UNCLASSIFIED - UNLIMITED

(2)

NORTH ATLANTIC TREATY ORGANIZATION
DEFENCE RESEARCH GROUP

1084-90

TECHNICAL REPORT
AC/243(Panel 3)TR/3

MILLIMETRE WAVE PROPAGATION OVER THE SEA

Panel 3 on Physics and Electronics

RSG.8 on Propagation and Target / Background Signatures at Millimetre Wavelenghts

UNCLASSIFIED - UNLIMITED

REPORT DOCUMENTATION PAGE

1. Recipient's Reference:	2. Further Reference:
3. Originator's Reference: AC/243(Panel 3)TR/3	4. Security Classification: UNCLASSIFIED/UNLIMITED
	5. Date: 29 OCT 90 / 6. Total Pages: 193 p.

7. Title (NU):
MILLIMETRE WAVE PROPAGATION OVER THE SEA

8. Presented at:

9. Author's/Editor's:
Dr. Y.G.M. Hurtaud

10. Author(s)/Editor(s) Address: Centre d'Electronique de l'Armement (CELAR) 35998 Rennes-Armees France	11. NATO Staff Point of Contact: Defence Research Section NATO Headquarters B-1110 Brussels Belgium (Not a Distribution Centre)

12. Distribution Statement:

Approved for public release. Distribution of this document is unlimited, and is not controlled by NATO policies or security regulations.

13. Keywords/Descriptors:
FORWARD REFLECTION, SEA SURFACE, MILLIMETRE WAVE, TROPOSPHERIC PROPAGATION, RAIN ATTENUATION, MODELLING, MULTIPATH

14. Abstract:

Three measurement campaigns concerning the propagation of millimetre waves above the sea have taken place on the French Atlantic coast near the town of Lorient (Brittany). The length of the propagation path was 9.7 km. Due to the low position of the antennas also the sea surface was illuminated and part of the transmitted energy was reflected by it. From the analysed propagation and environmental data, mainly at 36 and 94 GHz, it appears that the following phenomena have a major influence on propagation: reflection at the sea surface, attenuation due to rain and non-standard atmospheric condition.

ORIGINAL: FRENCH
29th October 1990

TECHNICAL REPORT
AC/243(Panel 3)TR/3

DEFENCE RESEARCH GROUP

PANEL 3 ON PHYSICS AND ELECTRONICS

Technical Report on Millimetre Wave Propagation over the Sea

This is the technical report on Millimetre Wave Propagation over the Sea prepared by RSG.8 on Propagation and Target/Background Signatures at Millimetre Wavelengths under Panel 3 on Physics and Electronics. The Executive Summary of this report ("Yellow Pages") was also distributed under reference AC/243-N/309, dated 29th August 1990.

(Signed) Dr. K. GARDNER
Defence Research Section

This page has been left blank intentionally

SUMMARY NOTE ON THE CONTRIBUTION TO THE STUDY OF MILLIMETRE WAVE PROPAGATION OVER THE SEA

I. BACKGROUND AND PURPOSE OF CAMPAIGNS

AC/243(Panel 3)RSG.8, which is responsible for millimetre wave studies, set up a sub-group to study propagation. The sub-group initiated three measurement campaigns with a view to analyzing line-of-sight propagation in the low trophosphere over the sea. These experiments were carried out on the French Atlantic coast close to the town of Lorient:

- from November 1981 to January 1982
- from October 1984 to January 1985
- from 4th to 31st August 1986.

The study of the interaction of shortwaves with the surface of the sea in fact dates back quite a long way. As early as the 50's major work was done in the United States, mainly on centimetre waves. The experiments reported here are thus an extension of the American work into the millimetre wave range (mainly at 36 and 94 GHz) and set out to:

- characterize precisely the aspect of the surface of the sea;
- analyse the effect of this rough surface on the signal received;
- study the effect of hydrometeors, mainly rain;
- to tackle abnormal propagation phenomena.

II. GEOMETRICAL AND RADIO CHARACTERISTICS OF THE LINK

A 9.7 km long point-to-point radio link operating at 36 GHz was set up by France. As a result of the limited height of the antennas (approximately 45 m and 13 m for the transmitter and receiver aerials respectively) some of the energy emitted was reflected off the surface of the sea. The received signal therefore consisted of the sum of the signals due to direct and reflected radiation.

This configuration produces a low angle of incidence of the reflected ray on the horizontal plane (less than 0.5°).

As a result of significant tidal activity, causing constant changes in geometry, the received signal exhibits periodic attenuations over time, known as interference figures.

III. ENVIRONMENTAL MEASURING EQUIPMENT USED

Propagation of millimetre waves over the sea is heavily dependent on the state of the sea surface as well as on atmospheric conditions. Substantial means of measuring environmental factors were therefore employed;

- two meteorological stations were set up, on either side of the link,
- a meteorological buoy and a wave measurement buoy were floated close to the line of sight,
- finally, in 1984, a spectropluviometer precisely measuring the size and speed of fall of raindrops was installed at the receiver site.

The data gathered by the sensors enabled:

- a large oceanographic and meteorological data base to be compiled,
- a large number of propagation events to be precisely interpreted.

IV. ANALYSIS OF THE DATA GATHERED

Three main lines of study, of unequal importance, emerged during processing of the data captured. They relate to:

- the effect of reflection off the surface of the sea;
- attenuation by rain;
- propagation under abnormal atmospheric conditions.

(a) Reflection off the surface of the sea

This phenomenon gives rise to short term and long term fluctuations in the signal level.

The short-term fluctuation level follows a Rice distribution. Analysis of the hydrodynamic and radio spectra together shows that the received signal is sensitive to low frequency sea movements.

The long-term fluctuations are due to tidal effects. They were reproduced by means of an elevator simulating, for a very short time, variations in the sea level. A propagation model based on geometric optics and taking account of the sphericity of the earth was developed. It permits reproduction of the slow variations in the received signal level.

By means of this model the coherent forward reflection coefficient was determined experimentally and compared with existing theories. The theory of Miller et al, which introduces the periodic aspect of sea movement is in good agreement with the experimental results.

(b) Attenuation due to rain

Rain is a hydrometeor which strongly attenuates millimetre waves. Its effect was studied experimentally by means of a spectropluviometer and a bucket pluviometer at the ends of the link. Raindrop size distributions were obtained. By means of Mie's theory giving the effective extinction cross-section of raindrops the linear attenuation was calculated and then compared with the usual models. In general, good agreement was noted.

The experimental attenuation caused by rain on the link was extracted from the received signal from the estimate of the attenuation due to the double path.

Because the rainfall area does not automatically represent a uniform profile, the predicted attenuation on the basis of pluviometric data and the attenuation derived from measured signal levels may differ widely at a given instant.

On the other hand, when it is raining simultaneously at both ends of the link, which is about 10 kilometres or less long, the frequency of occurrence of the attenuations can be correctly assessed from the raindrop size distribution recorded at one end of the link and the rainfall intensity recorded at the other end.

Finally, statistics relating to pluviometry and signal level at 95 GHz were calculated over about 1,700 hours' operation. They show that the horizontally polarized wave is appreciably more attenuated than the vertically polarized wave (a difference of the order of 2-3 dB), which is in line with theoretical predictions (the larger raindrops are more elongated horizontally than they are vertically).

(c) Propagation under abnormal atmospheric conditions

Under special meteorological conditions (advection movements, calm and sunny days), the received signal may be subject to large and rapid variations caused by fluctuations in the refractive index of the air. Atmospheric stratification is strongly dependent on meteorological parameters close to the surface. Their fluctuations induce variation in the radio properties of the atmophere, causing variations in the optical path and possibly the number of rays to be considered.

V. CONCLUSION

In short range surveillance, acquisition, tracking or communications applications, millimetre wave systems can be highly effective. This frequency range offers the advantages of the optical spectrum (high angular resolution and high directivity) while having good performance (unlike infrared radiation) under unfavourable atmospheric conditions such as fog, dust or smoke. In the communications field, millimetre wave systems can transmit more data while avoiding, by their high carrier frequency, interference with other channels.

Nevertheless, certain link configurations render propagation conditions difficult. This is particularly true when the antennas are positioned at low altitude above the sea. The signal is then constantly subject to greater or lesser fluctuations associated with the geometry of the link and the roughness of the sea. The studies carried out show that the form of the signal is very different when the sea is calm and when it is rough.

To improve transmission, space or frequency diversity methods are appropriate. In the case of the 36 GHz link, vertical displacement of the receiver antenna by 40 cm or a frequency shift of 1.6 GHz changes the signal level from one extreme to the other.

Experimental studies were carried out on the effect of hydrometeors. Fog has little influence on link availability. On the other hand, rain can give rise to strong attenuation causing breaks in the link for several minutes. Attenuation due to rain increases as the frequency rises. Attenuation is then more sensitive to the raindrop size distribution.

Finally, these experiments have highlighted propagation events associated with the structure of the atmosphere. The work done should be supplemented by more precise characterization of the air-sea interface (e.g. by refractometric measurements).

CONTENTS

CONTENTS (Cont'd)

CONTENTS (Cont'd)

INTRODUCTION

The last two decades have seen increasing interest in the implementation and assessment of systems operating in the millimetre wave band. This part of the electromagnetic spectrum, which extends from 30 GHz to 300 GHz (i.e. between 1 mm and 1 cm) has valuable properties. It has the advantages of optics (high angular resolution, substantial directivity) coupled with better performance in adverse atmospheric conditions (e.g. good penetration in smokes, fogs and dust). In addition, in the telecommunications field, these systems can transmit an increased amount of data, avoiding interference with other channels by their high carrier frequency.

Many applications arise from this wide variety of properties.

In the civil field:

- remote sensing in the environment and in space (weather radar, clear-air turbulence detector);
- air traffic control on airports;
- aids to air navigation in the vicinity of airports (helicopter- or aircraft-mounted cable detectors, landing aids);
- motor vehicle collision prevention (by installation of an obstacle-detection radar).

In the military field:

- target surveillance and acquisition;
- tracking and fire control;
- protected wide-band communications on the battlefield.

A substantial effort has been made to define millimetre-wave propagation in the atmosphere, both in the radar field and in the field of point-to-point links.

The study which follows deals with point-to-point propagation above the sea and through hydrometeors (mainly rain).

(a) Propagation above the sea

Up to now there have been a few experiments of this type at low altitude over the sea (Table 1).

BEARD and KATZ [1], [2] made a substantial series of measurements in the 1950s and, mainly in the centimetre field. From these they deduced rules governing propagation and the reflection of this type of wave on the surface of the sea.

This work was followed by a few experiments in the millimetre wave band: by MONDLOCH [3], VIGNALI [4], and SHERWELL [5]. These reveal disturbances at the following levels:

- the troposphere (due to absorption of the gases which compose the atmosphere and time-space variations in the refractive index of the air);
- the surface of the sea (because of reflection of part of the incident energy).

Nevertheless, there are gaps in all these contributions, particularly as regards the following:

* precise measurement of the sea surface state;
* analysis of short-term fluctuations;
* measurement of the coherent forward reflection coefficient;
* extension to the 95 GHz frequency.

(b) Propagation through rain

Rainfall disrupts millimetre-wave propagation, because the size of the raindrops is of the same order of magnitude as the incident wavelength. Raindrop size distribution should be measured in order to calculate attenuation accurately on the basis of rain data. There have been few measurements of this type.

In order to study phenomena (a) and (b) as a whole, there have been three measurement campaigns since 1981 over a total period of eight months, allocated as follows:

- three months from November 1981 to January 1982;
- four months from October 1984 to January 1985;
- the month of August 1986.

As part of this programme, several nations contributed to the experiments by supplying equipment and sending personnel. Links operating at 10.5, 16, 35, 36, 94 and 95 GHz were set up.

The experimental base was on the French Atlantic coast in southern BRITTANY, near LORIENT. The length of the links between the transmission site, on the island of GROIX and the reception site on the GAVRES peninsula, was 9.7 km. Propagation was entirely over the sea.

Part of the incident energy was reflected from the surface of the sea, because of the very small clearance between the antennas and the water. The resultant signal level is therefore represented as the sum of two signal levels, due respectively to direct radiation and indirect reflected radiation.

A knowledge of the sea surface state therefore seems essential. That is why a wave measurement buoy (measuring meteorological parameters if necessary) was put down near the reflection zone.

Other instruments to monitor environmental conditions have also been installed:

- weather stations on land recorded all the conventional meteorological parameters;
- an optical pluviometer at the reception site measured the raindrop size distribution.

All these items of equipment will be described in detail in Chapter I, which is intended to give an overall view of the experiments.

A theoretical approach to millimetre wave propagation at grazing-incidence will be embarked upon in Chapter II. Aspects of the mathematical description of the sea surface will have been set out previously for this purpose.

Chapter III relates to the experimental study of data on the sea surface and the received signal levels. Short- and long-term fluctuations due to reflection will be analysed.

Lastly, the influence of the troposphere upon propagation will be dealt with in detail in Chapter IV. Attenuation by rain will be the subject of particular attention, and phenomena linked to the structure of the layer above the surface of the sea will also be described.

Authors	Year	Frequency Used	Link Distance	Angle of Incidence On Sea	Antenna Gain	Polarisation	Beamwidth
Beard and Katz	1953	band X	2.8 km 4.7 km	0.6° - 8°		Vertical linear	E: 8° R: 5.5°
Beard	1955	5.3 GHz 9.3 GHz 36 GHz	1.7 km	0.74°	20 dB 27 dB	Vertical linear	E: 20° R: 0.3° (X)
Mondloch	1969	53 GHz	11.3 km	0.28°	40 dB	Vertical or horizontal linear	
Vignali	1970	37 GHz	16 km	0.24°	37 dB		2°
Sherwell	1981	81 GHz	5.6 km	0.20°	E: 46 dB R: 53 dB	Vertical or horizontal linear	

Table 1

CHAPTER I

OVERVIEW OF EXPERIMENTS

1.1 DESCRIPTION OF SITE

The various measurement campaigns described here took place at the same site, near LORIENT (Figure 1.1).

Its exposure to the sea is limited on the north side by the coast and on the east and south-east by the QUIBERON peninsula and BELLE-ILE. Only the south and west sectors are exposed to the sea; these are therefore a priori the sectors marked by high roughness values.

As will be shown later, the reflection zone for all the systems is close to the south point of the peninsula of Gavres. (Indicated as "Pointe de Gavres" in map 1-3 on page 52-54).

This zone is in the immediate vicinity of the coast. The sea-bed here is at a depth of 10-15 m and rises steadily towards the beach. In the approaches to the coast, the long swells take a southerly direction in accordance with the law of refraction (Chapter II, paragraph 2.3.2).

Lastly, it should be noted that the fetches (Chapter II, paragraph 2.2.3.1) linked with the north and east sector winds are very short. These winds cannot raise he sea in the reflection zone even if they blow very strongly.

1.2 MEASUREMENTS RELATING TO ENVIRONMENTAL DATA

1.2.1 Measurement of mean sea level height

Mean sea level heights were measured all the time at PORT-TUDY (Ile de GROIX), about 9 km from the reflection zone. These measurements are made on a regular basis by the Service Hydrographique et Océanographique de la Marine (S.H.O.M.) using a tide-gauge. They are given in tabulated form. The mean heights are given relative to the zero level on marine charts, corresponding to the low-water position during the strongest possible tide (coefficient 120).

The tide in the region under consideration is of semi-diurnal type and varies almost sinusoidally. It oscillates about a level set at 3 m relative to the previous reference. Its range (or amplitude) lies between 2 m and 5 m.

1.2.2 Measurement of sea roughness

A buoy equipped with an accelerometer sensitive to vertical movements supplied typical sea-state parameters regularly throughout the measurement campaigns.

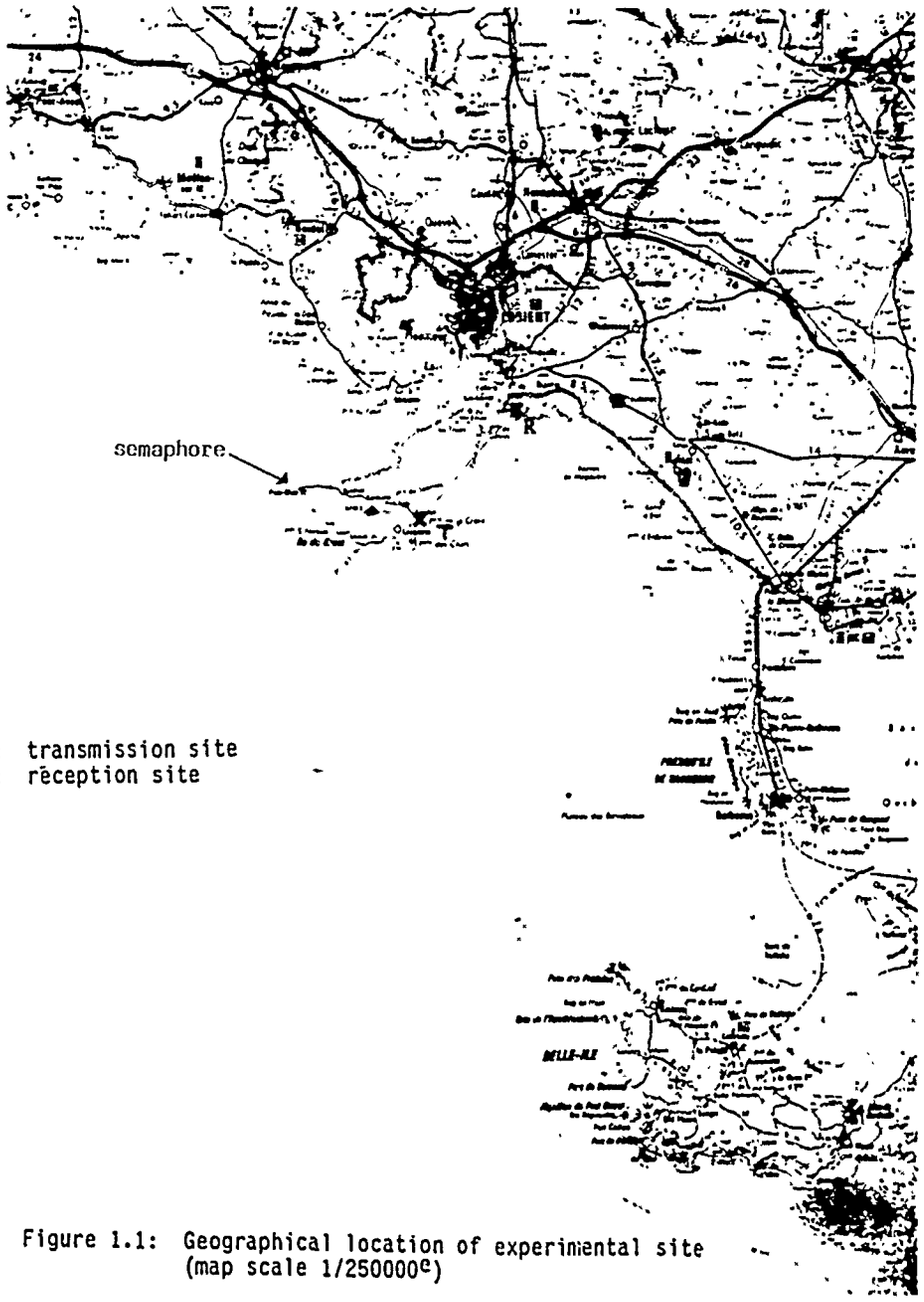

T: transmission site
R: réception site

Figure 1.1: Geographical location of experimental site (map scale 1/250000e)

For precise analysis of the measurements, a description of this equipment and the descriptive parameter calculation processes is given below.

For reasons of availability, a different buoy was used for each campaign.

1.2.2.1 Operating principle

These buoys operate on the same principle: they are equipped with an accelerometer sensitive to vertical movements. Double integration is used to reconstitute instantaneous variations in sea level. The desired parameters are obtained by processing these data.

1.2.2.2 Description of wave measurement buoys

The principal characteristics of the two buoys used during the measurement campaigns in autumn-winter 1984/85 and August 1986 are listed in Table 1.1.

A separate description is given so that certain specific aspects of each of them can be defined more precisely.

(a) C.O.B. buoy anchored in 1984/85

The buoy, which was lent by the Centre Océanographique de Bretagne (now called IFREMER), was of "MARISONDE" type [6]. This buoy is experimental in design and was studied in depth as part of a doctorate [7].

The parameter extraction algorithm (significant wave height H1/3 and significant wave period TH1/3) is based upon the narrow-spectrum hypothesis (Chapter II, paragraph 2.2.2.4). H1/3 and TH1/3 are then calculated on the basis of the second-order position and speed moments M_0 and M_2. However, this hypothesis is not regularly proved with any mooring place. Superposition of a sea raised by the wind and a swell movement leads to a broad spectrum.

The Argos system was used for data transmission on land. An ARGOS test kit on land interrogated the buoy every half-hour. The buoy transmitted these data concurrently every 3 hours to an ARGOS network satellite.

(b) DATAWELL buoy anchored in August 1986

A "DATAWELL" buoy of "WAVERIDER" type was anchored in the same zone in 1984/85 [8]. Throughout the experiments it was linked to a weather buoy by a 5 kg floating chain. The vertical accelerometer was fixed to a stabilised platform with high inertia (natural period 40 s) in order to eliminate horizontal accelarations due to pitching, rolling and the mooring of the buoy.

	C.O.B. buoy	DATAWELL buoy
Position	47° 39' 45" N 3° 21' 10" W	47° 39' 45" N 3° 22' 08" W
Physical Characteristics		
Weight	400 kg	70 kg
Diameter	1.2 m	0.7 m
Mast height	2 m	-
Height of ballast beam	1.5 m	-
Parameters measured (accuracy)		
Hl/3	± 0.1 m	± 0.1 m
THl/3	± 0.1 s	
Hmean	-	± 0.1 m
Hmax	± 0.1 m	-
Sampling time	10 mn	20 mn
Measurement rate	20 mn	20 mn
Data transmission mode	ARGOS network and ARGOS test kit	27 MHz link connecting buoy to reception site

Table 1.1

Its frequency response to vertical movements is shown in Figure 1.2. This indicates a constant response in the [0.08 Hz, 0.3 Hz] band for a zero mooring force. The manufacturer's curve shows that the buoy is relatively insensitive to low-frequency movements (a fall in the transfer function towards low frequencies as from about 0.08 Hz) and to high-frequency movements (steep slope at 1 Hz).

The significant parameters are computed on the basis of the reconstituted instantaneous heights by sorting the waves according to increasing amplitude. The largest waves are then averaged in accordance with the definition (Chapter II, paragraph 2.2.2.4). This technique does not presuppose any particular assumption on the signal contrary to the C.O.B. buoy algorithm.

1.2.3 Measurement of meteorological conditions

1.2.3.1 Measurements at sea

Measurements defining the surface of the sea were supplemented by meteorological measurements.

During the 1984-1985 campaign, the C.O.B. buoy had a vane and an anemometer fixed to a mast at a height of 2 m. They measured the speed and direction of the average wind over 12 minutes. Their accuracy was of the order of ± 2 m/s for speed and $\pm 10°$ for direction.

During the August 1986 campaign an XM 25 NEREIDE type meteorological buoy (to which the wave measurement buoy was moored) measured the following at 30-minute intervals:

- wind speed and direction;
- air temperature;
- humidity;
- pressure;
- solar radiation.

The acquisition period was 10 minutes for wind, about 2 minutes for air temperature, humidity and pressure and about 4 minutes for solar radiation.

1.2.3.2 Measurements on land

Weather stations

A SIMOUN [9] weather station manufactured by ENERTEC was installed on the transmission site at an altitude of about 30 m. Similarly another weather station was installed at the reception site at an altitude of 10 m.

These stations measured all the conventional meteorological parameters at 6-minute and 10-minute intervals respectively.

Ile de GROIX semaphore station [9]

The meteorological and oceanographic readings of the GROIX semaphore station, which is at the north-west of the island at an altitude of 40 m, were available. (See Figure 1.1 for its location).

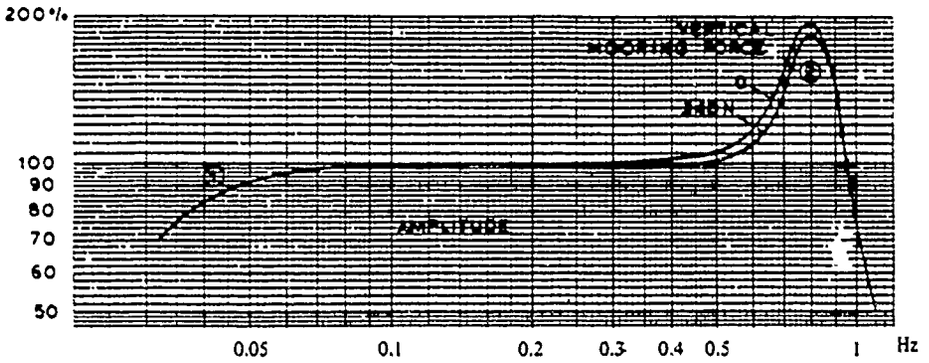

Figure 1.2: Buoy transfer function (supplied by manufacturer)

They show, at synoptic times of day:

- air temperature;
- wind speed and direction;
- atmospheric pressure;
- visibility;
- measured rainfall (in depth of water).

In addition, a monthly weather table sets out all adventitious phenomena (in intensity and duration as regards precipitation).

1.2.4 Rain gauge measurements

Two rain gauges were placed on either side of the link in order to study attenuation by rain at millimetre wavelengths:

- one was a conventional bucket-type rain gauge, which measured the rainfall at the transmission site;
- the other, a spectropluviometer, measured the rain at the reception site.

1.2.4.1 The spectropluviometer, an instrument measuring the size of raindrops

This sensor has been designed by CNET for accurate measurement of rainfall [10], [11].

Unlike the techniques developed previously, there is no physical contact between the apparatus and the raindrops, since measurements are made optically. Processing the rough data yields a double histogram, showing raindrop diameter (from 0 to 5 mm) and speed (from 0 to 10 m/s). The raindrops are classified in 16 classes of equal dropsize intervals.

(a) Measurement principle

An infrared-transmitting electroluminescent diode forms a parallelepipedic beam through a convergent lens and a horizontal rectangular diaphragm (Figure 1.3). This beam is focused on a photodiode. The current delivered by the latter is constant when the beam is not interrupted. When a raindrop passes through the beam, the light decreases in intensity relative to its nominal value. After elimination of the continuous component, inversion and amplification, the signal is composed of pulses whose height and width are functions respectively of raindrop size and speed of fall.

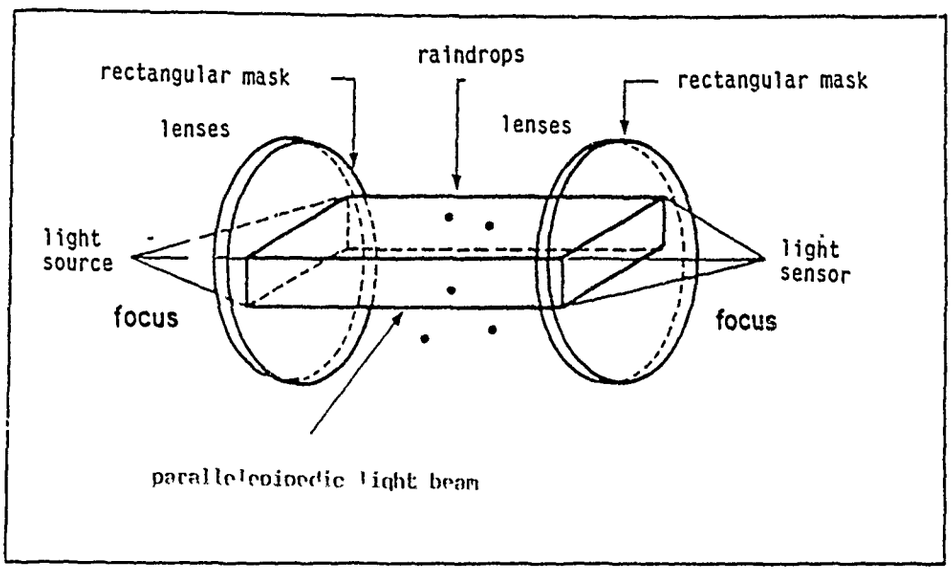

Figure 1.3: Simplified diagram of spectropluviometer

(b) Obtaining raindrop speed and diameter

Diameter

The pulse maximum amplitude is proportional to the effective vertical cross-section of the drop. The diameter of a drop (which is assumed to be spherical) is therefore deduced from that value.

Speed

Estimation of velocity is more tricky. A special computation method is used to avoid errors due to the simultaneous passage of several drops through the beam. The method is based on the fact that the surface of the pulses due to passage of the drop is proportional to D^2/V, where V is the vertical component of raindrop velocity and D is its diameter (Figure 1.4).

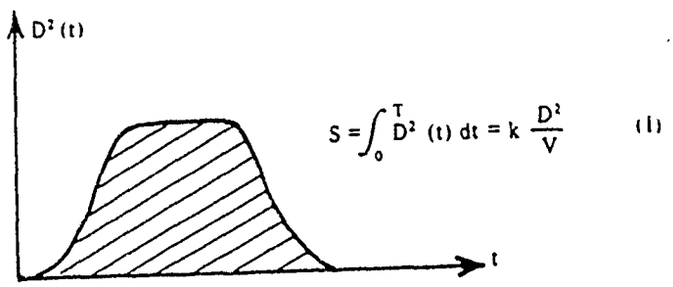

$$S = \int_0^T D^2(t)\,dt = k\,\frac{D^2}{V} \qquad (1)$$

Figure 1.4

(c) Rain rate computation

The spectropluviometer measures the velocity and diameter of raindrops which interrupt the beam. The measurement interval of these two parameters is shown in Table 1.2.

	Minimum Value	Maximum Value	Step	Number of Steps
Diameter	0.156 mm	4.843 mm	0.312 mm	16
Speed	0.312 m/s	9.688 m/s	0.625 m/s	16

Table 1.2

Errors due to the edge effects are limited by pre-processing, where raindrops with a velocity which deviates more than 50% from the GUNN and KINZER expression are eliminated (Chapter IV, paragraph 4.3.1.4).

The drop distribution $n(D,v)$ per m^3 and by diameter and velocity interval is obtained on the basis of the number $C(D,v)$ of drops counted in each diameter and velocity class. The distribution is such that:

$$n(D,v) = C(D,v) / (S \cdot \Delta t \cdot v(D)) \quad (2)$$

An expression in which:

- S is the pluviometer sampling area (10^{-2} m^2);
- Δt is the sampling time.

The velocity v and the diameter D refer to the central value in each class.

The drop concentration (m^{-4}) and the mean speed $v(D)$ for each sample are deduced from:

$$N(D) = \sum_v n(D,v) \quad (3)$$

$$v(D) = [\sum_v n(D,v) \cdot v] / N(D) \quad (4)$$

The rain rate can be computed on the basis of these two magnitudes:

$$R(mm/h) = 3.6\,10^6 \frac{\pi}{6} \sum_D N(D) \cdot v(D) \cdot D^3 \quad (5)$$

(d) Instrumental limitation

The raindrop diameter and drop velocity measurements are affected by errors. This uncertainty arises from three main factors:

- the sampling step;
- the design of the instrument;
- the environmental conditions.

The errors introduced by sampling are due to the statistical behaviour of the showers. Studies have been made of the fractional standard error $\delta R/R$ on the fall rate caused by taking the MARSHALL-PALMER distribution as a reference (Chapter IV, paragraph 4.3.1.4). For a sampling time of 60 s, which is typically used in the measurements, this error is about 8% for rain intensities of 1 mm/h and 4% for 100 mm/h.

The shape of the sensor gives rise to two types of error:

- the first type is due to the effects of the edges. When a drop falls on one of the two vertical sides of the beam, measurement leads to the detection of a small drop with an abnormally high speed. This effect tends to underestimate the number of drops in each class interval, the more so when the drops are large;
- the second type of error arises when more than one drop is present in the beam. The effect of this is to underestimate the number of small drops ($D < 1$ mm) and to overestimate the number of large drops.

In the case of a rain intensity of 1 mm/h these two effects combine to give an overall error $\Delta N/N$ less than 10% in the interval between the second and twelfth classes ([0.4 mm, 3.6 mm]). The interval for 10 mm/h extends from the third to the fourteenth class ([0.7 mm, 4.3 mm]) (Figure 1.5).

Nevertheless, the rain intensity error remains under 1% in the case of values not exceeding 30 mm/h (Figure 1.6).

1.2.4.2 Tipping - bucket rain gauge

This apparatus, classic in design, gives an estimate of the duration and intensity of the rainfall.

The water collected by a sharp-edged conical funnel falls into a bucket, which tips when it has collected a certain amount of water (Figure 1.7). The total number of times the bucket tips is recorded.

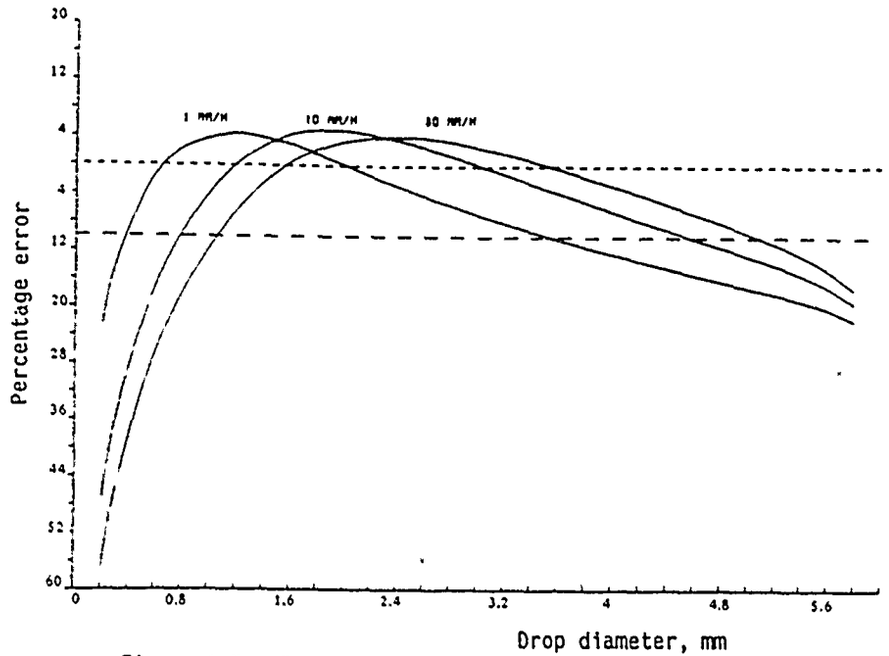

Figure 1.5: Error in number of drops per size interval for various rain intensities

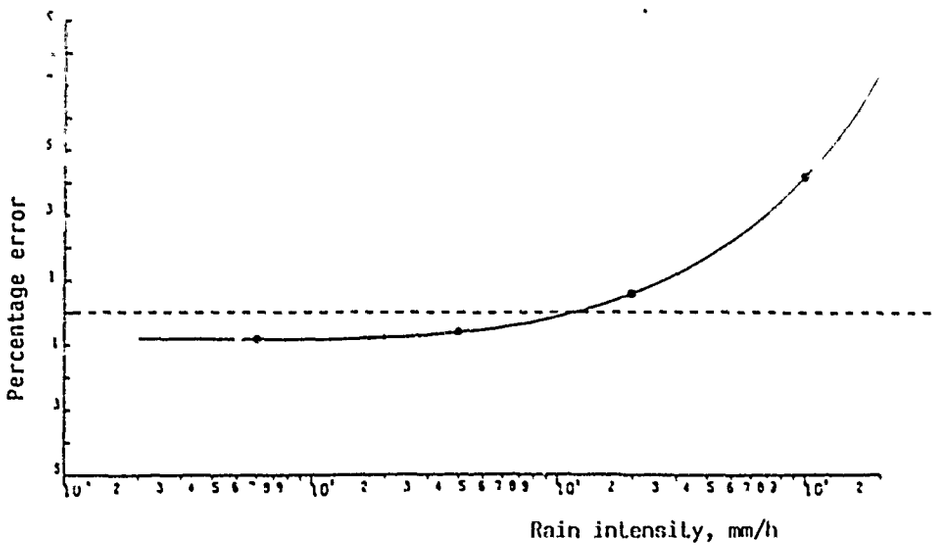

Figure 1.6: Error in rain intensity resulting from the combined effect of drop multiplicity and optical edge effect [11].

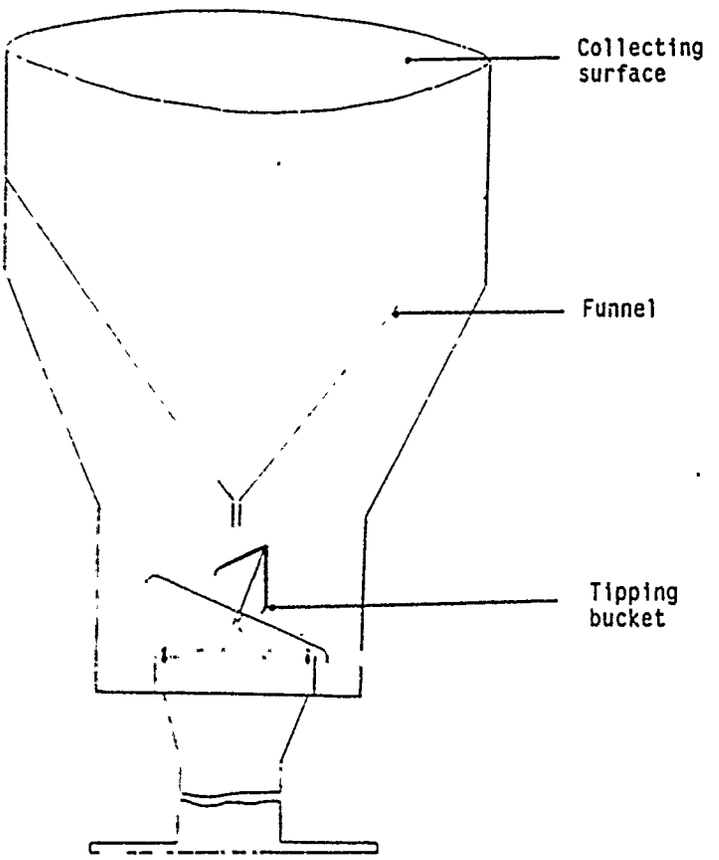

Figure 1.7: Simplified diagram of tipping-bucket rain gauge

The apparatus used during the experiments had a water collection surface of 1,000 cm^2. The amount of water necessary to cause the bucket to tip was 20 grams, i.e. 0.2 mm of rain.

Since the rain rates were taken every 6 minutes, the minimum rain rate value supplied by this gauge was therefore 2 mm/h (corresponding to one tip during the 6 minutes).

1.3 MEASUREMENTS RELATING TO PROPAGATION DATA

1.3.1 Link geometry

The transmitters and receivers were fixed during most of the experiments. During the months of October 1984 and August 1986, however, a hoist at GAVRES provided an opportunity for varying the receiver antenna height by about 4.8 m. This device made it possible to simulate the tide phenomenon in a sufficiently short time to eliminate variations in environmental conditions.

In these two types of experiment, the antenna height (relative to the marine chart zero level) for the link operating at 36 GHz is shown in Table 1.3.

Measurement Campaign	Transmission Height/ Level 0	Reception Height/ Level 0	Mean Angle of Incidence on Sea
1981 - 1982	18.6 m	12.7 m	0.15°
October 1984	48.2 m	10.3→15.1 m	0.3°
1984 - 1985	48.2 m	13.2 m	0.3°
August 1986	48.2 m	10.3→ 15.1 m	0.3°

Table 1.3

The 36 GHz system was installed by us. Consequently the propagation data gathered at this frequency will be analysed in greater detail.

As regards the other links, the antenna heights can be found in Annex III.

As can be seen, the aerial locations lead to an angle of incidence of the ray reflected on the sea of less than 0.5° relative to the horizontal plane.

1.3.2 Description of transmission systems

1.3.2.1 System operating at 36 GHz:

- TFH 720

The TFH 720, manufactured by THOMSON - CSF, is a mobile military link capable of transmitting digital data at a rate of 2 Mbit/s or 8.5 Mbit/s, corresponding to 30 or 120 simultaneous telephone channels [12], [13]. The principal characteristics are given in Table 1.4.

TRANSMITTER	Power transmitted	50 mW
	Source	GUNN oscillator
	Modulation	Binary phase shift keying (DPSK)
	Antenna	Cassegrain type, diameter: 40 cm
	beamwidth at 3 dB gain polarisation	1.5° 42 dB 45°
RECEIVER	Detector	GUNN oscillator-mixer
	Antenna	Cassegrain type, diameter: 40 cm
	beamwidth at 3 dB gain polarisation	1.5° 42 dB linear at 45° relative to the horizontal
	Dynamic range	About 60 dB

Table 1.4

NOTE: The behaviour of the digital link according to environmental conditions is not described in this paper.

Year	Frequency	TRANSMISSION				RECEPTION			
		Transmitted Power	Antenna	Beamwidth at 3 dB	Polarisation	Antenna	Beamwidth at 3 dB	Polarisation	Dynamic
1981-1982	94 GHz Netherlands	40 mW	Horn with lens D=0.23 m	1°	Vertical linear	Cassegrain type D=1.2 m	0.19°	Vertical linear	> 50 dB
1981-1982	95 GHz Germany	50 mW	Cassegrain type D=0.6 m	0.35°	Linear at 45° (*)	Cassegrain type D=0.6 m	0.35°	Vertical or horizontal linear	40 dB
1984-1985 1986	10.56 GHz Netherlands	300 mW	Parabolic D=1.10 m	1.96°	Horizontal linear	Parabolic D=1.22 m	1.7°	Horizontal linear	30 dB
1984-1985	16 GHz United States	40 mW	Parabolic D=0.915 m	1.43°	Vertical linear	Parabolic D=0.915 m	1.43°	Vertical linear	60 dB
1984-1985 1986	35 GHz Netherlands	40 mW	Parabolic D=0.41 m	1.5°	Horizontal linear	Parabolic D=0.41 m	1.5°	Horizontal linear	40 dB
1984-1985	94 GHz Netherlands	40 mW	Horn with lens D=0.23 m	1°	Horizontal linear	Parabolic D=0.41 m	0.54°	Horizontal linear	40 dB
1984-1985 1986	95 GHz Germany	50 mW	Parabolic D=0.305 m	0.72°	Right-handed circular	Parabolic D=0.305 m	0.72°	Right-handed circular	70 dB

Table 1.5

1.3.2.2 Systems operating at other frequencies

The principal characteristics of the systems installed during successive measurement campaigns are shown in Table 1.5. The high level of antenna directivity is particularly apparent: antenna beamwidth at 3 dB is always less than 1.5°. The polarisation of the transmitted signal was linear, except in the case of the German 95 GHz system installed in 1984-1985 and 1986, in which polarisation is right-handed circular.

1.3.2.3 Remarks

The field level at the receiver input is obtained on the basis of measurement of automatic gain control (AGC) and a voltage-level calibration curve supplied by the manufacturer.

The received power level, corresponding to propagation losses in free space, is readily arrived at when the characteristics of the systems are known (Annex III). This level is at -42 dBm in the case of the 36 GHz link.

1.3.3 Qualitative presentation of propagation measurements

The measurement campaigns as a whole have revealed a certain number of propagation phenomena linked to the sea surface state and environmental conditions.

The phenomena primarily affecting this type of grazing - incidence link are presented initially by a qualitative approach.

In the case of the sea, the reflection phenomenon creates:

- long-term signal level fluctuations;
- short-term signal level fluctuations.

The former type of fluctuation is caused by variations in the mean level of the sea. The resultant field E_T can be written as a first approximation as the sum of the direct field E_{di} and the reflected field E_r according to the following expression:

$$E_T = (E_{di}^2 + E_r^2 + 2 E_{di} E_r \cos\theta)^{1/2}$$

where 0 is the difference in phase between the direct ray and the indirect ray:

$$\theta = \frac{4\pi (h_e - h_m)(h_r - h_m)}{\lambda d} + \pi \qquad (6)$$

where h_m is the mean sea level height;

- h_t and h_r are the transmission and reception antenna heights;
- d is the link distance; and λ is the transmission wavelength.

For a given link geometry, the number of passages through the extrema in one tide is proportional to the range and to the transmission frequency.

Moreover, these periodic attenuations are all the more marked when the sea is calm. This is illustrated by Figure 1.8, which shows the received signal level at 36 GHz as a function of time for two "extreme" cases (calm sea and rough sea). The disappearance of the interference figure in the case of the rough sea can be seen.

The second type of fluctuation is due to reflection on the waves (Figure 1.9). Their dominant periodicity is 10 s maximum. For a given average field level their amplitude is an increasing function of roughness.

The rain creates substantial attenuations, the more so when the frequency is high: this is illustrated by Figure 1.10. Whereas attenuation is no more than a few dB at 10.5 GHz, it exceeds 20 dB at 35 GHz and 94 GHz. The receiver noise level is reached at the latter frequency and saturation is apparent.

With a calm sea, attenuation due to rain is added to that caused by multipaths.

Lastly, the low troposphere affects propagation by altering the ray trajectory and disrupting the signal in amplitude and in phase. This shows itself in "abnormal" fluctuations in the received signal level. Figure 1.11 clearly shows that these fluctuations are linked to atmospheric conditions: they cease suddenly at about 17 h 15 as a consequence of an increase in relative humidity H_{buoy} (from 62% to 92%) and a drop in ambient temperature T_{buoy} (from 25.6°C to 19.7°C).

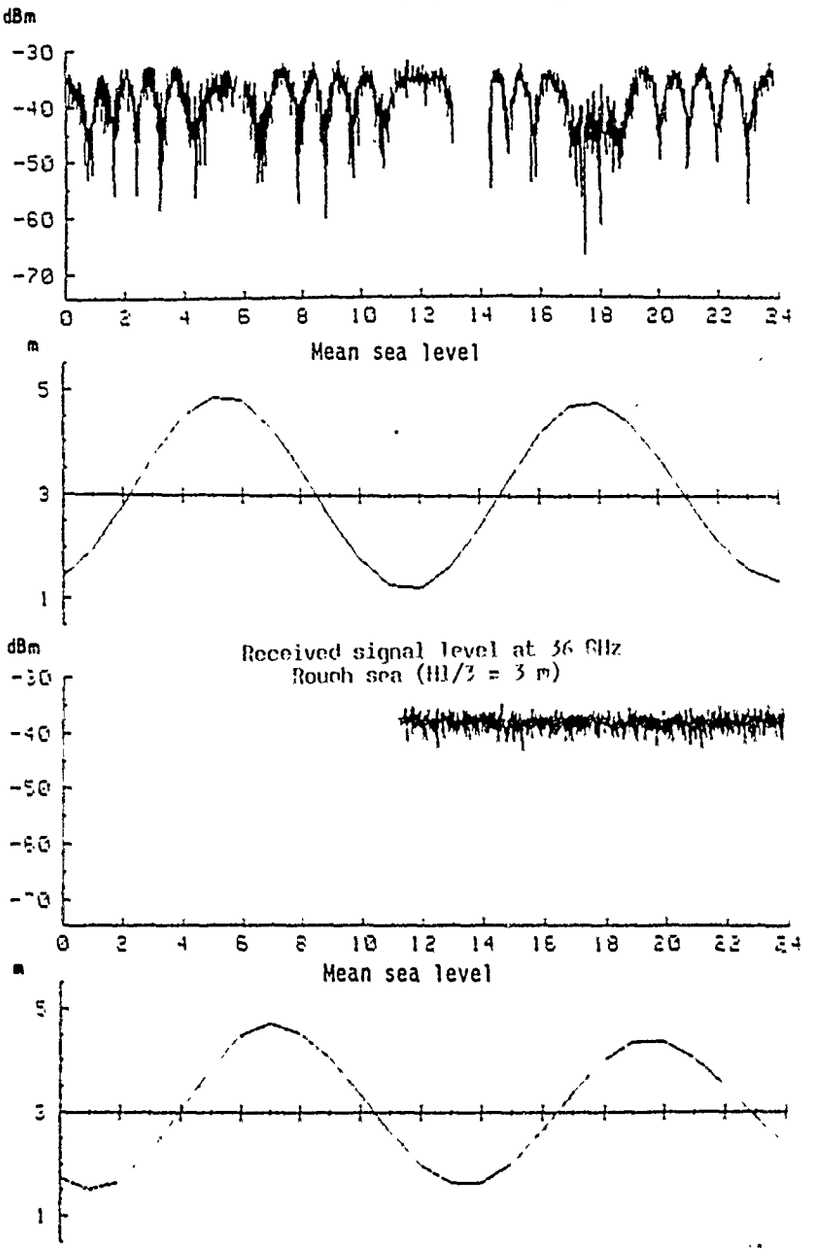

Figure 1.8: Received signal level at 36 GHz according to tide and roughness of sea

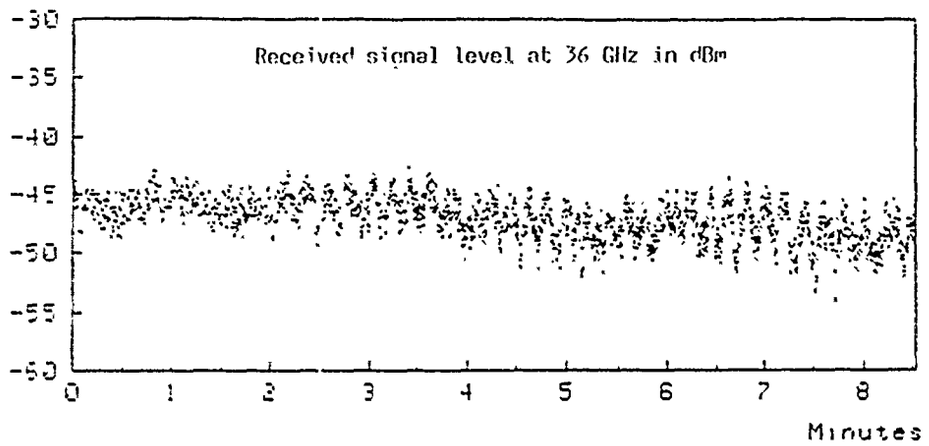

Figure 1.9: Short-term fluctuations due to reflection on the sea

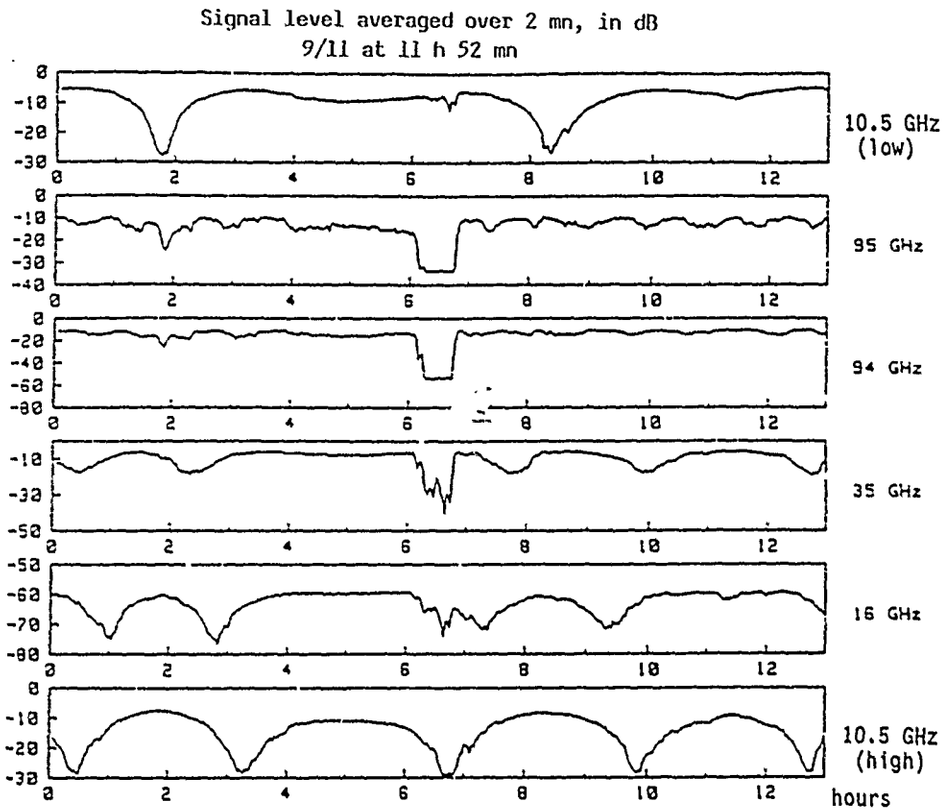

Figure 1.10: Rain event

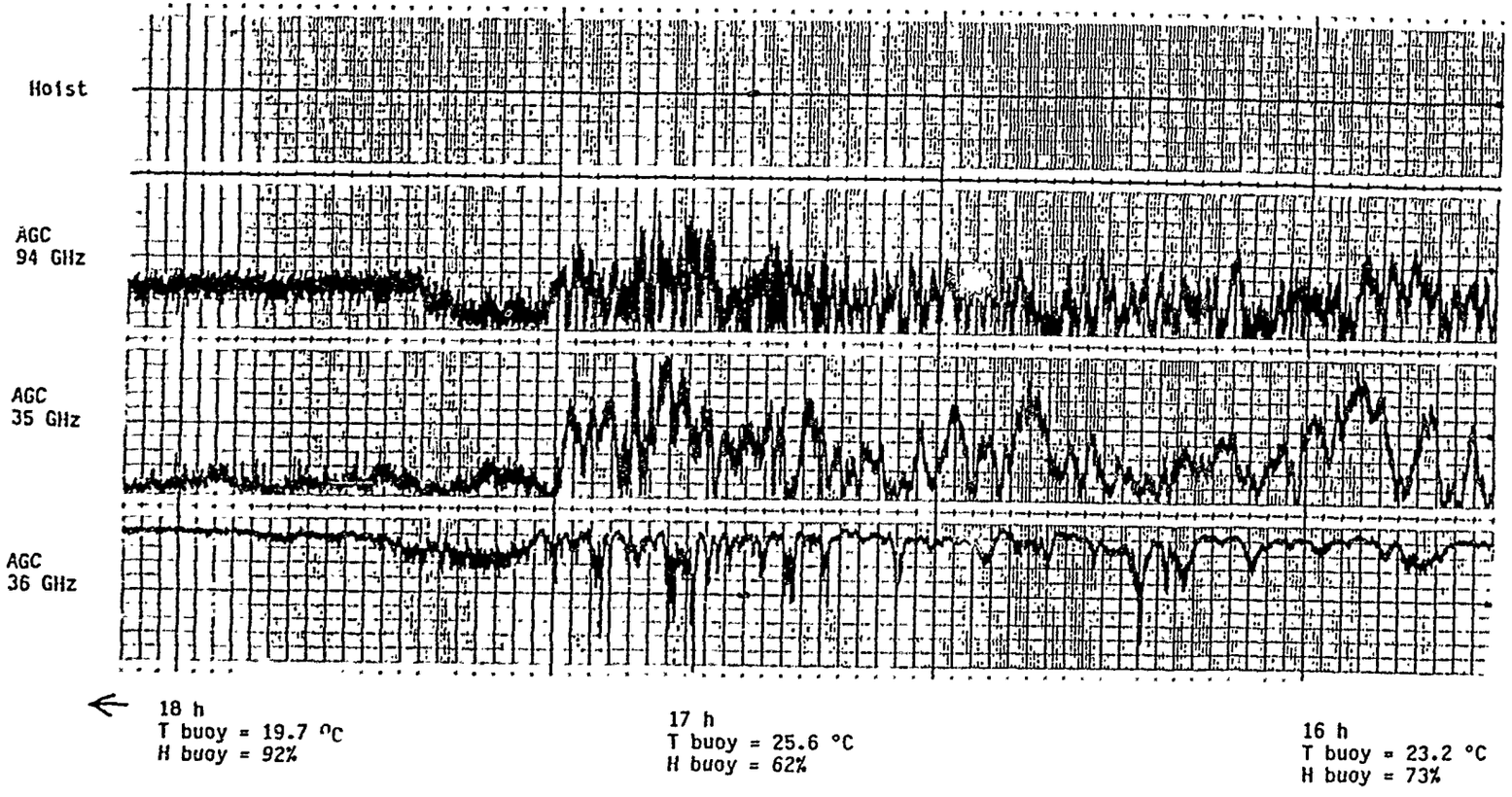

Figure 1.11: Atmospheric scintillations, 17-08-86

CHAPTER II

THEORETICAL APPROACH TO PHENOMENA RELATING TO REFLECTION ON THE SEA

2.1 INTRODUCTION

In the case of the links under consideration, i.e. links with grazing incidence, the fact that part of the transmitted energy is reflected on the sea profoundly affects transmission quality. The disruptions caused by the existence of a secondary ray should therefore be analysed in detail.

First of all, the surface of the sea will be described both from the deterministic and from the probabilistic aspect, in order to complete this study.

All the theoretical factors essential to the use of the propagation and environmental data will then be set out.

2.2 DESCRIPTION OF THE SEA SURFACE

2.2.1 Deterministic representation of the sea surface

2.2.1.1 Hydrodynamics equations [14], [15]

In general, movement of the sea surface is defined by a group of second-order non-linear equations derived from the laws of hydrodynamics. It is represented by a function z (x,y,t) dependent upon two orthogonal horizontal co-ordinates and time (Figure 2.1).

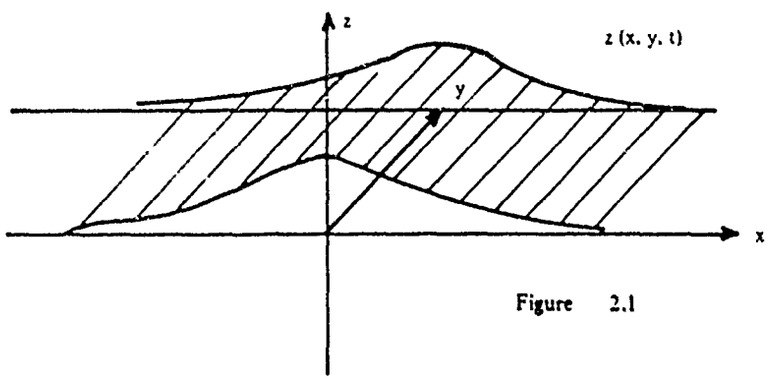

Figure 2.1

In order to simplify the treatment, the fluid is assumed to be homogeneous, incompressible and frictionless. The pressure put on the water is independent of co-ordinate y. Lastly, the fluid is confined by a surface in contact with the air and by the sea-bed at depth P.

If the space in which the study is made is a vortex-free medium, the movement of the fluid is irrotational: the speeds of movement of this fluid are derived from a potential ϕ called the velocity potential. Thus the continuity equation for an incompressible fluid is written as follows:

$$\Delta \phi = 0 \qquad (1)$$

The conditions at the following limits are added to this equation:

- Condition at the sea-bed.

The vertical velocity of the particles tends towards zero with great depths.

- Condition of constant pressure at the free surface (dynamic condition).

- Condition of hydrodynamic equilibrum or kinematic condition.

This gives expression to the fact that the water particles follow the surface movement.

These conditions lead to a system of differential equations which have no exact overall solutions. One method of solving this system is to develop the solution as a limited series (perturbation method). When the variations in surface movement decrease with respect to its wavelength, the maximum order of the series representing the solution decreases; some equations become linear and solvable.

2.2.1.2 First-order approximation

The first-order approximation becomes valid where the ratio of amplitude to wavelength is very small.

Then the sea movement equation is represented by a sine curve of peak-to-peak amplitude 2a propagating along the positive x axes:

$$z(x,t) = a \sin(k x - \omega t) \qquad (2)$$

where k represents the wave number, $k = 2\pi / \lambda$;

ω is the movement pulsation, linked to k by the relationship:

$$\omega^2 = g k \tanh(kP) \qquad (3)$$

where g is the gravity constant ($g = 9.81\ m/s^2$), P the depth and tanh the hyperbolic tangent.

The velocity of the movement can be deduced immediately as a function of the wavelength:

$$C = \frac{\omega}{k} = \left[\frac{g\lambda}{2\pi} \tanh\left(\frac{2\pi P}{\lambda}\right)\right]^{\frac{1}{2}} \qquad (4)$$

This formula calls for two observations:

(a) the sea is a dispersive medium, the velocity of the waves being linked to their wavelength. Velocity is independent of amplitude, as expected;

(b) expression (4) is simplified when the depth P increases and the P/λ ratio tends towards infinity:

$$C = \left(\frac{g\lambda}{2\pi}\right)^{\frac{1}{2}} = \frac{gT}{2\pi} \qquad (5)$$

The sea-bed had no effect upon movement as long as the depth is greater than the half-wavelength. The velocity ratio $C(P = \lambda/2)/C(P = \infty)$ is in fact equal to 0.998.

Figures 2.2 and 2.3, showing the speed and wavelength of waves as a function of their periods and the depth of the sea-bed illustrate this point: the P = 20 m curve separates from the curve where the depth is infinite ($P = \infty$) at a wavelength of about 40 m.

2.2.1.3 Solution at higher orders

Solution of the system of equations is more complicated when the amplitude-wavelength ratio is not low. Nevertheless literal expressions can be obtained at the higher orders, subject to simplifications.

Where the depth is infinite, solutions at the second, third and fourth orders in the form f(x-C.t) (where the velocity of propagation C is constant) have been demonstrated (STOKES solutions).

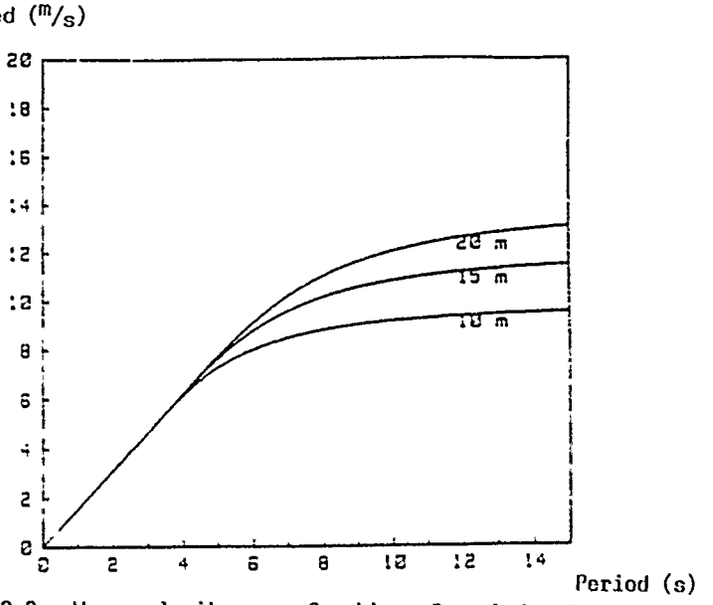

Figure 2.2: Wave velocity as a function of period and depth.

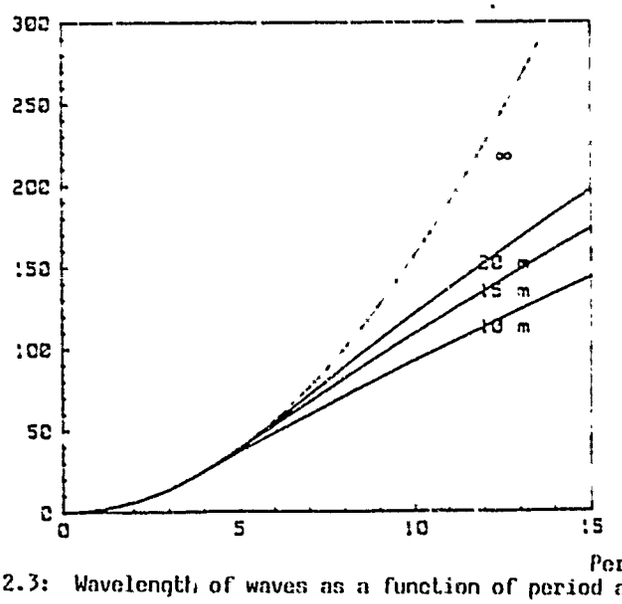

Figure 2.3: Wavelength of waves as a function of period and depth

Thus the second-order solution can be written as follows:

$$z(x,t) = -a\cos[k(x - C.t)] + \frac{k\,a}{2}\cos[2k(x - C.t)] \qquad (6)$$

where $C = (g\lambda/2\pi)^{\frac{1}{2}}$ is identical to the first-order expression obtained.

A feature of its graphic representation is that the peaks are sharper than the troughs, so that there is no longer symmetry relative to the x axis.

At the third order, speed becomes a function of amplitude:

$$C = \frac{g\lambda}{2\pi}\left(1 + \frac{4\pi^2}{\lambda^2}a^2\right) \qquad (7)$$

The peaks become sharper.

A maximum value of the ratio $2a/\lambda$ [called the wave steepness (C_b)] is obtained by adhering to the continuity equations at the water-air interface in the case of rough surfaces:

$$C_{b\,max}(P) = 0.14\tanh\frac{2\pi P}{\lambda} \qquad (8)$$

Beyond this the wave breaks because it is unstable. The ultimate waves have a peak angle of 120°.

2.2.1.4 Capillary waves

Only the waves known as gravity waves have been dealt with in this paragraph so far: slight surface movements, called capillary movements, are also present.

In order to study these the contact forces on the air-water separation surface must be taken into account, because they are no longer negligible with respect to gravity forces.

Calculation of the surface movement, presumed to be sinusoidal (first-order solution) is based upon the pressure discontinuity ΔP_r on the air-water contact surface:

$$\Delta P_r = T_s\left(\frac{1}{R_1} + \frac{1}{R_2}\right) \qquad (9)$$

where T_s is the surface tension and R_1 and R_2 are the principal radii of curvature of the surface.

Velocity of movement becomes:

$$C^2 = \frac{g}{k} + T_s \cdot k \qquad (10)$$

where $T_s = 7.4 \times 10^{-4}\ m^3/s^2$

When the wavelength varies from 0 to infinity, propagation velocity passes through a minimum: $C_m = 0.23$ m/s for $\lambda_m = 2(T_S/g)^{\frac{1}{2}} = 1.73$ cm.

The speed C, which then takes the form:

$$C_m = \frac{1}{2}\left(\frac{\lambda}{\lambda_m} + \frac{\lambda_m}{\lambda}\right) \qquad (11)$$

is shown in Figure 2.4.

When λ is less than λ_m, the second term predominates. This part of the curve corresponds to the capillary waves. When λ is greater than λ_m the first term assumes the greater importance. It relates to the gravity waves.

As soon as $\lambda < 1/3\,\lambda_m$ the gravity effect is negligible in the case of capillary waves. On the contrary, when $\lambda > 3\,\lambda_m$ the movements are pure gravity waves.

2.2.2 Statistical representation of the sea surface

Sea surface roughness at a point is the resultant of a certain number of movements differing in origin, amplitude and direction (e.g. sea raised by the wind, swell originating from the open sea). Consequently the surface of the sea has a disordered appearance, which calls for statistical representation.

2.2.2.1 Definition of the hydrodynamic spectrum

Let there be a ortho-normal frame of reference and surface $z = S(x,y,t)$ representing the sea at time t (Fig. 2.5).

Let us consider a point M_0 (x_0, y_0, z_0) on this surface: $z_0 = S(x_0, y_0, t)$ represents variations at this point in the height of the sea relative to the datum.

If it is assumed that at M_0 the surface confirms the steady-state property in the broad sense, i.e.:

- that the mean value $E\{(S(t))\}$ is constant;

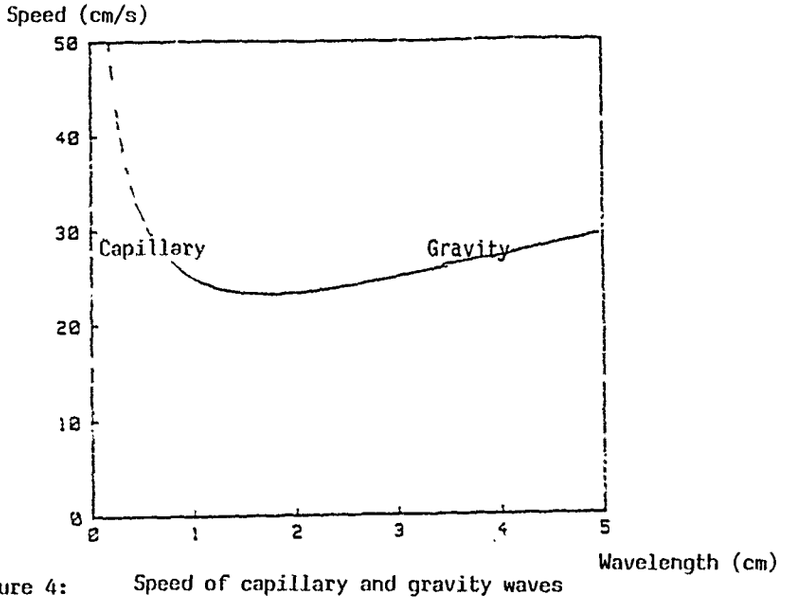

Figure 4: Speed of capillary and gravity waves

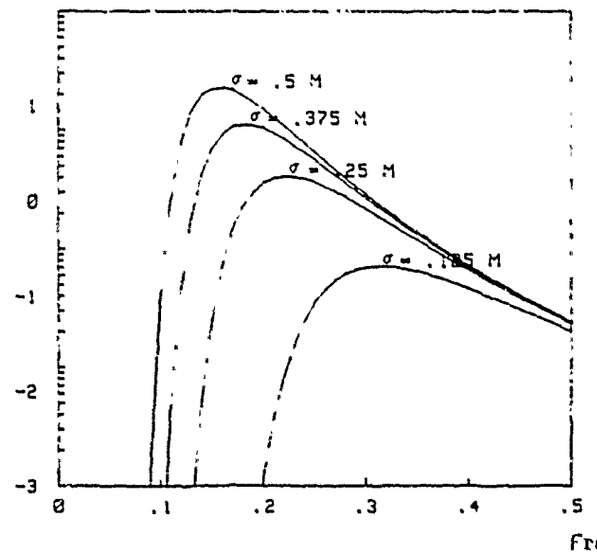

Figure 2.6: Pierson-Moskowitz spectra of sea raised by the wind

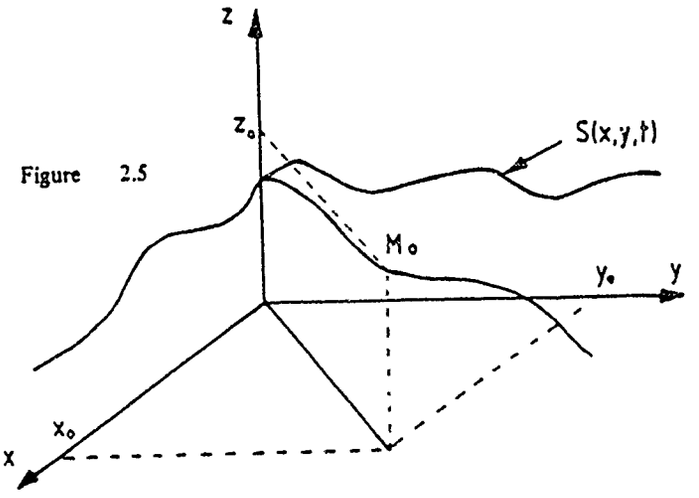

Figure 2.5

- that the mixed first-order moment, $E\{(S(t_1).S(t_2))\}$, also called covariance function, is reduced to an autocorrelation function $R(\tau) = C_S(t_1 - t_2)$ depending only on the time difference $\tau = t_1 - t_2$.

The energy spectrum or spectral density is then defined as being the FOURIER transform of the autocorrelation function.

$$\tilde{S}(\omega) = \frac{1}{2\pi} \int_{-\infty}^{+\infty} R(\tau) e^{-j\omega\tau} \, d\tau \qquad (12)$$

The reverse FOURIER transform is written as follows:

$$R(\tau) = \int_{-\infty}^{+\infty} \tilde{S}(\omega) e^{j\omega\tau} \, d\omega \qquad (13)$$

The spectral density represents the distribution of the mean-square surface height S(t) on the frequency axis.

$$\sigma^2 = R(0) = E\left\{S^2(t)\right\} = \int_{-\infty}^{+\infty} \tilde{S}(\omega) \, d\omega \qquad (14)$$

2.2.2.2 Proposed forms of gravity spectrum

When the sea is entirely raised by the wind, PIERSON and MOSKOWITZ [16] have suggested the following gravity spectrum, which gives the best match with that obtained experimentally at sea:

$$\tilde{S}(\omega) = \frac{0.084\, g^2}{\omega^5} \exp\left[-0.74\left(\frac{\omega_m}{\omega}\right)^4\right] \qquad (15)$$

where $W_m = g/Ws$ is the pulsation of the dominant wave and Ws is the wind velocity at a height of 19.5 m.

Figure 2.6 shows the shape of this spectrum for various degrees of roughness. It is noteworthy that the spectrum extends towards the low frequencies when the variations in level increase; the masses of water in motion are more and more substantial, and therefore the inertia increases.

A simple relationship between the wave mean-square height σ and the wind velocity can be deduced by using expression (14):

$$\sigma\,(m) = 6.571\ 10^{-3}\ \ W^2\,(m/s) \qquad (16)$$

PHILLIPS [17] states that the spectrum tends towards the following spectral distribution in the region of waves clearly higher than the dominant wave and smaller than the capillary waves (equilibrium region):

$$\tilde{S}(\omega) = \alpha\, g^2\, \omega^{-5} \qquad (17)$$

where α is a specific constant ($\alpha \approx 0.01$).

More recently other forms of spectrum have been suggested. In particular, formulae taking account of the wave formation distance have been given on the basis of the JONSWAP experiments [18].

2.2.2.3 Probability distribution of instantaneous sea levels

The instantaneous variation in the level of the sea at a given point on the surface can be written as the superposition of a large number of sine curves of random amplitude and phase:

$$z(t) = \sum_{k=1}^{N} a_k \cos(\omega_k t + \varphi_k) \qquad (18)$$

The process is assumed to be ergodic. This means that the temporal average of the random function Z(t) converges towards its statistical average.

When N tends towards infinity, the distribution of instantaneous variations in level tends towards the normal distribution:

$$p(z) = \frac{1}{\sqrt{2\pi}\sigma} \exp\left[-\frac{z^2}{2\sigma^2}\right] \qquad (19)$$

where σ^2 is the signal variance. Its square root is the mean-square wave height.

Since Z is a centred Gaussian function, it can be shown that the position is the same for its successive derivatives.

NOTE: In fact the probability distribution of the instantaneous variations in level differs from the normal distribution for the following two reasons:

- in the case of an actual surface the definition region of the distribution is limited in such a way that beyond the extreme limits the probability of observing the corresponding event is zero;

- the normal distribution is symmetrical about zero, whereas this is not the case with the actual distribution. In fact the surface shows peaks which are sharper than the troughs (see paragraph 2.2.1.3).

Some authors have suggested the GRAM-CHARLIER distribution, taking these observations into account [19].

Nevertheless the normal distribution is regarded as sufficient in a large number of cases.

2.2.2.4 Wave height probability distribution

2.2.2.4.1 Definition of wave height

We will define the wave height as the difference in level between a trough and the next crest (Figure 2.7).

2.2.2.4.2 Wave height probability distribution

This distribution is obtained with the aid of probability densities consisting of the random functions Z, Ż and Z̈.

The intermediate stage in obtaining this result involves calculating the probability of a peak in a small range of height Δ z and per unit of time.

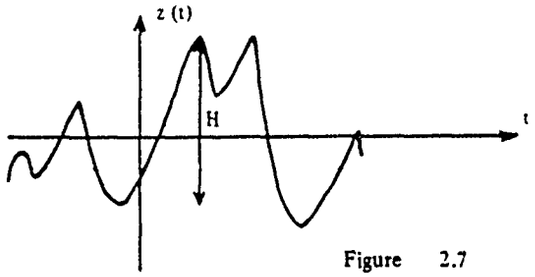

Figure 2.7

The associated probability density depends upon the width of the spectrum. The two extreme cases lead to a normal distribution for a broad spectrum and to a RAYLEIGH distribution for a narrow spectrum.

The probability density of the instantaneous heights can be deduced from this distribution, giving preference to waves of high amplitude, i.e. by considering the narrow spectrum. The probability distribution is then a RAYLEIGH distribution:

$$P(H) = \frac{H}{4 m_0} e^{-\frac{H^2}{8 m_0}} \qquad (20)$$

where H is the peak to peak amplitude and $\sqrt{m_0}$ is the mean-square height with $m_0 = E\{Z^2\}$.

This situation is seen in particular in the case of seas raised by the wind. These show a spectrum which becomes narrow in the case of high roughness levels (Figure 2.6, paragraph 2.2.2.2).

2.2.2.4.3 Significant parameters

(a) Definition of significant wave height

A parameter called the significant wave height or the height H1/3 is used in many oceanographic applications to characterize the surface of the sea [20]. It corresponds to visual observation of the sea. It is defined in a given period as the mean value of the heights of the upper third of the waves with the greatest amplitude.

Mathematically, this definition can be written as follows:

$$H1/3 = \frac{\int_{H_0}^{\infty} H\, P(H)\, dH}{\int_{H_0}^{\infty} P(H)\, dH} \qquad (21)$$

where $$\int_{H_0}^{\infty} P(H)\, dH = \frac{1}{3} \qquad (22)$$

(b) The case of the narrow spectrum for a sea raised by the wind

Assuming that H follows a RAYLEIGH distribution, H1/3 can be written as follows on the basis of the mean-square height $\sigma = \sqrt{m_0}$:

$$H1/3 = 4,0089 \cdot \sigma \qquad (23)$$

When the sea is raised by wind of a velocity Ws, (23) becomes:

$$H1/3\,(m) = 0.0270 \cdot W^2\,(m/s) \qquad (24)$$

The wave mean period, called the significant wave period and designated TH1/3, is generally associated with this wave classification. In the case of a fully developed sea, various works have shown that the period TH1/3 is always very close to the period associated with the peak of the PIERSON-MOSKOWITZ spectrum:

$$TH1/3 \simeq TM \quad \text{where} \left(\frac{\partial \tilde{S}}{\partial T}\right)_{TM} = 0$$

which is itself linked to the mean period by:

$$TH1/3 = 1.41 \quad T_{mean} \ (*) \qquad (25)$$

(*) The empirical relationship used by the C.O.B. buoy in the algorithm to calculate the significant wave period.

In deriving expression [15], TH1/3 is expressed as a function of σ or of H1/3:

$$TH1/3 = 4,44 \sqrt{H1/3} \qquad (26)$$

2.2.3 Parameters affecting wave amplitude and direction

2.2.3.1 Wind action on the sea

2.2.3.1.1 Wave formation and growth under the influence of the wind [21], [22]

(a) Description of phenomenon

Small wavelets or "catspaws" are created on the surface of a calm sea when a gentle breeze begins to blow. These are caused by variations in the pressure put by the breeze on the water.

As it continues to blow, the wind feeds the waves, which move in the same direction. When the wind velocity exceeds about 2 m/s the sea commences to take shape and the catspaws merge into each other. The wavelength and amplitude of the waves increase.

When the wind reaches 5 m/s the speed of increase in height is greater than the speed of increase in wavelength. The wave steepness increases. The waves which have the greatest steepnesses break (since the waves are propagated in groups, breaking takes place in the vicinity of the group). This phenomenon becomes apparent when the mean steepness reaches 8%. When the wind increases further, breaking waves are even more numerous. It is noteworthy that the steepness of an individual wave does not exceed 14% in the open sea.

(b) Classification scales

The wind is often classified by means of the BEAUFORT scale. This scale shows wave height in the case of a sea raised by the wind far from the coast (see Table 2.1).

It is preferable to use the DOUGLAS scale for wave height classification, because it is more accurate in the case of moderate roughness (Table 2.2).

2.2.3.1.2 Wind action on the sea: the concept of fetch

Two sea states at a given point do not depend solely upon the force of the wind blowing locally; they are also dependent upon the distance known as "fetch" over which the wind has acted on the sea [23]. This distance is that covered by the wave under the influence of the wind.

To illustrate this definition, let us assume a point situated any distance from the coast in the direction of a wind of velocity V which begins to blow from the coast towards that point (Figure 2.8).

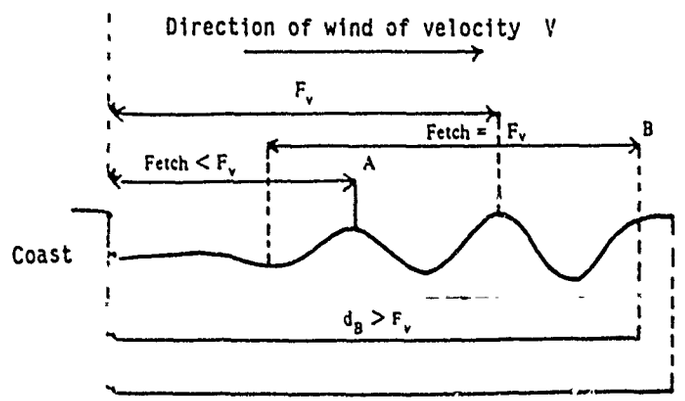

Figure 2.8

-40-

BEAUFORT WIND SCALE
(for a standard height of 10 metres above flat and open ground)

BEAUFORT NUMBER	DESCRIPTIVE TERM	EQUIVALENT SPEED AT A STANDARD HEIGHT OF 10 METRES ABOVE FLAT AND OPEN GROUND				SPECIFICATIONS			PROBABLE WAVE HEIGHT IN METRES*	PROBABLE WAVE HEIGHT IN FEET*
		AVERAGE VELOCITY IN KNOTS	METRES/SEC	KM/H	MPH	ON LAND	IN OPEN SEA	NEAR THE COAST		
0	Calm	< 1	0 - 0.2	< 1	< 1	Calm; smoke rises vertically.	The sea is like a mirror.	Calm.	-	-
1	Light air	1 - 3	0.3 - 1.5	1 - 5	1 - 3	Direction of wind shown by smoke but not by wind vanes.	Ripples form resembling fish scales, but with no foam.	Fishing boats make very slight headway.	0.1 (0.1)	¼ (¼)
2	Light breeze	4 - 6	1.6 - 3.3	6 - 11	4 - 7	Wind felt on face; leaves rustle; ordinary vane moved by wind.	Wavelets, still short but more marked; wave crests glassy in appearance but no breaking.	The wind fills boat sails, which make about 1-2 knots.	0.2 (0.3)	½ (1)
3	Gentle breeze	7 - 10	3.4 - 5.4	12 - 19	8 - 12	Leaves and small twigs in constant motion; wind extends light flags.	Very small waves; crests begin to break; foam glassy in appearance; sometimes a few scattered white horses.	Boats begin to heel over and make 3-4 knots.	0.6 (1)	2 (3)
4	Moderate breeze	11 - 16	5.5 - 7.9	20 - 28	13 - 18	Wind raises dust and loose paper; small branches are moved.	Small waves becoming longer; white horses quite numerous.	Effective moderate breeze; boats carry all their sail and heel over well.	1 (1.5)	3½ (5)
5	Fresh breeze	17 - 21	8.0 - 10.7	29 - 38	19 - 24	Small trees in leaf begin to sway; crested wavelets form on inland waters.	Moderate waves, more clearly elongated in shape, many white horses generated (possibly spray).	Boats shorten sail.	2 (2.5)	6 (8)
6	Strong breeze	22 - 27	10.8 - 13.8	39 - 49	25 - 31	Large branches in motion; telegraph wires whistle; umbrellas used with difficulty.	Small begins to form; crests of white foam more extensive everywhere (normally some spray).	Boats take two reefs in the mainsail; precautions required in fishing.	3 (4)	9½ (13)
7	Moderate gale	28 - 33	13.9 - 17.1	50 - 61	32 - 38	Whole trees in motion; inconvenience in walking against wind.	The sea begins to rise; the white foam from breaking waves begins to be blown in trails in the eye of the wind.	Boats remain in port; those at sea anchor.	4 (5.5)	13½ (19)
8	Fresh gale	34 - 40	17.2 - 20.7	62 - 74	39 - 46	Breaks twigs off trees; generally impedes progress.	Waves of moderate height and greater length; foam of spray begin to break away from their upper crests; foam is blown in well-marked trails in the eye of the wind.	All boats make for port if one is near.	5.5 (7.5)	18 (25)
9	Strong gale	41 - 47	20.8 - 24.4	75 - 88	47 - 54	Slight structural damage occurs; chimney pots and slates are moved.	Large waves; dense trails of foam in the eye of the wind; wave crests begin to shake, collapse and break as rollers; spray may reduce visibility.	-	7 (10)	23 (32)
10	Whole gale	48 - 55	24.5 - 28.4	89 - 102	55 - 63	Rare inland; trees uprooted, considerable structural damage occurs.	Large waves with long plumed crests; the spray builds up in wide banks and is blown in the eye of the wind in thick white trails; the surface seems white overall; breaking of rollers is intensified and sudden; visibility is reduced.	-	9 (12.5)	29 (41)
11	Storm	56 - 63	28.5 - 32.6	103 - 117	64 - 72	Very rarely experienced; accompanied by widespread damage.	Exceptionally high waves (small and medium - sized ships may be lost to sight temporarily); the wind is completely covered by banks of white foam extended in the direction of the wind; the edges of the wave crests are blown everywhere and produce froth; visibility is reduced.	-	11.5 (16)	37 (52)
12	Hurricane	64 - 71 or more	32.7 - 36.9 or more	118 - 133 or more	73 - 82 or more	-	The air is full of foam and spray; the sea is entirely white due to drifting banks of foam; visibility is very greatly reduced.	-	14 (-)	45 (-)

* This Table is designed solely as a rough guide to show what may be expected on the high seas far from the coasts. It should never be used for the converse, i.e. to define or describe the sea state. On inland seas and near coasts with a fetch wind the waves will be lower and steeper. The figures in parentheses show the maximum probable wave height.

Table 2.1: BEAUFORT SCALE

State	Description Term	Significant Wave Height H1/3 (m)
0	Calm	0
1	Smooth	0. - 0.30
2	Slight	0.30 - 0.90
3	Moderate	0.90 - 1.50
4	Rough	1.50 - 2.40
5	Very rough	2.40 - 3.60
6	High	3.60 - 6.00
7	Very high	6.00 - 12.00
8	Precipitous	12.00

Table 2.2

DOUGLAS Scale

For a certain time the sea at this point will rise to a certain height due to the action of the wind; it will then reach a stable level of roughness, although the wind continues to blow. This roughness is a function of the fetch at the point in question.

If the distance d is very great (point B) the waves will reach a maximum amplitude dependent only upon the wind velocity V. The waves will have risen over a fetch F_V of length linked to V.

If, on the other hand, the point is near the coast (point A), the fetch will be too short and the wave amplitude will depend upon the distance to the coast.

2.2.3.2 Wave direction near the coasts

Wave direction near the coast is not solely dependent upon wind direction; it is also governed by the curves of the sea-bed. Wave motion is subject to the influence of the sea-bed when its wavelength is greater than twice the depth (paragraph 2.2.1.2). The minimum period for which it can be assumed that the waves are subject to the influence of the sea-bed relief can be deduced from this analysis and are presented in Table 2.3.

Depth	Minimum Period
10 m	5 s
15 m	6 s
20 m	7 s

Table 2.3

The wave front direction near the coast can be defined if the direction and period of the waves in the open sea are known and the sea-bed chart is available.

Let us assume a sudden discontinuity in the sea-bed where the depth varies from P_1 to P_2. Wave refraction can be written as follows:

$$\frac{\sin \varphi_1}{C_1} = \frac{\sin \varphi_2}{C_2} \qquad (27)$$

where C_1 and C_2 represent the speeds at depths P_1 and P_2;

φ_1 is the angle of incidence and φ_2 is the refracted angle (Figure 2.9).

Figure 2.9

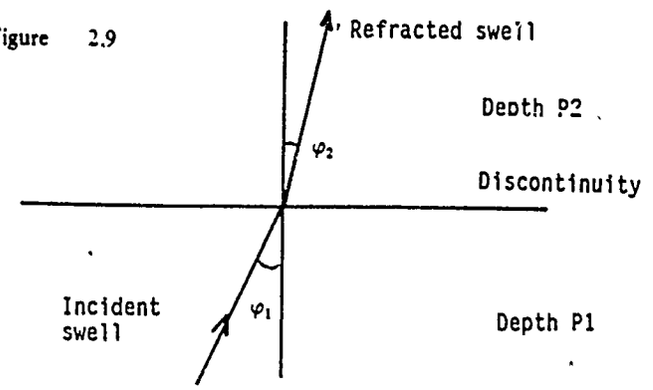

Relationship (27) reveals that the swell, which has a large wavelength, tends to follow a direction perpendicular to the coast when the contour lines of the sea-bed are parallel to the shoreline.

It should be noted that relationship (27) is valid only when the sea-bed gradients are small with respect to the wavelength. In the opposite case, the study is formulated in diffraction terms.

2.3 MILLIMETRE WAVE REFLECTION ON THE SEA AT GRAZING-INCIDENCE

2.3.1. Introduction

Calculation of the electromagnetic signal level reflected on the sea surface has been the subject of many publications since the 1950s. The reasons for this substantial amount of work are:

- the difficulty of representing the random three-dimensional movement of the sea surface mathematically;
- the specific aspects of computation methods according to the frequency band used.

The various figures encountered in the theoretical studies are summarised in Table 2.4 [24], [25]. The sea surface has been defined for this purpose by its longitudinal periodicity L and wave mean amplitude H. The electromagnetic wavelength is indicated by λ_i.

	Low frequency scattering model	High frequency scattering model	Composite model
Conditions	$L < \lambda_i$ $H < \lambda_i$	$L \gg \lambda_i$ $H > \lambda_i$	2 vertical roughness scales $H_1 \ll \lambda_i \quad H_2 > \lambda_i$
Frequency band	Hectometer, decameter, HF band		UHF, centimeter, millimetre band
Calculation method	Perturbation method	Physical or geometrical optics	Physical or geometrical optics (H_2) and perturbation method (H_1)
References	Rice [26] Valenzuela [27] [28] Barrick [29] [19] Wright [30] Broche [32] Ishimaru [31] Augros [33]	Ament [34] Beckman [35] Kodis [36] Karasawa [38] Beard [39] Barrick [37]	Wright [40] Guinard [41] Bass [42] Brown [43] Moore [44] Fung [45]

Table 2.4

It is not the purpose of this paragraph to list these various theories, none of which is entirely applicable to the present situation. Its object is rather to supply a theoretical approach which can be used to analyse the received signal levels for the links which were set up.

It will be assumed for this purpose that the received signal level fluctuations are due solely to the phenomenon of reflection on the sea: disturbances caused by the atmosphere are not considered in this part.

2.3.2 Vector representation of the received signal level

In the absence of disturbances caused by the atmosphere, qualitative study of the received signal levels suggests that the received field E_t can be represented as vectors by the sum of the two components (Figure 2.10):

- the coherent component ($\vec{E}_d$), which is deterministic in nature, is the sum of the field due to direct radiation ($\vec{E}_{dc}$) and the component due to coherent reflected radiation ($\vec{E}_{ic}$);
- the incoherent component ($\vec{E}_a$) arises from the many facets which make up the surface of the sea and which reflect the transmitted field randomly in phase and amplitude.

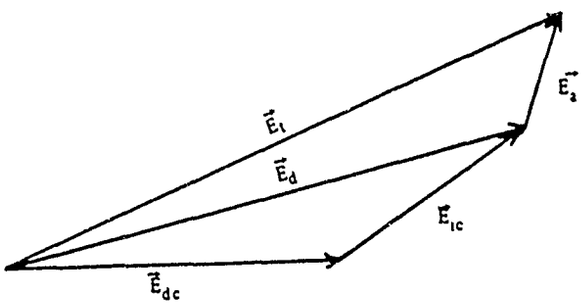

Figure 2.10

This vector sum, which makes it possible to account for fast and slow fluctuations in the received field level, is closely dependent on several factors.

(a) Link geometry

The reflecting surface varies in form according to the location of the link relative to the plane of reflection. This surface should therefore be calculated and its illumination verified for the transmission and reception antennas.

(b) Surface state

The ratio between coherent component and incoherent component is linked to the roughness of the sea surface. The ratio is quantifiable on the basis of experimental received signal level data by virtue of the proposed mathematical modelling. In addition, a coherent reflection model makes it possible to study the coefficient of coherent forward reflection experimentally.

2.3.3 Calculation and illumination of the reflecting surface

2.3.3.1 Definition of FRESNEL ellipsoids

Let us consider a propagation link of wavelength λ linking two points E and R and some point M in space. The length of the direct path will be called R_1 and the length of the indirect path through M will be called R_2 (Figure 2.11).

$R_2 = EM + MR$

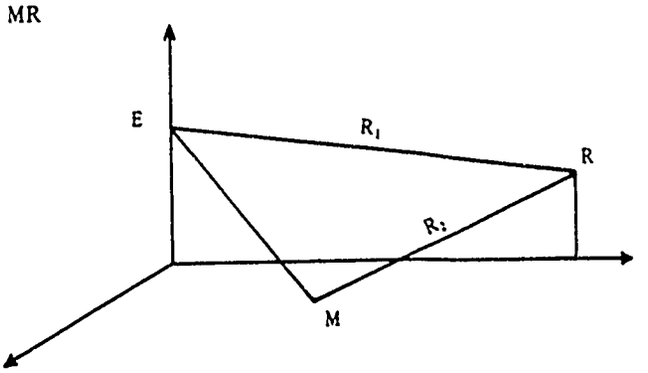

Figure 2.11

By definition the FRESNEL ellipsoid of order n is the locus of points such that the difference in progression $\delta = R_2 - R_1$ is equal to a multiple of the half wavelength:

$$\delta = n\frac{\lambda}{2} \qquad (28)$$

Points E and R are the foci of the FRESNEL ellipsoids. The phase shift in the reflected ray corresponding to two ellipsoids of successive orders is equal to 180°.

NOTE: The greater part of the direct radiation energy is confined to the first FRESNEL ellipsoid. This ellipsoid should not be masked beyond 40% in order to receive a signal which has not been reduced too much in comparison with the free space signal [46]. In the case of the millimetre links under consideration, this first ellipsoid was very narrow, which fully justifies the use of geometrical optics in the computations.

2.3.3.2 Ellipsoid intersection with the surface of the sea, which is presumed smooth

For this type of link with a double path (multipath), the received signal is determined from a knowledge of the signal level reflected on the surface of the sea.

The characteristics of this signal level are closely dependent upon the reflecting surface geometry. The signal retransmitted on the latter is not uniform, but varies in amplitude and phase.

FRESNEL ellipsoid intersection with the surface of the sea (FRESNEL zones) indicates the zones which contribute to the reflected signal level in the same direction. BECKMANN [35] proves that the contribution of the first FRESNEL zone is the most substantial in calculating a reflected signal level.

The geometrical dimensions of the FRESNEL zones are calculated as follows. Illumination of this zone by the transmission and reception antennas is then considered.

2.3.3.2.1 Equation for ellipses in the common frame of reference

Let there be a link of length d, for which the height of the transmission and reception antennas h_e and h_r are known. A FRESNEL ellipsoid cuts the plane representing the flat sea as an ellipse completely defined by the position of its centre relative to the transmission site, its major axis and its minor axis (Figure 2.12). Let us consider the ellipsoid of order n. Its equation in the frame of reference $(\vec{u}_o, \vec{v}_o, \vec{w}_o)$ at Mo $(d/2, 0, h_e + h_r/2)$; frame of reference x y z) comes immediately:

$$b^2 x'^2 + a^2 (y'^2 + z'^2) = a^2 b^2 \qquad (29)$$

where a is the length of the semimajor axis and b is the length of the semiminor axis.

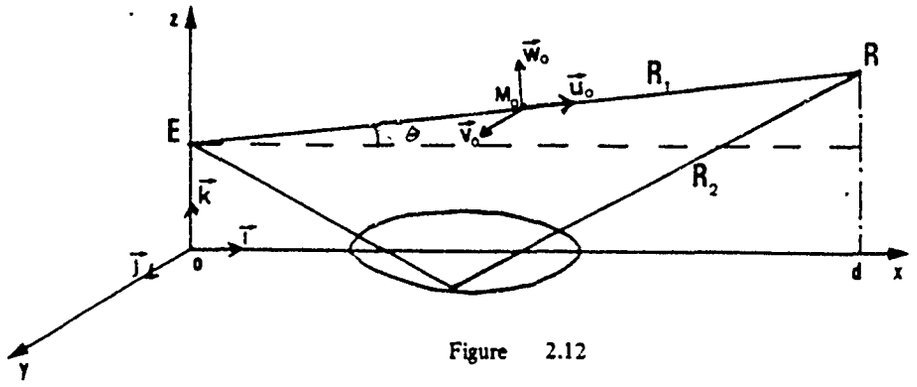

Figure 2.12

The ellipsoids are defined by:

$$R_2 - R_1 = \delta \tag{30}$$

where R_1 is the distance between the foci (called d in the continuation of the presentation) and R_2 is the distance from one focus to the other through any point of the ellipsoid.

The first item in the calculation is to find a and b by examining the ellipse, where the ellipsoid intercepts the plane xoy. It is easily arrived at:

$$\begin{cases} a = \dfrac{\delta + d \cdot \cos\theta}{2} \\ b = \dfrac{1}{2}\left(\dfrac{2\,\delta\, d}{\cos\theta} + \delta^2\right) \end{cases} \tag{31}$$

with θ the angle of ER with the horizontal plane.

2.3.3.2.2 Change of frame of reference

We must now describe the equation for the ellipsoid in the frame of reference xyz; the frame of reference must be changed for this purpose. This involves relocating the frame of reference $(\vec{u}_0, \vec{v}_0, \vec{w}_0)$ at the origin O, then rotating it through angle $-\theta$. The former co-ordinates are linked to the new co-ordinates by the following system:

$$\begin{cases} x' = \left(x - \frac{d}{2} \right) \cos\theta + \left(z - \frac{h_e + h_r}{2} \right) \sin\theta & (32) \\ y' = y \\ z' = - \left(x - \frac{d}{2} \right) \sin\theta + \left(z - \frac{h_e + h_r}{2} \right) \cos\theta & (33) \end{cases}$$

Replacing x', y' and z' by expressions (32) and (33) in equation (29) is sufficient to obtain the ellipse equation in the xy plane. Tedious calculations, [47], lead to the following equation:

$$\left(x - \frac{d}{2} - p \right)^2 \left(b^2 \cos^2\theta + a^2 \sin^2\theta \right) + a\, y^2 = \frac{a^2 b^2 \left(b^2 \cos^2\theta + a^2 \sin^2\theta - C^2 \right)}{b^2 \cos^2\theta + a^2 \sin^2\theta} \qquad (34)$$

with

$$p = - \frac{C \left(a^2 - b^2 \right) \sin\theta \cos\theta}{b^2 \cos^2\theta + a^2 \sin^2\theta} \qquad (35)$$

$$C = \frac{h_e + h_r}{2} \qquad (36)$$

The parameters characteristic of the FRESNEL ellipse are extracted from this equation. Expressions giving:

- the distance x_0 from the centre of the ellipse to the point of transmission;
- the length of the semimajor axis;
- the length of the semiminor axis;

are obtained by introducing the fact that the antenna heights h_e and h_r and the difference between the direct and indirect path are small with respect to the link distance d:

$$x_0 = \frac{d}{2} \frac{1 + \frac{2 h_e (h_e + h_r)}{n \lambda d}}{1 + \frac{(h_e + h_r)^2}{n \lambda d}} \qquad (37)$$

$$X_n = \frac{d}{2} \frac{\sqrt{1 + \frac{4 h_e h_r}{n \lambda d}}}{1 + \frac{(h_e + h_r)^2}{n \lambda d}} \qquad (38)$$

$$Y_n = \frac{\sqrt{n \lambda d}}{2} \sqrt{\frac{1 + \frac{4 h_e h_r}{n \lambda d}}{1 + \frac{(h_e + h_r)^2}{n \lambda d}}} \qquad (39)$$

The area A_n of the ellipse is deduced, knowing that:

$$A_n = \pi X_n Y_n :$$

$$A_n = \frac{\pi d \sqrt{n \lambda d}}{4} \frac{1 + \frac{4 h_e h_r}{n \lambda d}}{\left[1 + \frac{(h_e + h_r)^2}{n \lambda d}\right]^{3/2}} \qquad (40)$$

NOTE: The antenna heights are modified by the following expressions [48] to take account of the curvature of the earth:

$$h_e = h_{e0} - \frac{d_e^2}{2a}$$

$$h_r = h_{r0} - \frac{d_r^2}{2a} \qquad (41)$$

where a is the Earth's radius and d_e and d_r are the distances from the points of transmission and the point of reception to the point of reflection.

2.3.3.3 Analysis of results

2.3.3.3.1 Form of FRESNEL ellipses

The dimensions of the first two FRESNEL ellipses were calculated for the 35 GHz, 36 GHZ and 94 GHz links installed at fixed heights during the 1984-1985 measurement campaign (Table 2.5). $\triangle X_1$ and $\triangle X_2$ show the distances between the first two ellipses on the major axis.

It is observed that the FRESNEL ellipses are greatly elongated in the direction of propagation. Their minor axes measure only a few metres, whereas their major axes are of the order of a kilometre in length.

Transmission frequency		35 GHz	36 GHz	94 GHz
Height of transmission site/sea level		18.8 m	45.2 m	17.8 m
Height of reception site/sea level		13.7 m	10.2 m	12.7 m
n = 1	Distance from ellipse centre to reception point	3,945 m	1,724 m	3,788 m
	Length of semimajor axis	1,695 m	616 m	1,164 m
	Length of semiminor axis	4.47 m	3.4 m	2.71 m
n = 2	Distance from ellipse centre to reception point	4,048 m	1,810 m	3,848 m
	Length of semimajor axis	2,263 m	863 m	1,601 m
	Length of semiminor axis	6.33 m	4.86 m	3.84 m
ΔX_i		465 m	161 m	377 m
ΔX_2		671 m	333 m	497 m
Area of first FRESNEL zone		23,788 m^2	6,580 m^2	9,910 m^2

Table 2.5

FRESNEL ellipses at 35, 36 and 94 GHz
(spherical earth; k = 4/3)

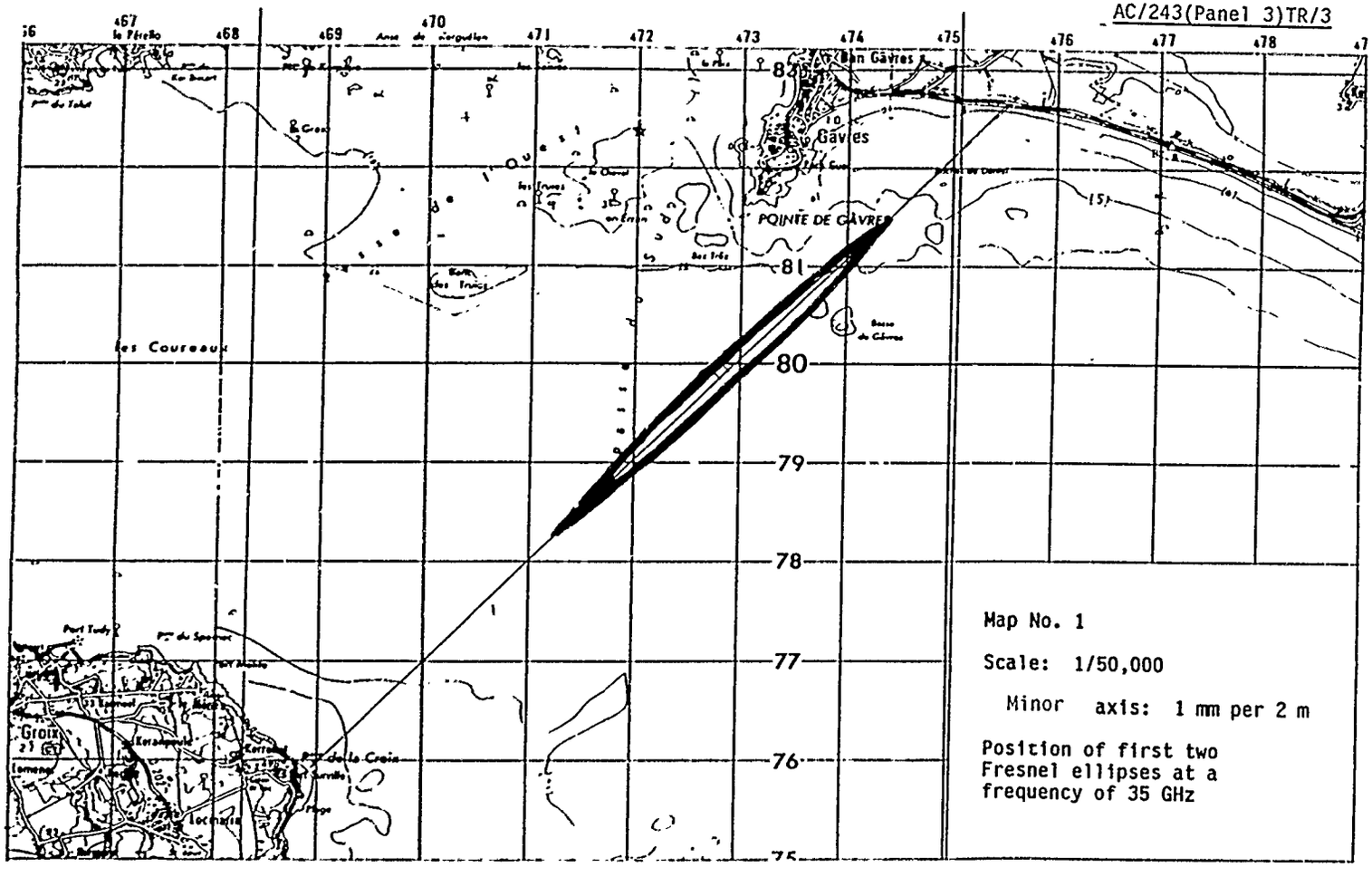

Map No. 1

Scale: 1/50,000

Minor axis: 1 mm per 2 m

Position of first two Fresnel ellipses at a frequency of 35 GHz

-52-

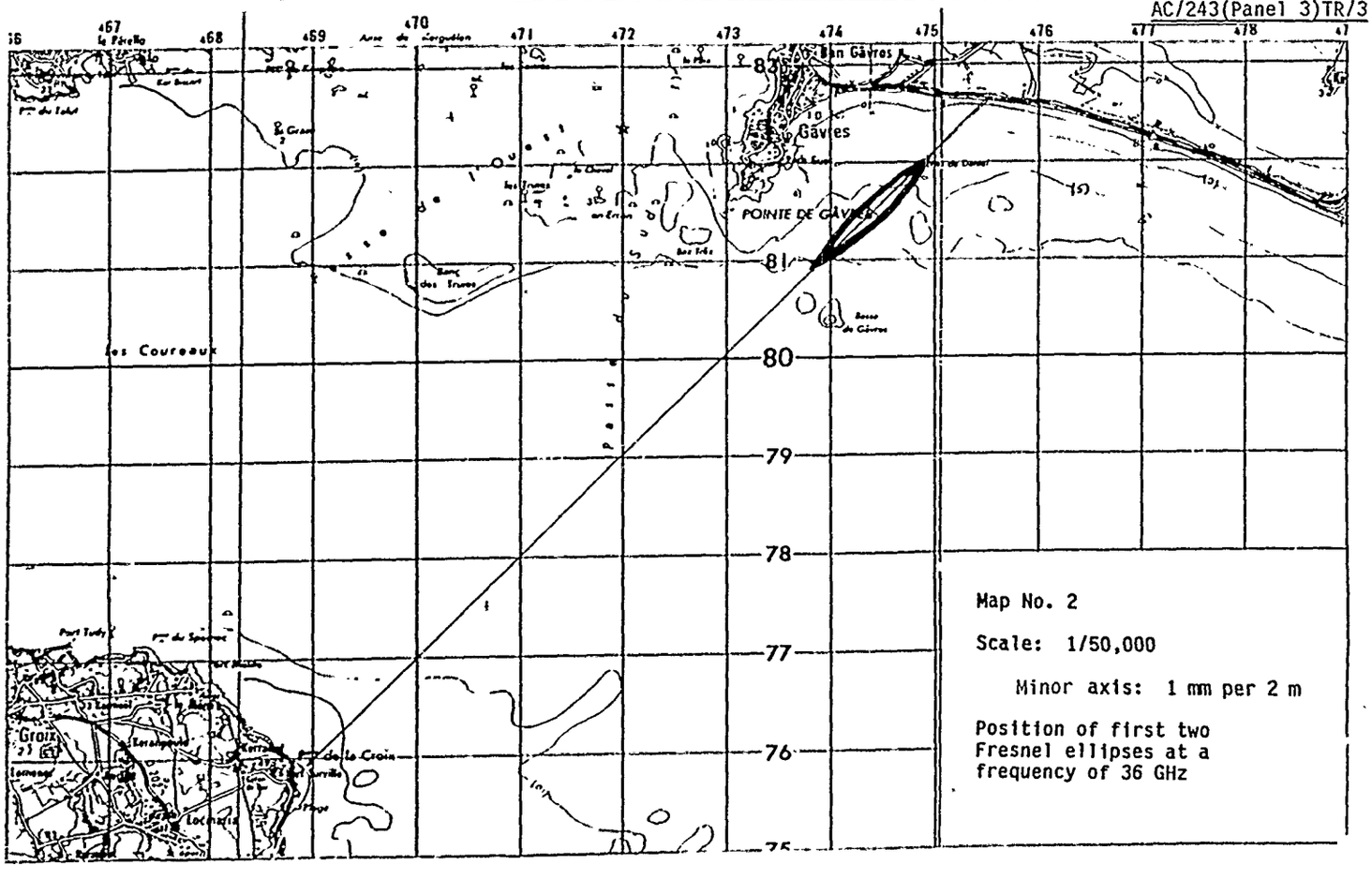
Les Gâvres
POINTE DE GÂVRES
Les Coureaux
Groix
Locmaria
83
82
81
80
79
78
77
76
75
Map No. 2
Scale: 1/50,000
Minor axis: 1 mm per 2 m
Position of first two Fresnel ellipses at a frequency of 36 GHz

-53-

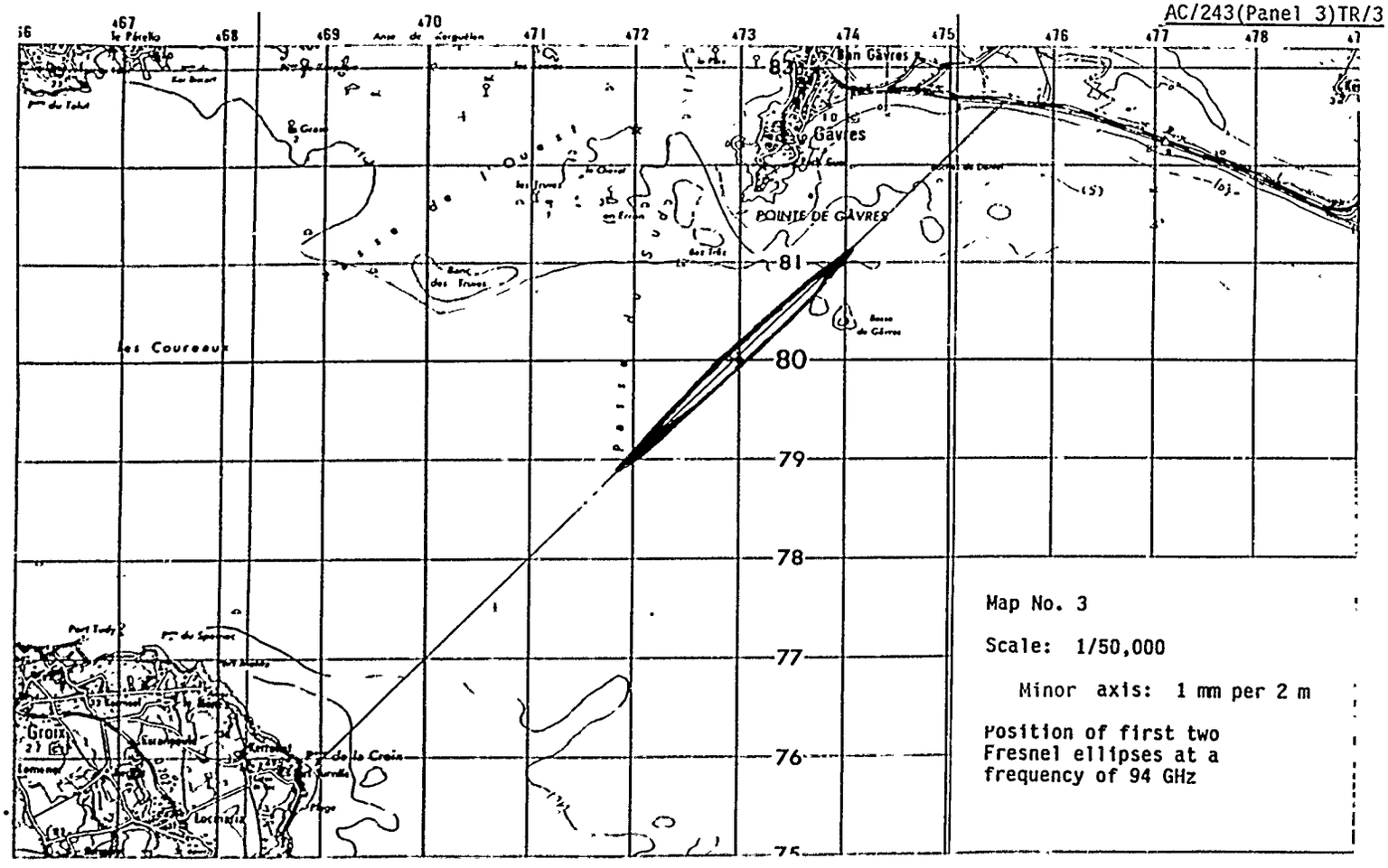
Les Gavres
POINTE DE GÂVRES
Les Coureaux
Groix
Locmaria
Map No. 3
Scale: 1/50,000
Minor axis: 1 mm per 2 m
Position of first two Fresnel ellipses at a frequency of 94 GHz

-54-

2.3.3.4 Position of the first FRESNEL ellipses

In the case of the link operating at 36 GHz, the first FRESNEL ellipses are centred at a distance of about 2 km from the point of reception. This distance for the other links, at 35 GHz and 94 GHz, is about 4 km, the transmitters being at a lower position. It is apparent from maps 1, 2 and 3 that the FRESNEL ellipses are close to the coast where the wave movements are affected by the rise of the sea-bed.

Thus the FRESNEL ellipses relating to the 36 GHz transmission link are just above the sea-bed level curves (depth of the order of 10 m). The waves with long periods ($T > 6s$) then follow a direction perpendicular to the shoreline, in accordance with the law of refraction (paragraph 2.2.3.2). Their direction therefore forms an angle of about 45° with the direction of propagation.

It is difficult to determine wave direction on the FRESNEL ellipses for the 35 GHz link. It is closely dependent upon the wave direction in the open sea.

2.3.3.5 Illumination of FRESNEL ellipses by the transmission and reception antennas

The existence of a reflected path leads to the assumption that the reflecting zone essentially corresponding to the first FRESNEL zone is correctly illuminated by the antenna. Its displacement according to the sea level height has been studied for this purpose for the two extreme receiver heights (mounted on a hoist). Figure 2.13 shows with regard to the 36 GHz system that the ellipse is correctly illuminated by each of the two antennas, the maximum variation in illumination in the zone being less than 2 dB.

NOTE: A downward variation of 4.8 m in the receiver height relocates the reflecting surface about 500 m towards the coast.

2.3.4 Theoretical study of short-term fluctuations

2.3.4.1 Statistical study: RICE distribution

Theoretical study of this type of fluctuation is based on the preceding vector model (paragraph 3.2). The resultant field can be written as follows:

$$\vec{E}_t = \vec{E}_d + \vec{E}_a \qquad (42)$$

where E_d is the deterministic component:

E_a is the random component.

If it is assumed that the phase of $\vec{E}_a$ is distributed uniformly in the interval $[0, 2\pi]$ and that its projections on a two dimensional orthogonal co-ordinate system have a centred Gaussian distribution with the same standard deviation σ, then the fluctuations of the absolute value E_t of the resultant component follow a RICE distribution (Annex V).

$$p(E_t) = \frac{E_t}{\sigma^2} \exp\left[-\frac{E_d^2 + E_t^2}{2\sigma^2}\right] \cdot I_0\left[\frac{E_d \cdot E_t}{\sigma^2}\right] \qquad (43)$$

where $I_0[.]$ is the modified zero-order BESSEL function of the first kind and $\sigma\sqrt{2}$ is the mean square amplitude of the random vector.

When the deterministic amplitude is negligible with regard to the random amplitude, the resultant signal level fluctuations tend towards a Rayleigh distribution.

When the random signal level amplitude is small with respect to the deterministic amplitude, the received signal level fluctuations tend towards a Gaussian type distribution. In this case the surface elements diffuse in a totally random fashion the energy and the central limit theorem can be applied.

Lastly let us note that formula (43), expressed in power terms, can be written as follows (Annex VI):

$$p(P_t) = \frac{1}{P_a} \exp\left[-\frac{P_d + P_t}{P_a}\right] I_0\left[\frac{2\sqrt{P_d P_t}}{P_a}\right] \qquad (44)$$

2.3.4.2 Spectral study

Study of signal level fluctuations may also be tackled by spectral analysis. A simple mathematical formulation makes it possible to link the periodicity of the received signal level to that of the reflecting surface. The conditions for validity of this reasoning are those in which the reflecting surface is displaced in its entirety by a swell movement: the reflection zone, which is presumed to be a point zone, then varies in height at the frequency of the swell.

If it is assumed that this link is short enough for the curvature of the earth to be ignored, the received signal level can easily be expressed as follows (without taking polarisation into account):

$$E_t = E_0 \left(1 + F_t^2 \rho^2 + 2 F_t \rho \cos\theta\right)^{1/2} \qquad (45)$$

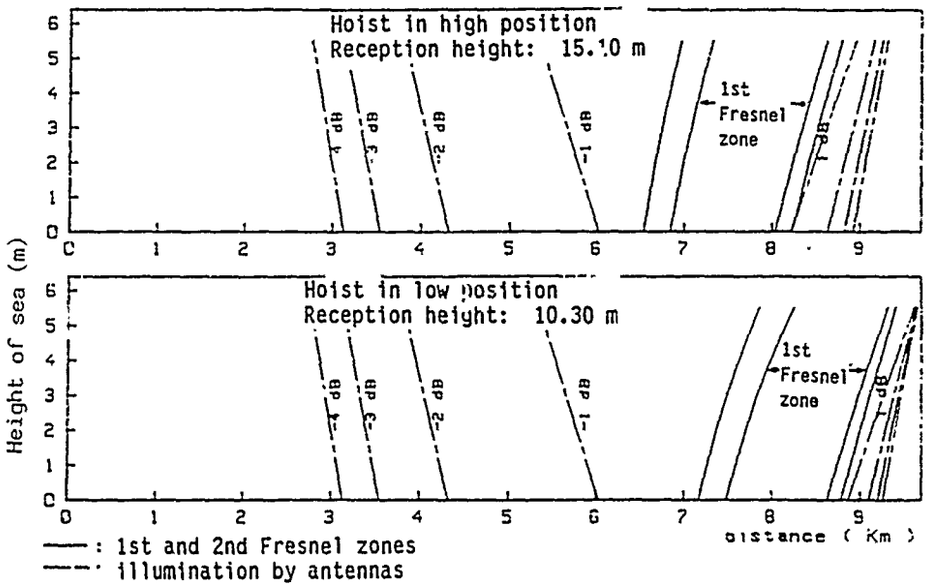

Figure 2.13: Illumination of the first two Fresnel zones by the antennas as a function of mean sea level and receiver height

where E_0 is the incident field;

ρ is the overall forward reflection coefficient of the sea;

F_r is the contribution of the antennas to the indirect path, the antennas being aimed at each other;

θ is the difference in phase between the direct ray and the indirect ray.

$$\theta = \frac{4\pi h_e h_r}{\lambda d} + \pi \tag{46}$$

If the mean sea level varies sinusoidally:

$$\Delta H = \frac{H}{2} \sin \omega t \tag{47}$$

H being the maximum displacement, assumed to be small with respect to the mean antenna heights h_{e0} and h_{r0}, the difference in phase becomes:

$$\theta = \theta_0 + \Delta\theta \sin \omega t \tag{48}$$

$$\theta_0 = \frac{4\pi}{\lambda d}(h_{e_0} h_{r_0}) + \pi \tag{49}$$

$$\Delta\theta = \frac{4\pi}{\lambda d}(h_{e_0} + h_{r_0})\frac{H}{2} \tag{50}$$

In the case of the 36 GHz link, $\Delta\theta$ is 490° with a variation in height of 1 m.

The resultant field takes the following form when 0 in expression (45) is replaced by (48):

$$E_t^2 = E_0^2 \left[1 + F_r^2 \rho + 2F_r \rho \cos(\theta_0 + \Delta\theta \sin \omega t)\right] \tag{51}$$

Development of $\cos(\theta_0 + \Delta\theta \sin \omega t)$ into a BESSEL series leads to the following formulation, expressed in terms of power:

$$\frac{p}{p_0} = B_0 + B_1 \sin \omega t + B_2 \cos 2\omega t + B_3 \sin 3\omega t + \ldots. \tag{52}$$

$$B_0 = 1 + F_r^2 \rho + 2 F_r \rho \cos\theta_0 \; J_0(\Delta\theta)$$

$$B_1 = -2 F_r \rho \sin\theta_0 \; J_1(\Delta\theta)$$

$$B_{2k} = 4 F_r \rho \, J_{2k}(\Delta\theta) \cos\theta_0$$

$$B_{2k+1} = -4 F_r \rho \, J_{2k+1}(\Delta\theta) \sin\theta_0$$

with $J_n(.)$ as an n-order Bessel function of the first kind.

From this development it is apparent that the signal spectrum consists of harmonics of the sea movement. The amplitude coefficient of these harmonics depend upon the link geometry and wave height and decrease with increasing order (B1 to B).

- when the ratio of wave height to incident wave length increases, the number of harmonics above a given threshold is greater;
- when θ_0 is a multiple of $k\pi$ (extreme resultant signal), only the even harmonics are present. The main line at the swell frequency is greatest in the intermediate position between maximum and minimum. In a real situation, in which we are no longer concerned with a point but with a zone of reflection, this observation is not valid.

From the examination of the vector representation of expression (51) it follows that the vector representing the reflected signal varies sinusiodally in phase about the vector $(1 + E_{ic} \cos 0_0, E_{ic} \sin 0_0)$, which vector is determined by the link geometry (Figure 2.14).

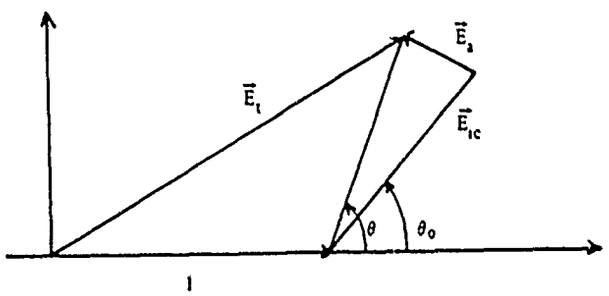

Figure n° 2.14

This vector representation with the inclusion of the incoherent vector E_{ic} can be linked to the general vector model (used for Figure 2.10) by the following equation:

$$E_{ic} \cos(\theta_0 + \Delta\theta \sin \omega t) = E_{ic} \cos \theta_0 + E_{ax}$$

$$E_{ic} \cos(\theta_0 + \Delta\theta \sin \omega t) = E_{ic} \sin \theta_0 + E_{ay} \qquad (53)$$

The incoherent vector standard can then be readily developed into a FOURIER series:

$$E_a = E_{a_0} (D + D_1 \sin \omega t + D_2 \cos 2\omega t + D_3 \sin 3\omega t + \ldots\ldots\ldots) \qquad (54)$$

2.3.5 Theoretical study of long-term fluctuations

Long-term fluctuations are due to the coherent composition of the direct signal level and the coherent reflected signal level. A knowledge of the coefficient of coherent forward reflection is necessary in order to calculate these fluctuations as a function of time or receiver height.

Methods which can be used to calculate this term are set out first in this paragraph, then a model based on coherent reflection is developed.

2.3.5.1 Reflection on a perfectly plane surface

Reflection of an electromagnetic wave on a perfectly plane conducting surface creates an attenuation and a phase shift in the incident wave. The ratio ρ_0 of the reflected electric field strength to the incident electric field strength, called the FRESNEL reflection coefficient, is defined to characterise the surface.

The expression for the incident wave takes a different form according to its polarisation.

Thus in the case of horizontal polarisation:

$$\rho_{0_h} = \frac{\sin\varphi - \sqrt{\epsilon - \cos^2\varphi}}{\sin\varphi + \sqrt{\epsilon - \cos^2\varphi}} \qquad (55)$$

where φ is the angle of incidence of the wave;

$\epsilon = \frac{\epsilon_2}{\epsilon_1}$ is the permittivity ratio between the two media under consideration;

ϵ is expressed as $\epsilon = \epsilon_r - j\,60\,\sigma\,\lambda$ (56)

Where medium 1 is air and medium 2 is sea water of average salinity at 20°C:

$$\left.\begin{matrix}\epsilon_r = 16 \\ \sigma = 55\end{matrix}\right\} \text{ for } f = 36 \text{ GHz}$$

$$\left.\begin{matrix}\epsilon_r = 8 \\ \sigma = 80\end{matrix}\right\} \text{ for } f = 94 \text{ GHz}$$

Similarly in the case of vertical polarisation:

$$\rho_{0_v} = \frac{\sin\varphi - \frac{\sqrt{\epsilon - \cos^2\varphi}}{\epsilon}}{\sin\varphi + \frac{\sqrt{\epsilon - \cos^2\varphi}}{\epsilon}} \qquad (57)$$

NOTE: The case of grazing incidence on the sea. On this assumption, the modulus of ϵ is large with respect to unity. The FRESNEL reflection coefficient is then close to -1; the incident wave has a 180° phase shift:

$$\rho_{0_h} = \frac{\varphi - \sqrt{\epsilon}}{\varphi + \sqrt{\epsilon}} = -1 + \frac{2\varphi}{n}$$

$$\rho_{0v} = \frac{\varphi - \frac{1}{\sqrt{\epsilon}}}{\varphi + \frac{1}{\sqrt{\epsilon}}} = -1 + 2n\varphi \qquad (58)$$

where n is the refractive index of the water.

2.3.5.2 Reflection on a rough surface

2.3.5.2.1 Theoretical calculation

The calculation technique used is based upon the physical optics method. A certain number of hypotheses regarding the surface are assumed to develop the theory:

1. The radius of curvature of the reflecting elements is clearly greater than the incident wavelength. This is the physical optics approximation.

2. Multiple scattering is ignored.

3. Shadow effects are not taken into account in the case of grazing-incidence links.

Subject to these hypotheses, AMENT [34] proposed a theoretical calculation in 1952 for the coherent reflected field strength, taking the statistical characteristics of the illuminated surface into account. He examined a linearly polarised wave illuminating a mono-dimensional rough surface which was a perfect conductor. Using MAXWELL equations and using the description of this surface he arrived at a set of integral equations relating to the averaged surface currents. To arrive at a solution, he assumed on the one hand that the current surface density is solely a function of altitude and on the other hand that the indirect current is that of the plane tangent to the point under consideration (the assumptions relate to hypotheses 3 and 1). AMENT then links the coefficient of coherent forward reflection to the probability density p (h) of the surface heights.

$$\rho_c = \int_{-\infty}^{+\infty} \exp (- 2 i k h \sin \varphi) . p (h) d h \qquad (59)$$

where $k = 2\pi/\lambda_i$ is the wave number of the incident wave;

φ is the angle of incidence of the wave relative to the mean altitude plane.

Application of this expression to the case of a Gaussian surface leads to the following:

$$\rho_c = \exp [- 2 (2 \pi g)^2] \qquad (60)$$

where g is the roughness of the sea;

$$g = \frac{\sigma \sin \varphi}{\lambda_i} \qquad (61)$$

σ being the mean square height of the surface.

Taking the same hypotheses into account, BECKMAN [35] developed a different theoretical calculation leading to AMENT's expression (60).

In the same document he deals with the case of reflection on a surface of finite conductivity. For a steady-state random process, he uses the physical optics approximation in order to justify that the coefficient of coherent forward reflection, can be written as the product of two terms:

$$\rho_s = \rho_0 \times \rho_c \qquad (62)$$

where ρ_0 is the coefficient of FRESNEL reflection of the plane surface of the same nature as the surface under consideration, and ρ_c is the coefficient of forward reflection of a perfectly conducting surface of the same roughness.

Expression (62) is verified even better when the reflection surface is small in size and slightly rough.

More recently, MILLER et al. [49] have deduced a new expression for ρ_c on the basis of experiments by BEARD [2]. They assume that the surface varies like a sine wave over a period of observation, the sine wave amplitude distribution being Gaussian and its phase being uniformly spread over $[-\pi/2, \pi/2]$. This representation introduces the periodic aspect of sea movement.

Subject to these hypotheses, and applying expression (59), the coherent reflection coefficient can then be written:

$$\rho_c = \exp\left[-2(2\pi g)^2\right] I_0\left[2(2\pi g)^2\right] \qquad (63)$$

where $I_0[.]$ is the modified zero-order BESSEL function of the first kind.

2.3.5.2.2 Dependence of the coefficient of coherent reflection with grazing incidence upon wave height and angle of incidence

Charts provide the roughness of the sea and the coefficient at 36 GHz in the case of grazing links (Fig. 2.15'. They illustrate expressions (61) and (63).

Where wave heights are constant, ρ_c shows slight linear variation as a function of the angle of incidence. The ρ_c is highest when the antenna clearance above the water is lowest (the roughness of the sea is then less pronounced).

When the sea passes from state 1 to state 3 on the Douglas scale, ρ_c decreases greatly: the disturbance of the sea, defined by its significant wave height or mean square height, seems to be the dominant parameter for this type of grazing-incidence link.

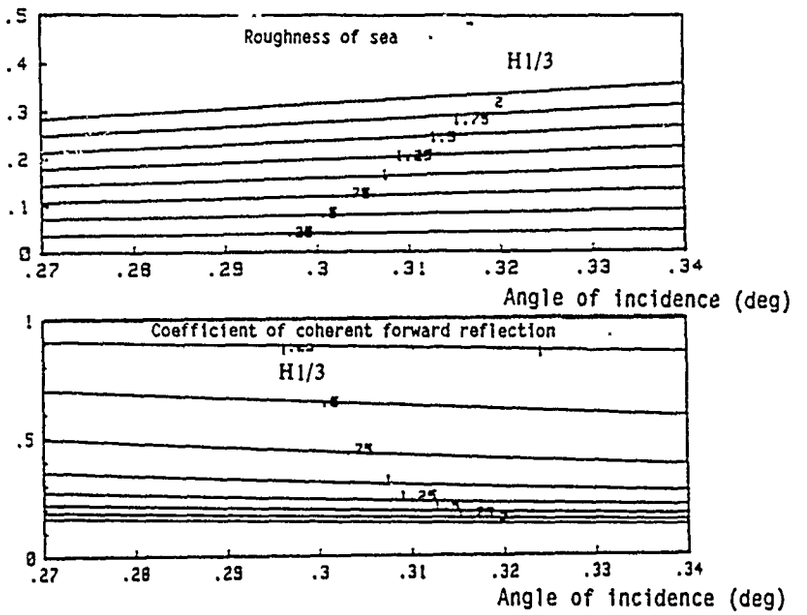

Transmission frequency: 36 GHz

Figure 2.15: Roughness of sea and coefficient of coherent forward reflection at 36 GHz for a grazing incidence link

2.3.5.3 Model based on coherent reflection

A model which takes account of slow fluctuations due to the tide can be set up if the coefficient of coherent forward reflection is known. It is reasonable to advance the following hypotheses in order to simplify the calculation of the resultant signal level:

- atmospheric attenuation is identical on the direct and indirect paths;
- the effect of the depolarisation of the reflected wave on the sea surface due to roughness is ignored. Since the incident wave is polarised linearly, its specular component after reflection on a surface of high conductivity and with radii of curvature which are large with respect to the incident wavelength is not depolarised;
- the variation in the index of atmospheric refraction as a function of altitude is linear and constant in time (the case of the standard atmosphere, dealt with in detail below).

The requirement for precise calculations makes it necessary to regard the earth as spherical, due to the presence of a refractive index gradient modifying the ray trajectory and due to a link length which is sufficiently large with respect to the Earth's radius.

That is the object of this paragraph, which aims to set out all the difficulties involved in determining the resultant signal level.

2.3.5.3.1 Propagation in a standard atmosphere

Millimetre wave propagation in the clear atmosphere is comparable to the propagation of optical light. It is therefore particularly sensitive to the refractive index of the air n, an index which is dependent upon the physical characteristics of the layer through which the waves pass.

Since n is very close to unity, the co-index of refraction N is usually associated with it:

$$N = 10^6 (n - 1) \tag{64}$$

which is expressed in terms of meteorological parameters obtainable by measurement:

$$N = \frac{77.6}{T} \left(p + 4810 \frac{e}{T}\right) \tag{65}$$

where e is the water vapour pressure;
T is the absolute temperature (in K);
p is the atmospheric pressure (in mb).

The ray trajectory is governed by the variation in the refractive index as a function of altitude. A mean value for this rate, which corresponds by convention to the standard atmosphere, has been generally accepted [50] on the basis of a large number of measurements:

$$\frac{dN}{dh} = -\frac{1}{4a} = -40 \text{ N units/km} \tag{66}$$

where a is the Earth's radius (in km).

The negative gradient leads to curvature of the rays towards the ground. Their trajectory is in fact defined by the differential equation deduced from the laws of refraction:

$$\frac{d^2 h}{dx^2} = -10^6 \frac{dN}{dh} = \frac{1}{r} \tag{67}$$

where r is the radius of curvature of the electromagnetic ray and x is the horizontal co-ordinate.

The relative curvature of the electromagnetic ray relative to the curvature of the Earth is then 1/a - 1/r.

This observation introduces the concept of equivalent Earth radius R = ka, deduced from a and r by the following equation:

$$\frac{1}{a} - \frac{1}{r} = \frac{1}{R} = \frac{1}{ka} \tag{68}$$

The rays are propagated in a straight line on such a terresterial sphere.

The value of k is then immediately deduced on the basis of the previous expression:

$$k = \frac{1}{1 - \frac{a}{r}} = \frac{1}{1 + a\frac{dn}{dh}} \tag{69}$$

In a standard atmosphere with $\frac{dN}{dh} = -40$ N° units/km: $k = 4/3$.

2.3.5.3.2 Calculating the difference in path between direct ray and reflected ray

Let there by a spherical surface of radius R = 4.a/3, on which a link is established between two points of respective altitutde h_e and h_r (Figure 2.16).

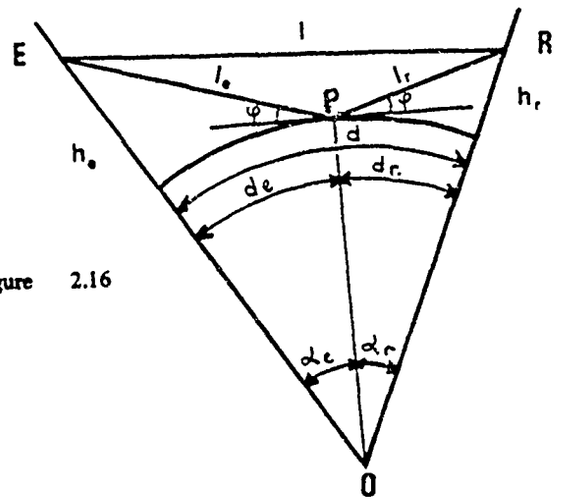

Figure 2.16

The difference in travel between direct ray and reflected ray is calculated by applying the relationship for any triangles to the triangles EPO and RPO.

By assuming

$$b = \frac{d_e - d_r}{d_e + d_r} \tag{70}$$

$$c = \frac{h_e - h_r}{h_e + h_r} \tag{71}$$

and

$$m = \frac{1}{4} \frac{d^2}{(h_e + h_r)\, R} \tag{72}$$

a third-degree b equation in the following form is arrived at:

$$m\,b^3 - (m+1)\,b + c = 0 \tag{73}$$

with $|c|$, $|b|$ and m less than 1.

Its solution is written as follows:

$$b = 2\sqrt{\frac{m+1}{3m}}\cos\left[\frac{\pi}{3} + \frac{1}{3}\,\mathrm{Arccos}\left\{\frac{3c}{2}\cdot\sqrt{\frac{3m}{(m+1)^3}}\right\}\right] \tag{74}$$

This makes it possible to arrive at the angle of incidence on the reflecting surface:

$$\varphi = \frac{h_e + h_r}{d}\,[\,1 - m\,(1+b^2)\,] \tag{75}$$

and the difference in path Δ :

$$\Delta = \frac{(h_e + h_r)^2}{2d}\,(1-b^2)\,[\,1 - m\,(1+b^2)\,]^2 \tag{76}$$

The difference in path may vary significantly when the receiver is moved vertically. The received signal level then passes through a certain number of extrema separated by the distance:

$$\delta h_r = \frac{\lambda d}{4 h_e}\,\frac{1 + m\,(1-b^2)}{1 - m\,(1+b^2)} \tag{77}$$

This expression becomes simpler in the flat Earth approximation:

$$\delta h_r = \frac{\lambda \cdot d}{4 h_e} \tag{78}$$

Numerical application to the Lorient site shows that moving the reception antenna a few metres is sufficient to give rise to interference figures:

f (GHz)	h_e	h_r
35	18.8	1.10 m
36	48.2	0.42 m
94	17.8	0.43 m

Table 2.6

2.3.5.3.3 Beam divergence factor

Reflection of the incident energy on the spherical surface creates an energy dispersion by enlargement of the beam.

Since the energy density received by the reception antenna is inversely proportional to the intersection of the direct and reflected solid angles with the reception plane, this effect tends to reduce the contribution of the reflected radiation relative to direct radiation.

This is why the curved surface divergence factor D is introduced. As before, it is expressed as a function of parameters m and b:

$$D = \left(\frac{1 - m(1 + b^2)}{1 + m(1 - 3b^2)} \right)^{1/2} \qquad (79)$$

2.3.5.3.4 Antenna radiation diagram

The propagation link employed during this experiment has a very small grazing angle. Since the beamwidth of the employed antennas is also small, the gain of these antennas into the direction of the direct path and of the indirect path has to be obtained.

The antennas were aligned optically at the beginning of the experiment. The alignment was carried out at the low position at the reception site when the hoist was used. The most general study case has been the one with the receivers located on the hoist (Figure 2.17).

If F(.) represents the radiation diagram for antennas presumed to be identical, their contributions in the case of a direct field (d) and an indirect field (i) take the following forms (with $h_e > h_r$):

$$F_d = F_{de} \cdot F_{dr} = F^2 (\alpha_0 - \alpha) \qquad (80)$$

$$F_i = F_{ie} \cdot F_{ir} = F (\theta_e - \alpha_0 + \alpha) \cdot F (\theta_r + \alpha_0 - \alpha)$$

where α_0 is the aiming angle at the low site:

$$\alpha_0 = \text{Arctg} \left[\frac{h_e - h_{rb}}{d}\right] \qquad (81)$$

and α is the angle of inclination of the direct ray relative to the horizontal:

$$\alpha = \text{Arctg} \left[\frac{h_e - h_r}{d}\right] \qquad (82)$$

$$F_d = F_{de} \cdot F_{dr} = F^2(\alpha_0 - \alpha)$$

$$F_i = F_{ie} \cdot F_{ir} = F(\theta_e - \alpha_0 + \alpha) \cdot F(\theta_r + \alpha_0 - \alpha)$$

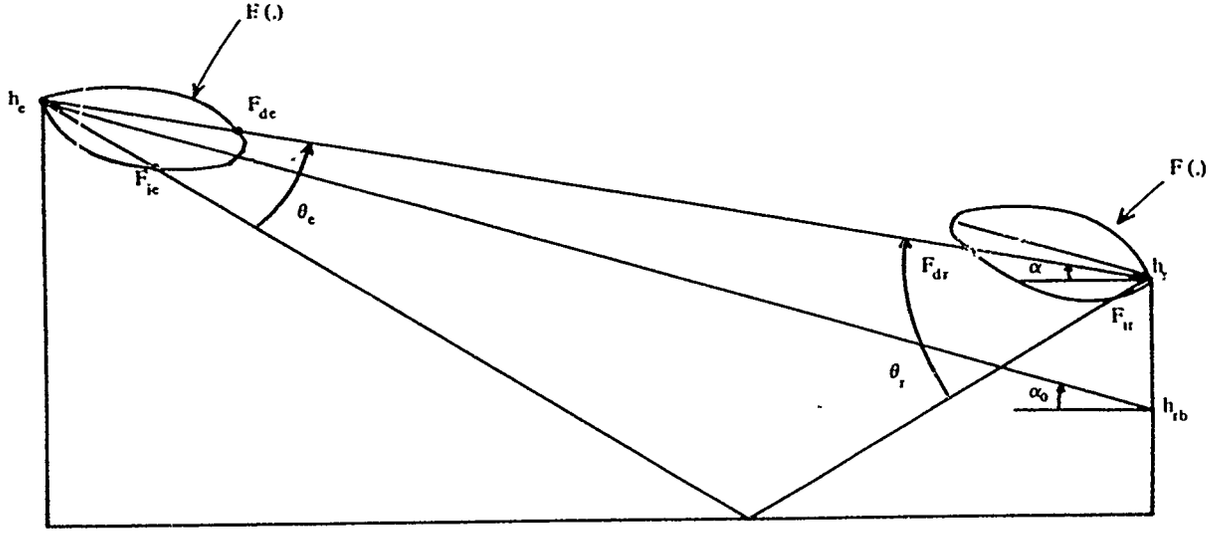

Figure 2.17

θ_e, θ_r is the angular difference on transmission and reception between the direct and indirect rays.

$$\theta_e = \varphi\ (1 - b)$$
$$\theta_r = \varphi\ (1 + b) \qquad (83)$$

where φ is the angle of incidence (expression 75).

2.3.5.3.5 Resultant signal

Following the hypotheses stated at the beginning of this paragraph, the received signal standard takes the following simple form:

$$E_d = (E_{dc}^2 + E_{ic}^2 + 2\, E_{dc} E_{ic} \cos\theta\ )^{1/2} \qquad (84)$$

where θ represents the difference in phase between the direct signal level and indirect signal level:

$$\theta = \frac{2\pi\Delta}{\lambda_1} + \theta_0 \qquad (85)$$

where θ_0 is the difference in phase due to the reflection on the water which value is close to 180°.

The direct and reflected signal amplitude can be deduced as a function of the transmitted signal E_0 by the previous relations:

$$E_{dc} = A.\, F_d\, E_0$$
$$E_{ic} = A.\, \rho_0\, \rho_c\, D\, F_i\, E_0 \qquad (86)$$

expressions in which A characterises atmospheric attenuation.

2.3.6 Space and frequency agility

In order to reduce long-term attenuations, agility techniques which are based on link "duplication" can improve the transmission quality.

The measurements performed at different antenna heights will supply the essential information for this agility technique.

2.3.6.1 Space agility

The difference in height Δh of the reception antenna relative to two successive extrema is almost constant (see Figure 3.23 and Chapter II, paragraph 3.5.3). Consequently, two reception antennas separated by Δh or by $(2n + 1) \Delta h$, n being an integer number, receive opposite phases. Slow fluctuations in signal levels can be considerably reduced by appropriate processing of the signals received by the two antennas.

2.3.6.2 Frequency agility

An attempt is made here to vary the transmission frequency f_i by Δf_i so that the interference figures measured at frequency f_i are opposite in phase to those measured at $f_i + \Delta f_i$.

With the flat Earth approximation, the differences in phase $\theta(fi)$ of the direct signal relative to the reflected signal can be written as follows (expression 76 and 85, Chapter II, paragraph 3.5.3).

For frequency f_i:

$$\theta(f_i) = \frac{4\pi h_e h_r f_i}{c d} + \theta_0 \quad (\theta_0 \approx 180°) \tag{87}$$

where c is the speed of light.

For frequency $f_i + \Delta f_i$:

$$\theta(f_i + \Delta f_i) = \frac{4\pi h_e h_r (f_i + \Delta f_i)}{c d} + \theta_0 \tag{88}$$

By making their difference equal to π, the necessary difference in frequency can be calculated directly:

$$\Delta f_i \text{ (GHz)} = 1. \frac{c d}{4 h_e h_r} . 10^{-9} \tag{89}$$

This difference is 1.6 GHz for f_i = 36 GHz.

Frequency agility makes it possible to establish a link free from the double path phenomenon at any moment.

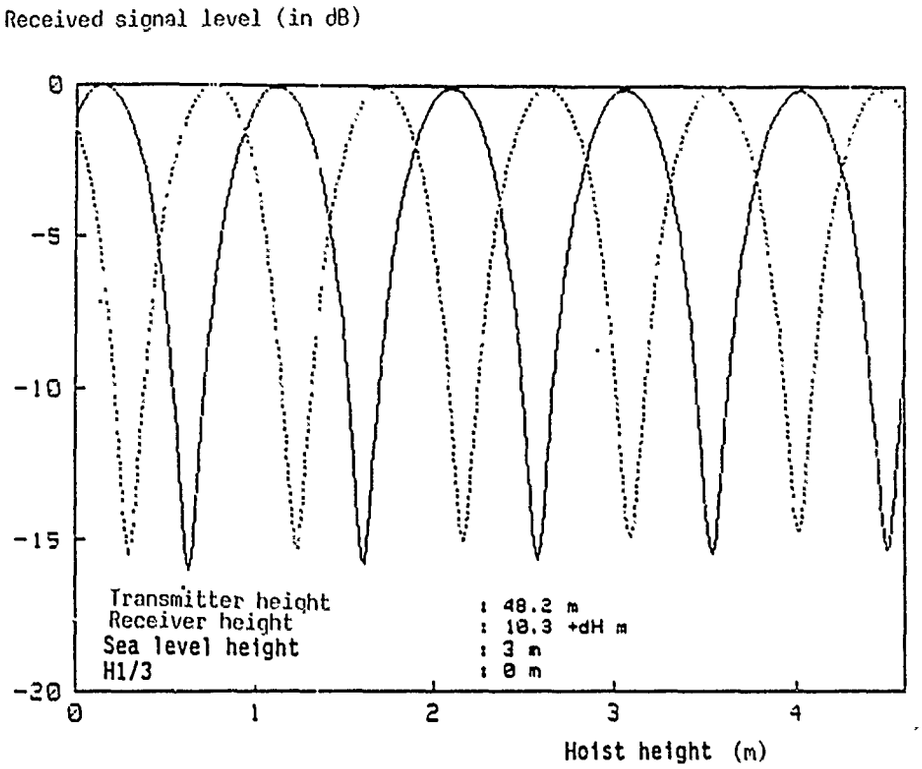

Figure 2.18: Space and frequency agility: received signal level as a function of hoist height and transmission frequency
(- : 36 GHz; ....: 37.6 GHz)

CHAPTER III

EXPERIMENTAL STUDY OF THE PHENOMENON OF REFLECTION ON THE SEA

3.1 PROCESSING OF OCEANOGRAPHIC DATA

All the data processed relates on the one hand to autumn-winter 1984-1985, during which weather conditions were rather bad and on the other hand to the month of August, summer 1986.

These data were analysed with a view to:

- gaining a good knowledge of the sea surface, particularly in the reflection zone;
- validating hypotheses relating to the significant parameter extraction algorithm.

With this in view, theoretical expressions linking significant wave height, significant wave periods and wind speed (defined in Chapter II, paragraph 2.2.2.4) are verified mainly on the basis of data from the 1984-1985 campaign.

Statistical analysis of sea movement is approached subsequently on the basis of measurement of instantaneous variations in sea level in 1986.

3.1.1 Order of magnitude of parameters

Table 3.1 shows the order of magnitude of the values collected during the 1984-1985 campaign.

	Minimum value	Mean value	Maximum value
Hl/3	0.3 m	1 m	5 m
THl/3	3.2 s	5.5 s	9 s
λ	15 m	50 m	100 m

Table 3.1

It can be seen from this that the maximum significant wave height reaches 5 m (during a storm in November).

The sea was also very calm for several days: at the beginning of December (the 10th, 11th and 12th) the significant height stayed below 0.6 m for more than 48 hours.

3.1.2 Sea roughness as a function of wind speed

3.1.2.1 Sea raised by the wind

In situations in which the sea is raised by the wind (where $H1/3 > 1.5$ m) it is apparent that the roughness of the sea is closely dependent upon wind speed (Figure 3.1). An increase in wind speed is accompanied by an increase in the significant wave height. The roughness of the sea diminishes when the wind slackens, but more slowly.

This dependence is also illustrated by Figures 3.2a and b, representing on the one hand the significant wave height of the waves H1/3 as a function of wind speed and on the other the period TH1/3 as a function of H1/3. The curves relating to expressions (24) and (26) in Chapter II, paragraph 2.2.2.4 deduced from the PIERSON-MOSKOWITZ analysis have also been drawn.

It is noteworthy that the experimental points showing the significant wave height as a function of wind speed show relatively widely spread points, and the corresponding line of least squares fits the measurements better than the PIERSON-MOSKOWITZ expression.

This result is explained in the following observations:

- Failure to take wind direction into account

Wind direction should be taken into account to obtain closer agreement. In fact the observation point is close to the shoreline and coast effects, such as the limitation of fetch in the case of winds in the north and east sectors, occur. Similarly, in the case of strong south-westerly winds, the île de GROIX provides protection against roughness from the open sea.

- Constant superposition of several wave movements

Several movements differing in nature are superimposed in certain situations. In particular, heavy swells from the Atlantic independent of the wind are observed in the region. They create additional roughness.

- Narrow spectrum assumption not systematically verified

The algorithm presupposing the shape of the spectrum is a cause of error with wide-band movements.

On the other hand, the significant wave period-significant wave height diagram is less dispersed. It fits well with the theoretical expression, subject to the above observations.

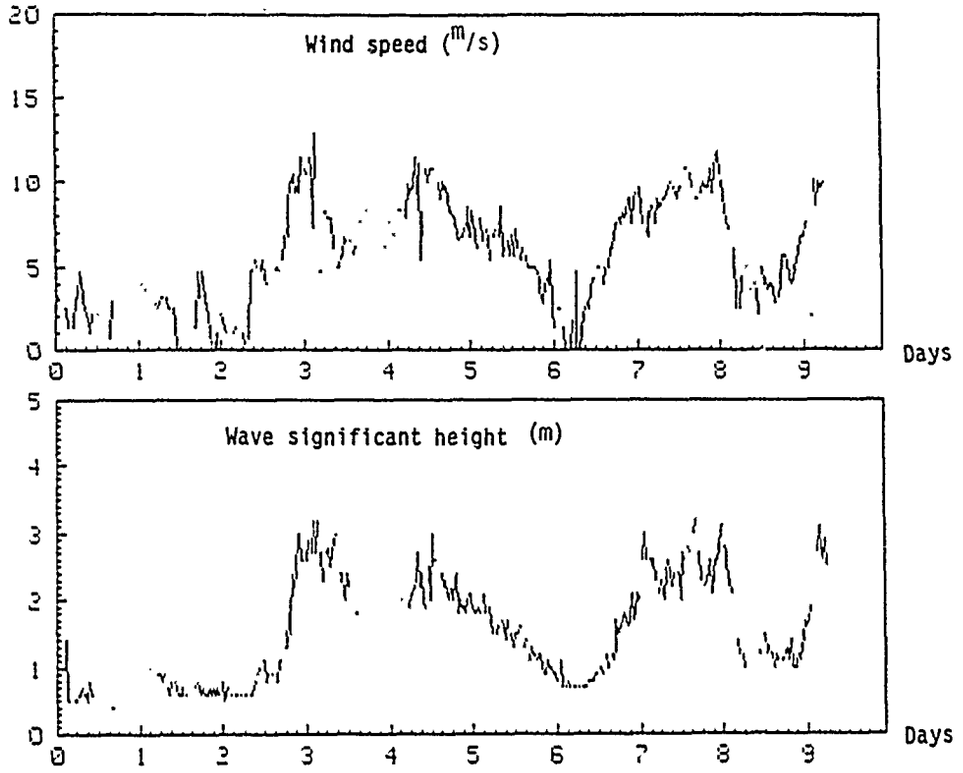

Figure 3.1: Time plot of wind speed and significant wave height over a 10-day period

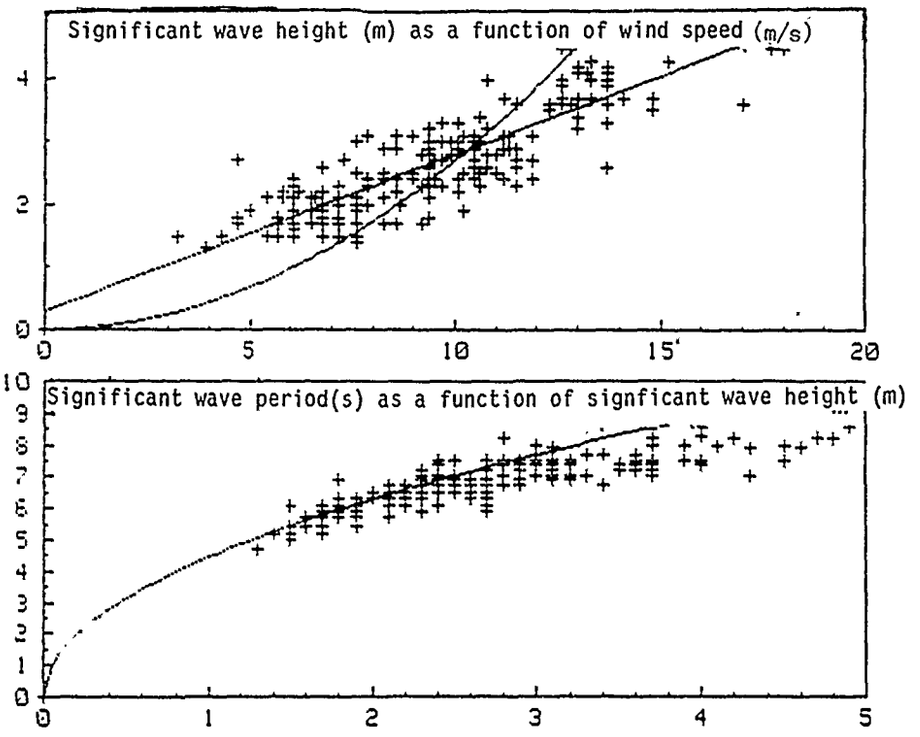

Figure 3.2 a & b: Buoy measurements in a sea raised by the wind

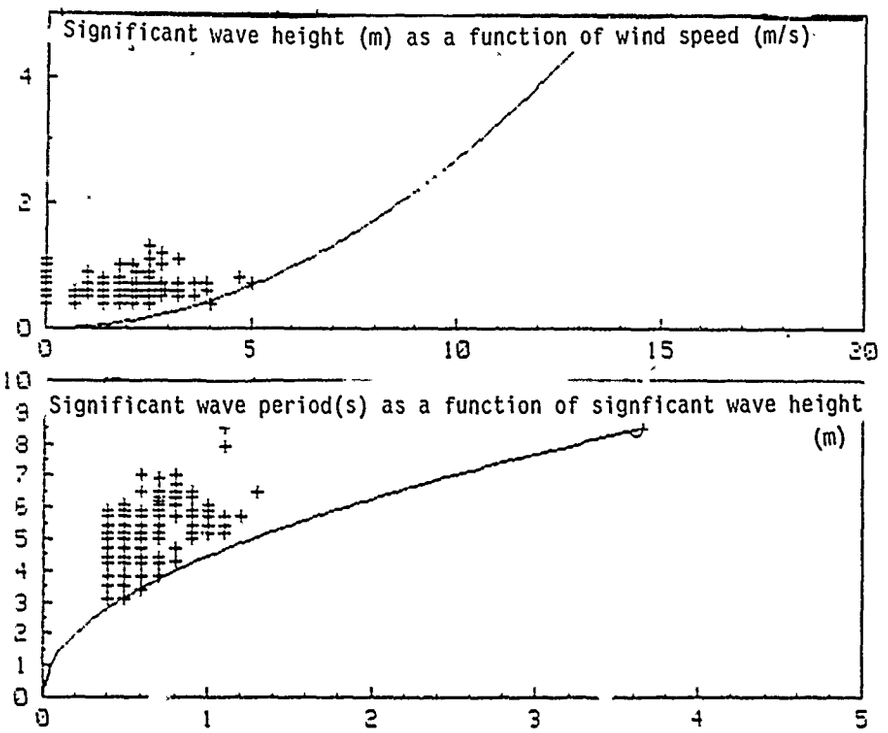

Figure 3.3 a & b: Buoy measurements in a calm sea

3.1.2.2 Sea roughness with light or zero wind

Measurements taken with a light wind (Figures 3.3a and b) were processed in the same way. During these periods the measurement points are all above the curves deduced from the PIERSON-MOSKOWITZ expression. It should be noted in particular that significant wave heights of more than 1 m are recorded in the absence of wind. The roughness of the sea is then due to the swell movement, which is characterised by high dominant periods.

3.1.3 Relationship between significant wave period and mean period

The wave measurement buoy anchored in 1986 supplied regular data on the mean period Tmean and the significant wave period TH1/3. The validity of the expression linking these two parameters can therefore be judged in this experimental context.

The measurement points relating to seas raised by the wind are plotted in Figure 3.4. Expression (25) from Chapter II, paragraph 2.2.4 is plotted as a fine line, whereas the mean square plot is shown as a thick line:

$$TH1/3 = 2.22\ Tmean - 3.511 \qquad (1)$$

These two curves are in fact close to each other in the area studied. Their maximum separation does not exceed 0.4 s in the period interval between 4 and 8 s.

3.1.4 Statistical analysis of instantaneous sea levels

It was possible to record instantaneous variations in sea level at the rate of 1 or 8 Hz for a week at the end of August 1986.

The wave hydrodynamic spectrum was calculated using a fast FOURIER transform programme. This study is tackled in paragraph 3.2.2.2 jointly with the signal spectrum study.

The instantaneous level distribution was also studied and compared to the normal distribution, using first HENRY's graphic method [51], then PEARSON's numerical analysis [52] (Fig. 3.5).

The measurement points are aligned in the plots as a whole, except at the extremities, because the actual distribution is limited. The values of the parameters calculated as part of the PEARSON's analysis (k, β_1, β_2) are close to those corresponding to a normal distribution.

The normal distribution is therefore a satisfactory statistical representation in the case of instantaneous sea level heights, considering the accuracy of the measurements supplied by the buoy.

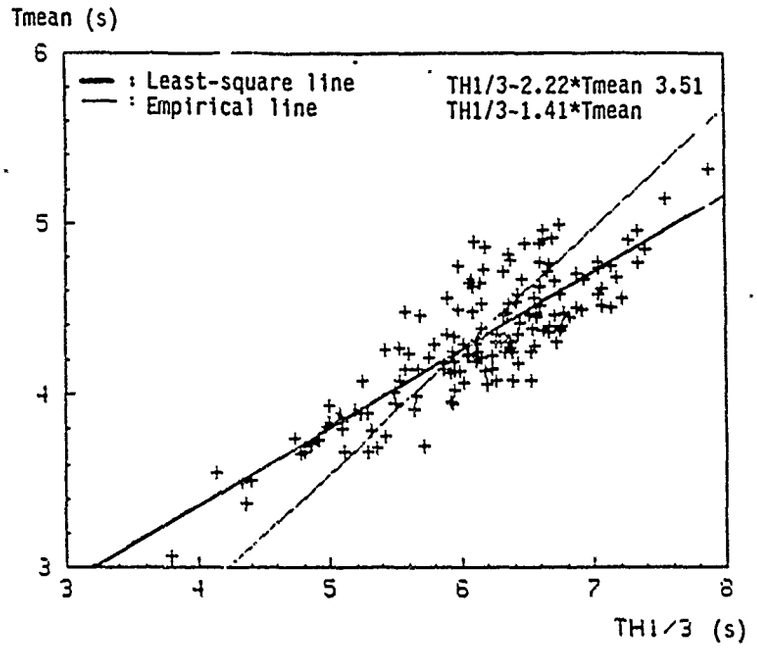

Figure 3.4: Relationship between significant wave period TH1/3 and mean period Tmean

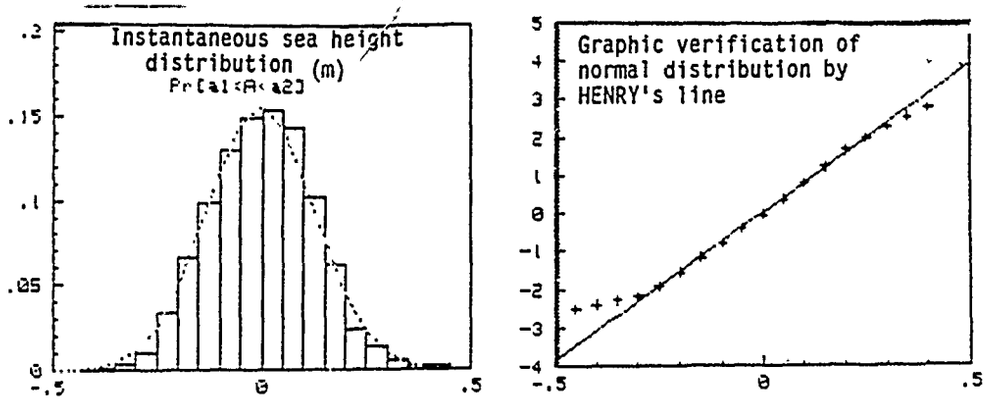

PEARSON numerical analysis (*) : $\beta_1 = 0{,}008$, $\beta_2 = 3{,}078$, $k = 0{,}046$

21 - 08 - 1986 at 18h (H1/3 = 0.35 m)

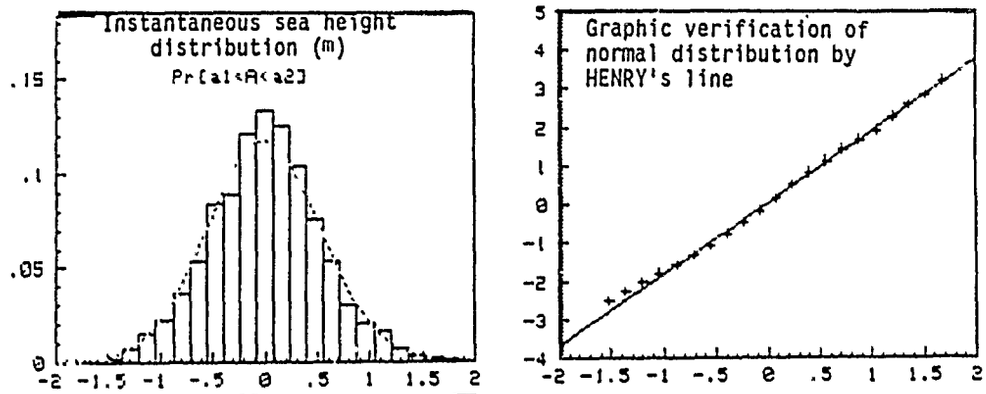

PEARSON numerical analysis (*) : $\beta_1 = 0{,}027$, $\beta_2 = 3{,}058$, $k = 0{,}0189$

25 - 08 - 1986 at 22h30 (H1/3 = 1.75 m)

Figure 3.5 a & b: Statistical study of instantaneous sea level fluctuations

(*) The sample studied follows a normal distribution if $\beta_1 = 0$, $\beta_2 = 3$ & $k = 0$

3.2 EXPERIMENTAL STUDY OF SHORT-TERM FLUCTUATIONS

3.2.1 Processing tools

3.2.1.1 Fast FOURIER transform

A fast FOURIER transform programme based on the COOLEY-TUCKEY algorithm was applied to time sections of 1,024 points in order to find the spectral density of the received signal.

The sampling period during the two measurement campaigns was 1 Hz and 8 Hz. The frequency spectrum is therefore limited to the interval from 0 to 0.5 Hz or from 0 to 4 Hz. These rates are appropriate to the study of fluctuations due to the sea because the dominant wave periods are generally greater than 5 seconds (i.e. 0.2 Hz).

Lastly, the statistical variability of the fluctuations was reduced during processing by incoherent averaging of four consecutive spectra.

3.2.1.2 Incoherent power determination by the RICE distribution

Assuming that the fluctuations follow a RICE distribution, the mean value of the resultant signal amplitude E_t is expressed on the basis of the standard deviation σ of the random vector and the ratio m^2 of the power P_d of deterministic signal to the random signal power P_a [2]:

$$\frac{E_t}{\sigma} = \left(\frac{\pi}{2}\right)^{1/2} \left[(1 + m^2)\, I_0\left(\frac{m^2}{2}\right) + m^2\, I_1\left(\frac{m^2}{2}\right)\right] \exp\left(-\frac{m^2}{2}\right) \qquad (2)$$

where I_0 (.) and I_1 (.) are zero - order and first - order modified Bessel functions of the first kind.

By expressing the mean power E_t^2 of the resultant signal, which is assumed to be constant, as a function of m^2:

$$\bar{E}_t^2 = P_a + P_d = 2\sigma^2 (1 + m^2) \qquad (3)$$

its standard deviation e_t becomes:

$$\frac{e_t}{\sigma} = \left[2(1 + m^2) - \left(\frac{\bar{E}_t}{\sigma}\right)^2\right]^{1/2} \qquad (4)$$

By relating expressions (2) and (4), e_t/E_t is expressed as a function of m^2 alone.

The experimental approach consists therefore in calculating the ratio of the standard deviation of the received signal to its mean signal value. This makes it possible to arrive at the corresponding m^2 value using expressions (2) and (4).

3.2.2 Experimental results

3.2.2.1 Statistical analysis

Fluctuations were analysed over periods in which the signal variations seem to be substantial, i.e. over the minima with a calm sea and also with a rough sea. The analysis was represented as four figures Figures 3.6 and 3.7 for each period studied:

- the time plot;
- the spectral density of the signal;
- the signal level distribution;
- the standardized curve for the signal level cumulative distribution.

A series of dotted curves were plotted in the Figures 3.6 and 3.7. On the assumption that the fluctuations follow a RICE distribution, it shows the power fraction F transmitted by the random vector over the total power.

$$F = \frac{P_a}{P_t} = \frac{P_a}{P_a + P_d} = \frac{1}{1 + m^2} \qquad (5)$$

The line of slope -10 dB per decade included in this network corresponds to the RAYLEIGH distribution.

The analyses as a whole, summarised in Table 3.2, are in accordance with the theoretical study.

Where the sea is calm and without swell, the signal fluctuations studied at the minima tend towards a RAYLEIGH distribution. The 9th November is the clearest example of this (Fig. 3.6). The wide range variation in signal levels (about 30 dB) is noteworthy.

Date	Time	H 1/3	Wind Speed	Mean Level	m^2	Calculated F	Graphically Determined F
09.11.84	1122 hrs	0.6 m	2.5 m/s	- 46.6 dBm	0.92	0.520	1 < F < 0.5
11.10.84	2338 hrs	0.4 m	2 m/s	- 48.2 dBm	2.14	0.318	0.2 < F < 0.3
31.10.84	2342 hrs	0.7 m	4 m/s	- 43.8 dBm	4.95	0.168	F = 0.3
10.12.84	1528 hrs	0.5 m	3 m/s	- 42.6 dBm	4.62	0.178	0.2 < F < 0.15
10.12.84	1840 hrs	0.5 m	3 m/s	- 42.3 dBm	5.40	0.156	0.15 < F < 0.125
27.11.84	2128 hrs	2 m	10 m/s	- 38.7 dBm	33	0.02	F = 0.025

Table 3.2

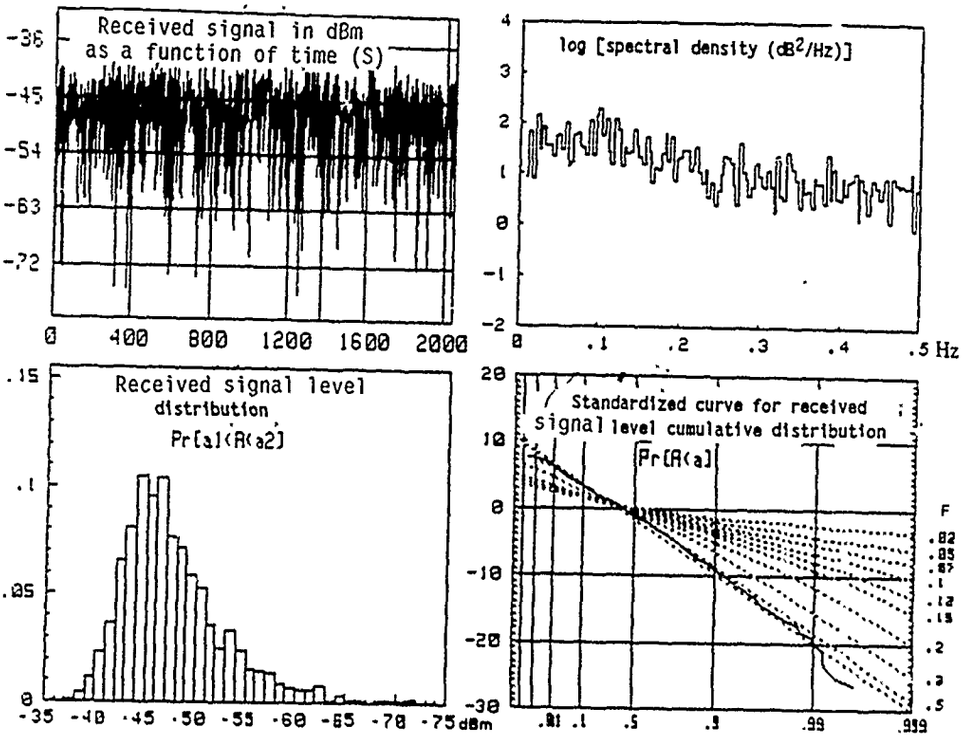

Transmission frequency: 36 GHz -- Sampling at 1 Hz
9 / 11 / 84 at 11 H 22

Figure 3.6: Study of fluctuations over a received signal
minimum: calm sea (H1/3 = 0.4 m)

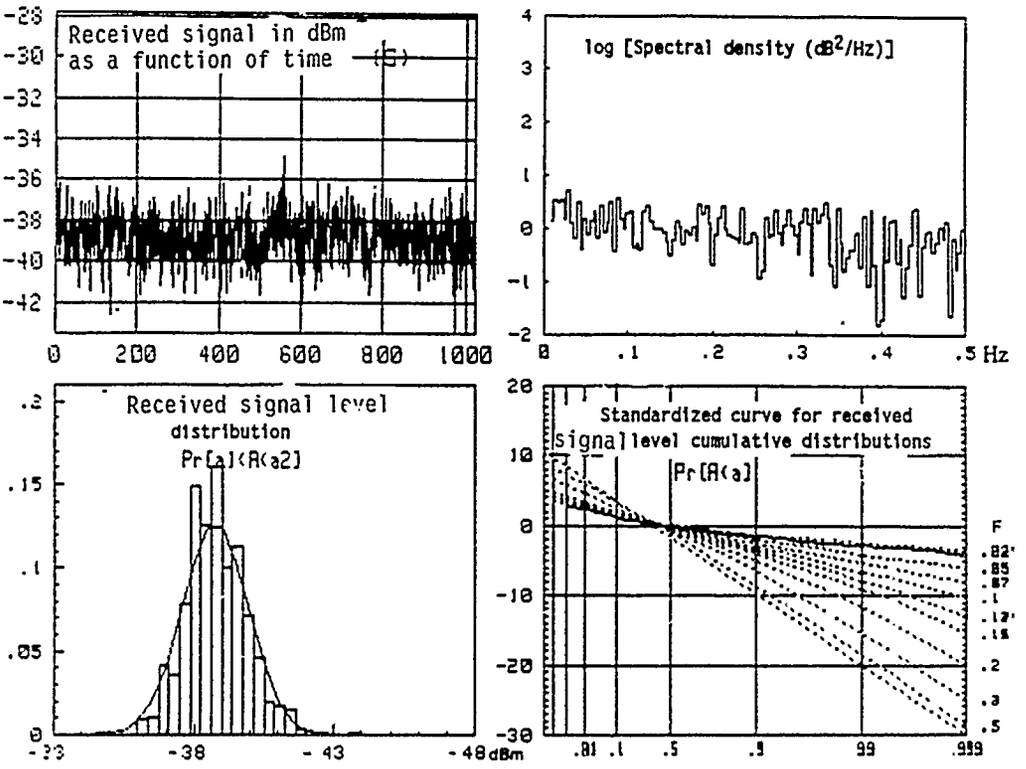

Transmission frequency: 36 GHz -- Sampling at 1 Hz
27/11/84 at 21 H 28

Figure 3.7: Study of fluctuations with a rough sea
($H_{1/3} \simeq 3$ m)

When the sea is rough the fluctuations are of Gaussian type (Figure 3.7). The power transmitted by the diffuse vector is then low with respect to that transmitted by the deterministic signal (F = 0.02).

3.2.2.2 Spectral analysis

(a) General results obtained during the first measurement campaign

The autumn-winter 1984-1985 campaign revealed a certain number of points linking sea state to signal spectrum:

- When the sea is calm (H1/3 < 1 m), spectral analyses show one or more lines around 0.1 Hz, the frequency associated with the swell movement.
- When the sea is rough (H1/3 > 2 m) the distribution is uniform over the entire field of study. There is no clearly distinguished line. The signal shows a frequency spectrum close to that for white noise (Figure 3.9 b).
- By varying the transmission frequency it can be shown that the spectral density peaks are approximately at the same frequency. They are particularly marked when the transmission frequency is low: when the wavelength decreases the sea becomes rougher and the diffusion component increases (Figure 3.8 a and b).

Lastly, the harmonic frequencies of the principal sea movement were revealed up to the second order (Figure 3.9 a).

Moreover, it became apparent during this experiment that there was disagreement between the significant wave period (TH1/3) recorded by the buoy and the frequencies corresponding to the signal spectra peaks.

The buoy put down in the vicinity of the reflection area in fact recorded a significant wave period close to 5 s. There was apparently a factor close to 2 between the principal periodicity of the signal and the "visual" periodicity of the sea supplied by the buoy.

(b) Joint analysis of hydrodynamic and signal spectra

This disagreement was removed during the August 1986 measurement campaign by successive measurements of signal level at 36 GHz and of instantaneous sea level height, giving access over a short period (about 20 minutes) to the hydrodynamic and signal spectral densities.

Although this type of measurement was carried out only for a few days, a wide variation in the sea state (from 1 to 4 on the Douglas scale) and in its aspect was recorded.

- Calm sea without swell

Following a day of light wind, the sea on the morning of 21st August showed a wide spectrum centred on 0.4 Hz. The significant wave height was 0.26 m (Figure 3.10 a). The signal spectrum was flat, with no dominant line (Figure 3.10 b).

- Calm sea with swell

A periodic movement of the sea of frequency close to 0.1 Hz became apparent during the afternoon. It corresponds to the swell movement from the ocean (Figure 3.11 a).

The received signal level spectral density also reveals a peak at the same frequency (Figure 3.11 b).

However, the harmonics of the principal movement are insufficient in power to stand out from the high-frequency spectrum originating in sea movements raised by the wind or in atmospheric turbulence.

Lastly, it is noted on referring to the hydrodynamic spectrum that the period TH1/3 does not correspond to a dominant movement of the surface, and consequently has no significance in relation to the received signal.

- Sea raised by the wind

A south-west wind, force 6 on the Beaufort scale, raised the sea in a few hours at the end of August 1986. The hydrodynamic spectra obtained during this period were compared with the PIERSON-MOSKOWITZ spectrum (Figures 3.12 a and 3.13 a). A fairly good match is apparent, particularly as regards the peak frequency and the steep front at low frequencies.

The signal spectrum has something in common with a noise spectrum with no dominant line, a form already recognised during the 1984-1985 campaign (Figure 3.7). So the hydrodynamic spectrum does not correspond to the signal spectrum.

- Superposition of swell and sea raised by wind

Figure 3.14 showing the hydrodynamic spectrum reveals that the sea movement is the result of swell (peak at $\simeq 0.1$ Hz) and a wind-induced sea movement (wide peak around 0.4 Hz).

It should be noted that TH1/3 = 3.81 s in no way represents the periodicity of the surface.

Periodicity at 0.1 Hz is found again in the received signal (Figure 3.14 b).

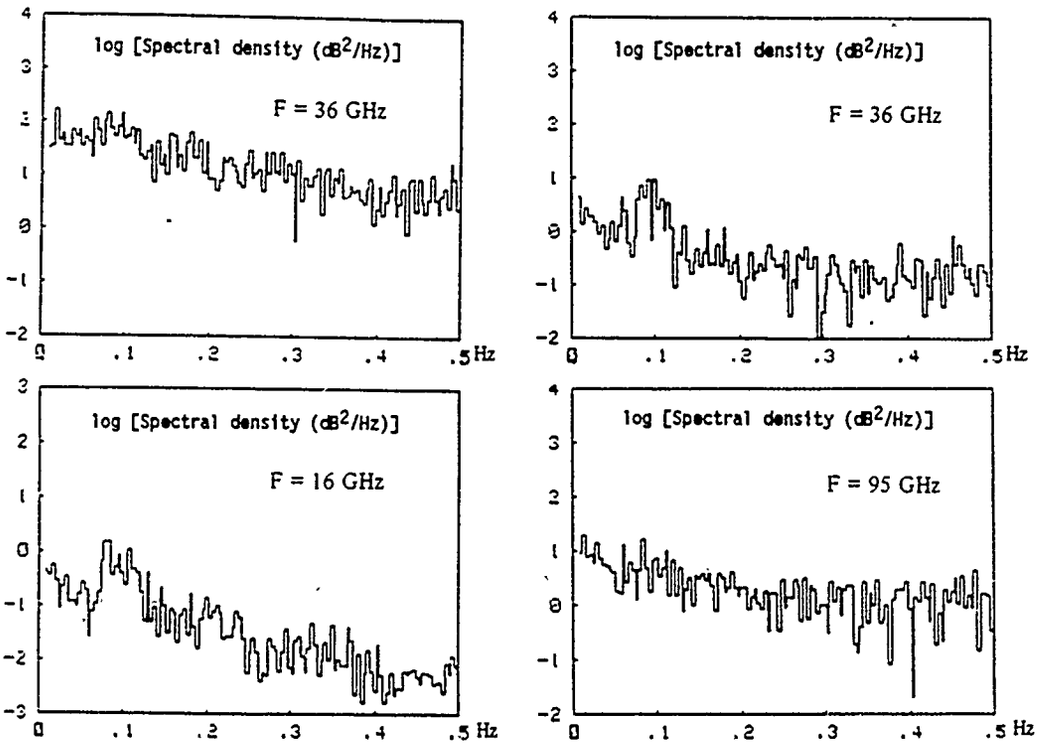

9 - 11 - 1984 at 11h15

H1/3 = 0.6 m
Wind speed (*) = 1.8 m/s

11 - 12 - 1984 at 13 h

H1/3 = 0.4 m
Wind speed = 1.4 m/s

Figure 3.8 a & b: Spectral analyses at 16, 36 & 95 GHz

(*) On the buoy.

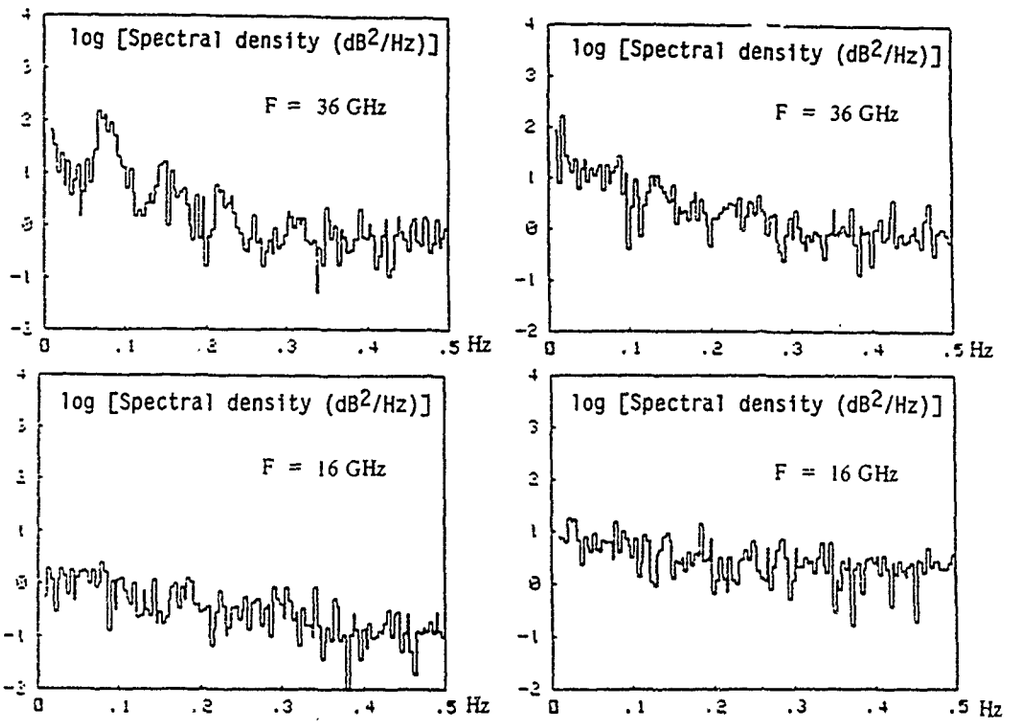

7 - 01 - 1985 at 19h15

Calm sea
Wind speed (**) ≃ 3 m/s

13 - 11 - 1985 at 22h30

H1/3 = 2.3 m
Wind speed (*) = 9 m/s

Figure 3.9 a & b: Spectral analyses at 16 and 36 GHz

(*) On the buoy
(**) At the receiver site

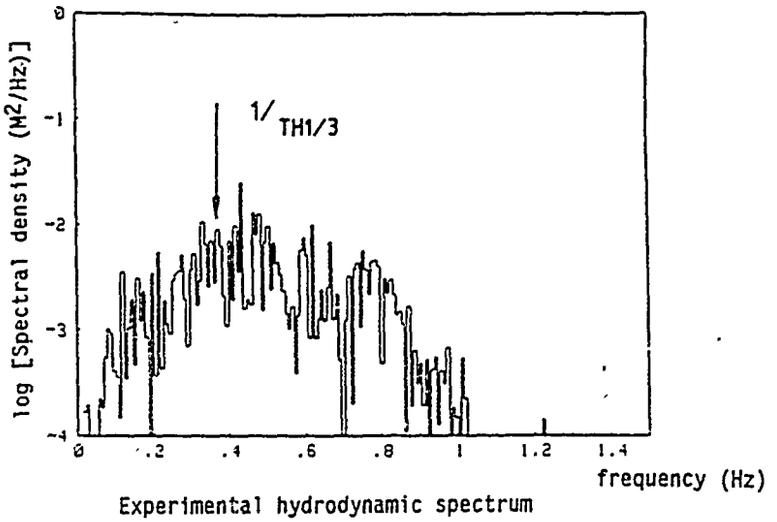

Experimental hydrodynamic spectrum

Mean square height = .08 M
21 / 8 / 86 at 9 h 26 mn Exp. no M01

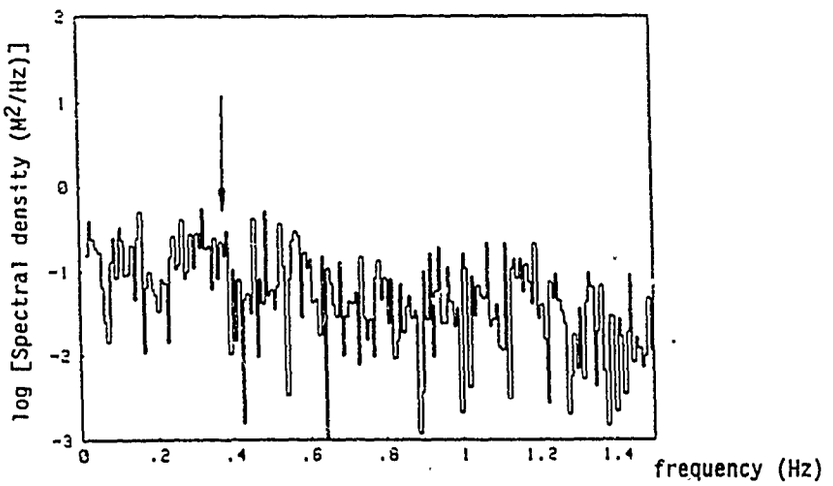

Spectral density at received signal level at 36 GHz
21 / 8 / 86 at 9 h 5 mn Exp. no SN44

Figure 3.10: Spectral analysis, calm sea without swell
(H1/3 = 0.26 m; TH1/3 = 2.67 s)

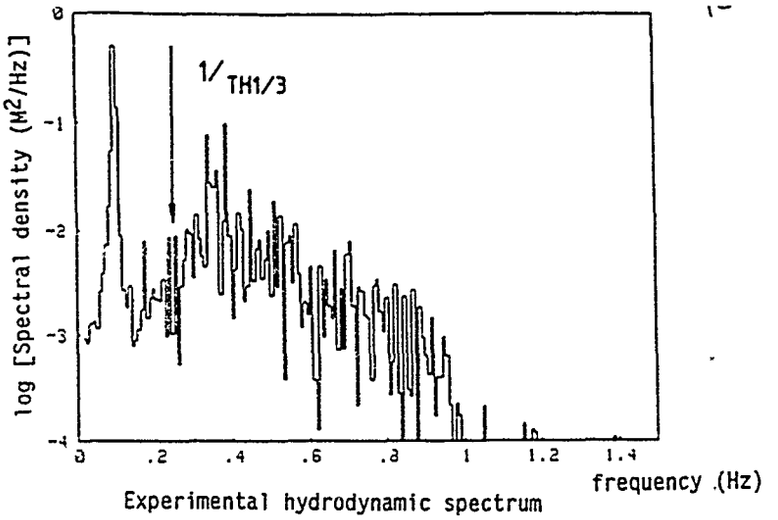

Experimental hydrodynamic spectrum

Mean square height = .12 M
21 / 8 / 86 at 18 h 4 mn Exp. no BN03

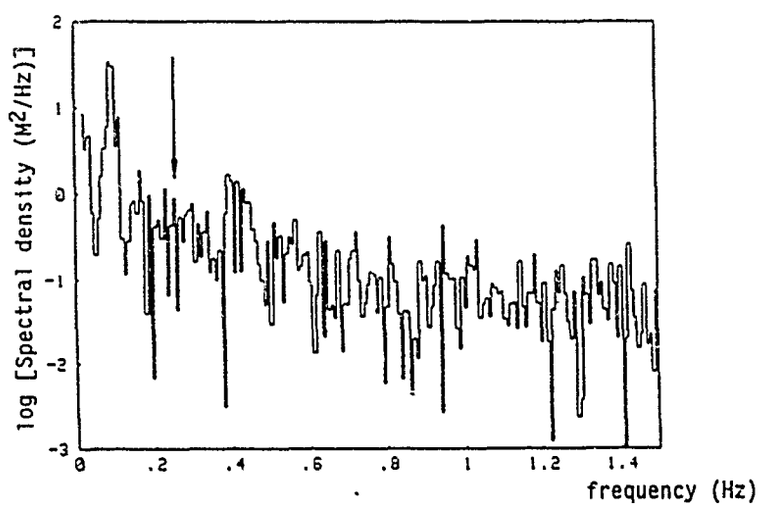

Spectral density at received signal level at 36 GHz
21 / 8 / 86 at 17 h 36 mn Exp. no S46

Figure 3.11: Spectral analysis, calm sea with swell
(H1/3 = 0.35 m; TH1/3 = 4.15 s)

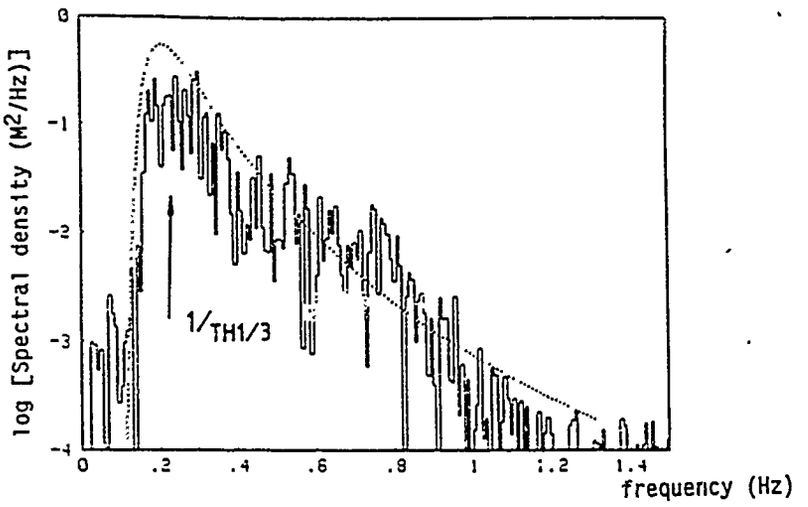

Experimental spectrum (-) and PIERSON-MOSKOWITZ spectrum (- -)
Mean square height = .29 M
25 / 8 / 86 at 15 h 36 mn Exp. no M11

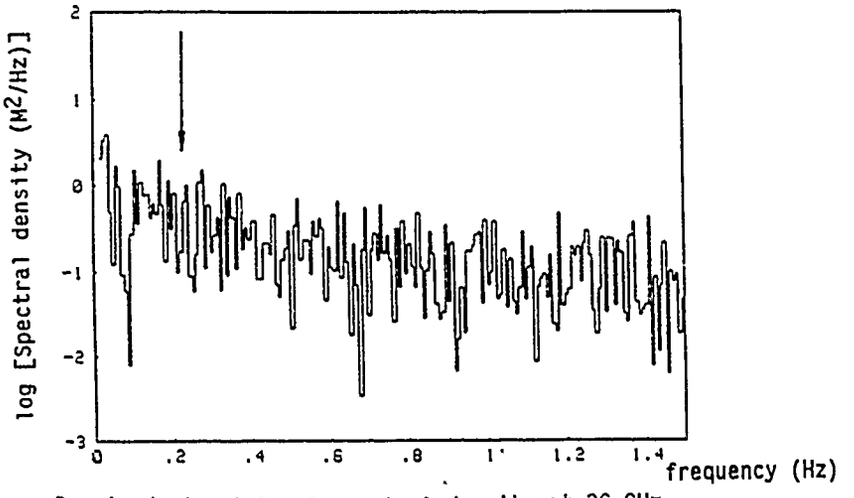

Received signal level spectral density at 36 GHz
25 / 8 / 86 at 15 h 36 mn Exp. no SN56

Figure 3.12: Spectral analysis in the presence of sea raised by wind
(Wind speed = 12 m/s; H1/3 = 1.04 m; TH1/3 = 4.55 s)

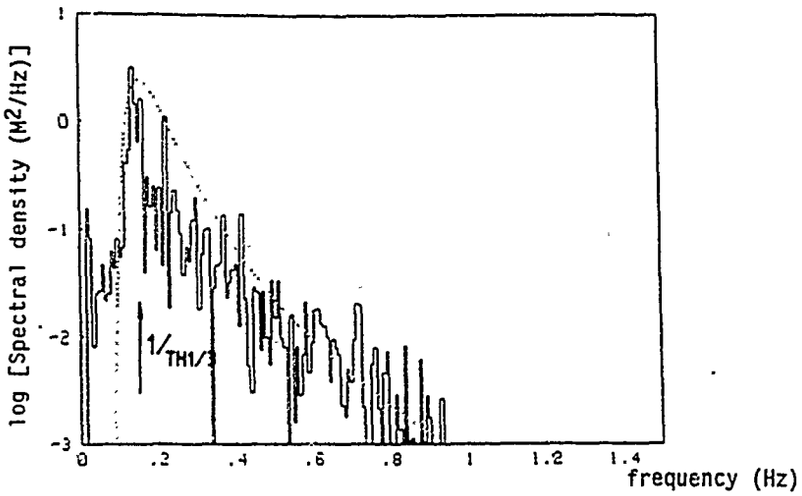

Experimental spectrum (-) and PIERSON-MOSKOWITZ spectrum (...)
Mean Square height = .51 m
25 / 8 / 86 at 22 h 29 mn Exp. no BN13

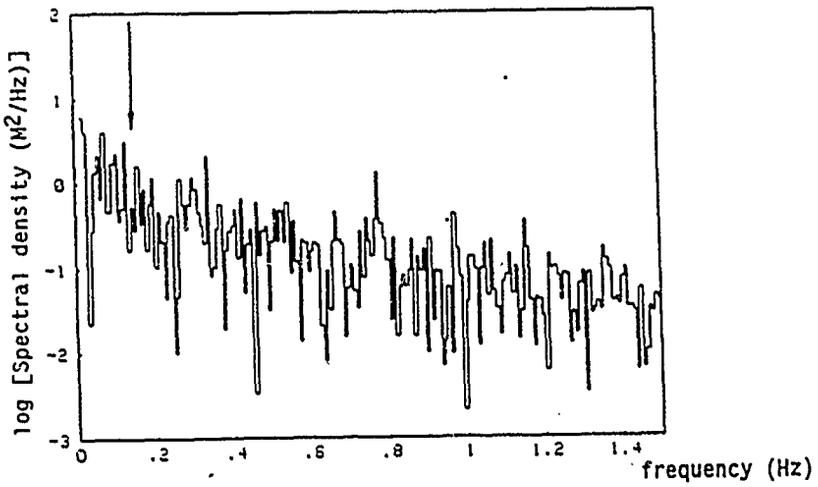

Received signal level spectral density at 36 GHz
25 / 8 / 86 at 22 h 39 mn Exp. no SN58

Figure 3.13: Spectral analysis in the presence of sea raised by wind
(Wind speed = 14 m/s; H1/3 = 1.75 m; TH1/3 = 6.5 s)

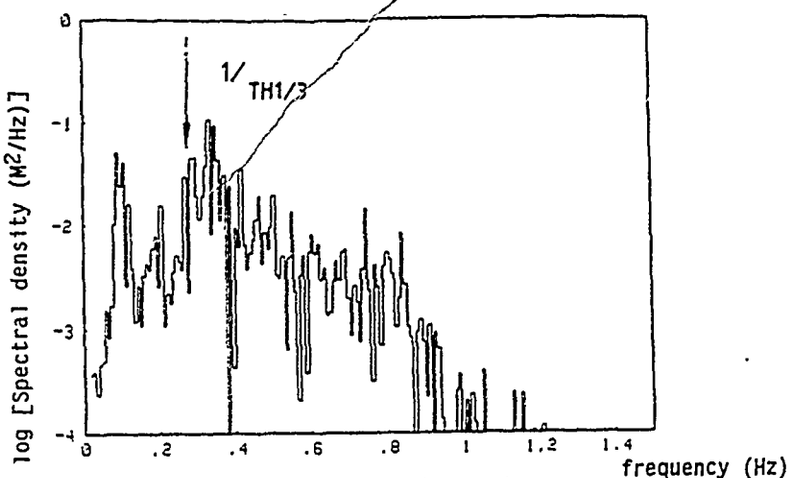

Experimental hydrodynamic spectrum

Mean square height = .15 M
21 / 8 / 86 at 19 h 13 mn Exp. no M04

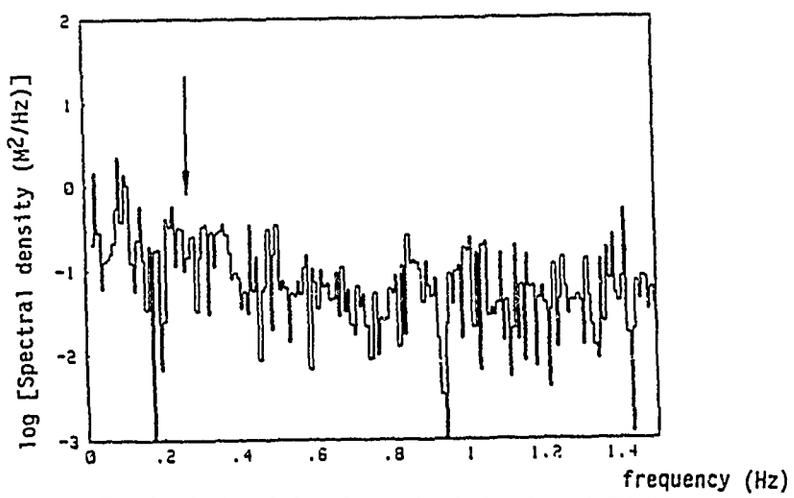

Received signal level spectral density at 36 GHz
21 / 8 / 86 at 19 h 24 mn Exp. no SN48B

Figure 3.14: Superposition of swell and sea raised by wind
(H1/3 = 0.5 m; TH1/3 = 3.8 s)

On the other hand, wave movements towards the higher frequencies do not seem to induce periodicity in the signal received: short-period waves originate when the wind rises. Their wavelengths are distinctly shorter than the swell wavelength. The waves deform the FRESNEL ellipses into a vast number of reflecting surfaces positioned almost at random. Consequently an averaging effect operates on the elementary signals received as a whole and eliminates wave periodicity.

In this experimental context the received signal level at 36 GHz seems to be more sensitive to low-frequency sea movements rather than to higher-frequency movements.

(c) Comments on received signal level periodicity

The signal level at reception is linked to the reflecting surface, corresponding approximately to the first FRESNEL zone. It will be remembered that this zone is an ellipse, greatly elongated in the direction of propagation (Chapter II, paragraph 2.3.3.3). The form which the sea takes on this surface therefore determines the form of the received signals. Several patterns may occur.

Calm sea without swell or sea raised by the wind

In this case the incoherent component is the sum of a large number of perfectly random elementary amplitude and phase signals (diffusers). BEARD and KATZ [1] state that the number of diffusers in the first illuminated FRESNEL zones must be at least five in order that the reflected signal can be considered as random.

This rule is verified in the context of the links studied by the disordered appearance of the surface and the length of the FRESNEL ellipses ($\approx$ 1.2 km at 36 GHz) with respect to the wavelength of the waves (at a maximum of 70 m).

Swell

When a swell is present, the incoherent component loses its totally disordered aspect, the most favourable case being that in which the direction of swell is perpendicular to the direction of propagation. The primary FRESNEL zones, with secondary axes much shorter than the wavelength of the waves, then include only a limited number of diffusers operating at the frequency of the swell and reflecting the incident wave in phase.

As regards the 36 GHz link, the angle between the direction of the swell and the principal axis of the ellipses was about 45°. The number of diffusers in this zone is presumed to be low, since the wavelength of the swell is at least 100 m or so. However, it cannot be calculated because of the rough aspect of the sea, which alters the dimensions of the reflecting surface.

NOTE: The fluctuations analysis time is a parameter to be treated with care. In the case of the link configurations studied, in which the reflected signal shows the periodicity of the swell, the statistical properties of the signals must nevertheless be invariable in time (the steady-state hypothesis). The analysis periods should therefore be greater in duration than the period of the principal sea movement (generally less than 10 s) in order to arrive at the signal level distributions.

3.3 EXPERIMENTAL STUDY OF LONG-TERM FLUCTUATIONS

Utilisation of the experimental data is based upon the model described in detail previously in Chapter II, paragraph 3.5.3. It is used to determine the coefficient of forward reflection and the interference figures are reconstituted in time on the basis of tide data and sea roughness data supplied by the buoy.

3.3.1 Coherent forward reflection coefficient

3.3.1.1 Measurement principle

This value is calculated on the basis of the extreme received signal levels. These are formulated as follows:

- for the minimum signal level:

$$E_m\,(dB) = 20 \log (F_{dm} - \rho_{om}\,\rho_c\,D_m\,F_{im}) \qquad (6)$$

- for the maximum signal level:

$$E_M\,(dB) = 20 \log (F_{dM} + \rho_{oM}\,\rho_c\,D_M\,F_{iM}) \qquad (7)$$

They assume that the coherent forward reflection coefficient ρ_c is invariate between two successive extrema. This is true in the case of settled sea states in which the meteorological and oceanographic parameters are stable in time.

for ρ_c. Solving the previous two equations leads immediately to the expression

$$\rho_c = \frac{F_{dm}\ 10^{A/20} - F_{dM}}{D_m\ F_{im}\ \rho_{om}\ 10^{A/20} + D_M\ F_{iM}\ \rho_{oM}} \qquad (8)$$

where $A = E_M - E_m > 0$ is the difference in attenuation between two successive extrema.

Two procedures have been set up to arrive at this value by experiment.

The first uses the tide. According to its amplitude, the period essential for determination of a measurement point is between 20 minutes and 1 hour.

Since environmental characteristics may change over long periods, a hoist was used to carry the reception antenna: the interference figures are then reproduced in a much shorter time (a few minutes).

3.3.1.2 Measurement of coherent forward reflection on the basis of variation in receiver height

The received signal level was subject to rapid fluctuations, due principally to the sea, the maximum principal period of which was of the order of 10 seconds.

The received signal level was averaged over a time substantially greater than the wave principal period, in order to reduce the effect of the corresponding incoherent term upon the extreme values, without making any a priori assumptions on its probability distribution.

With this in view, the hoist height was varied in stages during measurement. Fixing its duration at 30 mn and limiting errors of phase, the duration of a stage was 30 seconds and the height between two stages was 10 cm.

At 36 GHz, lowering the reception antenna 5 m causes the received signal level to pass through 5 minima. The transition from one extremum to another calls for a variation in the mean level of the sea of about 40 cm (Chapter II, paragraph 2.3.5.3).

Figure 3.15 shows a raising of the hoist when the sea is calm. The solid line shows the signal level averaged over each stage, whereas the measurements at 1 Hz appear as points.

Eleven measurements of this type were carried out over three consecutive days, yielding the coherent forward reflection coefficient (Figure 3.16):

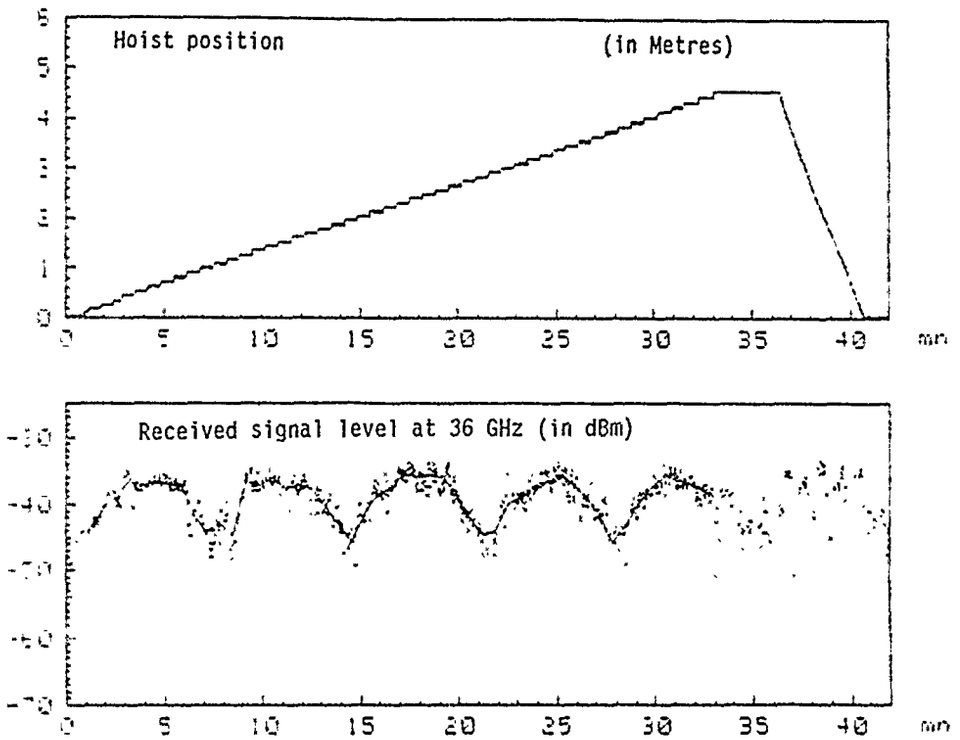

Figure 3.15: Measurement with hoist: calm sea
(H1/3 = 0.5 m)

- on the morning of 17th October the sea was calm (H1/3 = 0.6 m). The interference figures, of amplitude 10 dB, are clearly marked. The westerly wind then strengthened in the course of the day and night;

- the next day its speed reached more than 13 m/s. The sea was very rough (H1/3 > 2.5 m).

The amplitude of the interference figures, which was under 2 dB, decreased greatly.

- On the 19th the wind was a strong breeze and the sea was a little less rough (H1/3 = 1.9 m) (Figure 3.17).

3.3.1.3 Measurement of coherent forward reflection with fixed antennas

To supplement measurements made with the hoist, ρ_c was also determined using data acquired when the antennas were fixed.

The selected periods show interference figures due solely to the tide phenomenon. Then the meteorological measurements revealed:

- a low air temperature (less than 15°C);

- high relative humidity (close to 100%);

- the presence of wind, mixing up the atmosphere.

The received signal levels were averaged over two minutes in order to get rid of scintillations due to reflection on the sea. This period, which is long relative to the dominant wave period, ensures that the error on the position of the minima is acceptable. The maximum error on the indirect signal phase relative to the direct signal is less than 15° in the most unfavourable circumstances (tides of great amplitude).

Moreover, the data were smoothed by moving average over 10 minutes, to filter out variations due to wave propagation by groups and variations caused by atmospheric turbulence.

As before, the coherent forward reflection coefficient was determined over some 10 periods corresponding to degrees of roughness between 0.06 and 0.46 (Figure 3.18).

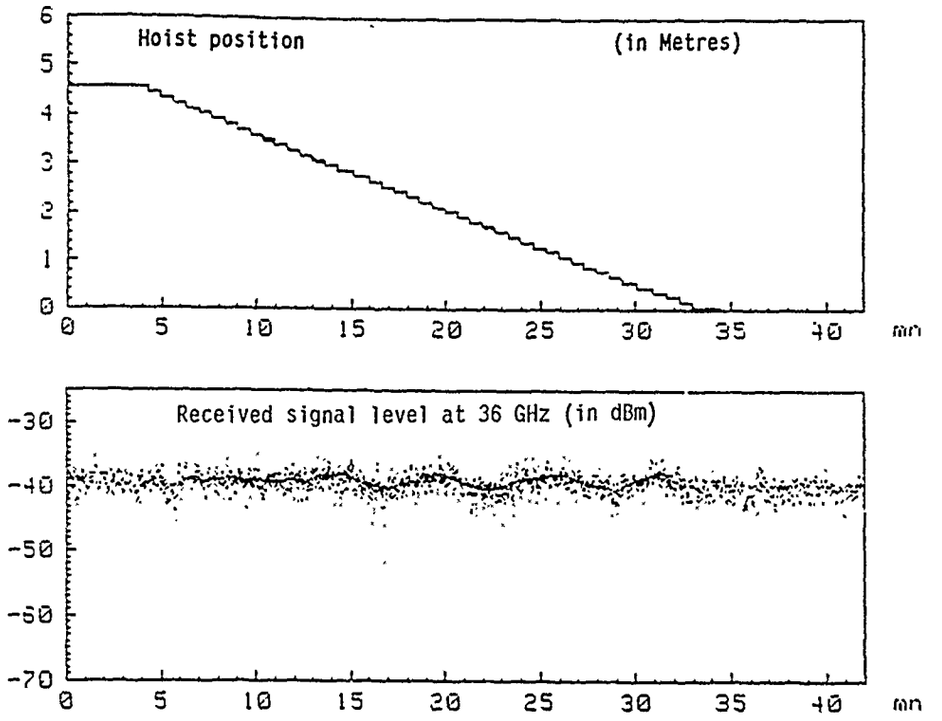

Figure 3.17: Measurement with hoist: rough sea
(H1/3 = 1.9 m)

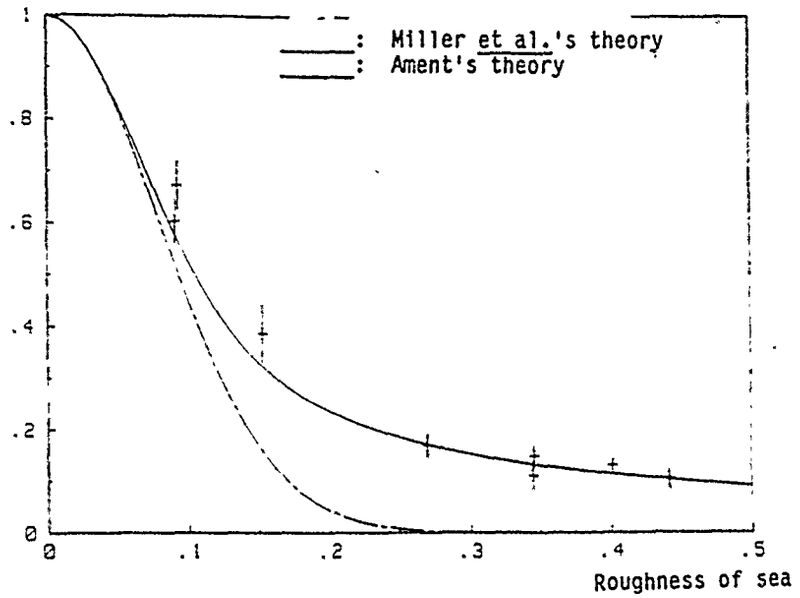

Figure 3.16: Coherent foward reflection coefficient
(Measurements with hoist)

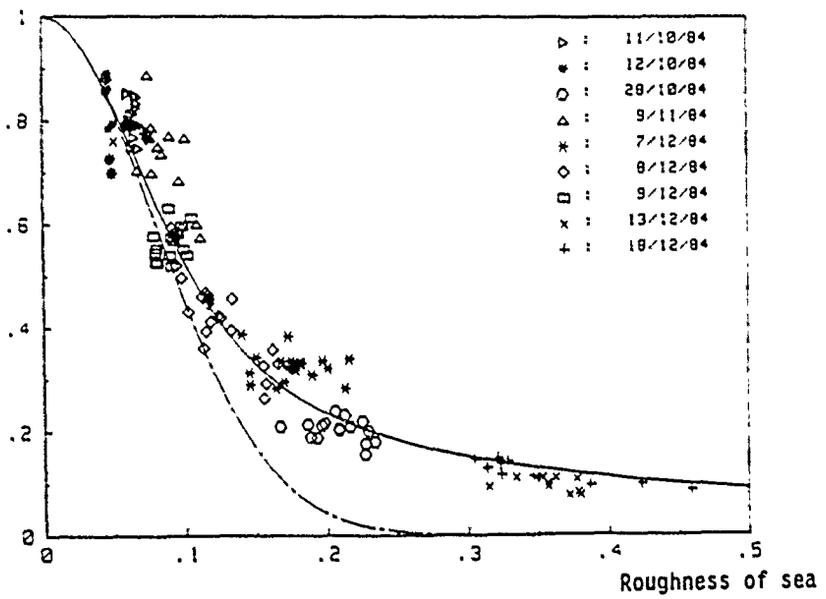

Figure 3.18: Coherent forward reflection coefficient
(Measurements with fixed antennas)

3.3.1.4 Calculation error relating to ρ_c

Determination of the coherent forward reflection coefficient ρ_c on the basis of propagation data and theoretical calculation on the basis of environmental data are subject to measurement errors which should be borne in mind. Measurement errors relate to:

- wave height supplied by the buoy;
- link geometry.

Differentiation of the expression of MILLER et al. in terms of the two previous parameters leads to the relative error of ρ_c:

$$\frac{\Delta \rho_c}{\rho_c} = 4x^2 \cdot \left[\frac{I_1(2x^2)}{I_0(2x^2)} - 1\right] \left[\frac{\Delta H1/3}{H1/3} + \frac{\Delta\varphi}{\varphi}\right] \qquad (9)$$

where $$x = \frac{\pi H1/3 \sin\varphi}{2\lambda_1} \qquad (10)$$

and $\varphi \approx \sin\varphi$ is less than 0.5°.

The relative error of ρ_c (Figure 3.19) reaches a value close to 17% in the case of an error in wave measurement of 10 cm (ρ_c is then about 0.6).

The processing errors lie in the amplitude Δ between the two successive extrema. In fact variations in atmospheric uniformity (possibly light rain or fog) and large variations in sea level height may lead to an error Δ A on this value.

Expression (8) was derived as a function of A to assess this error:

$$\frac{\Delta \rho_c}{\rho_c} = 0.230 \cdot \frac{10^{A/20}}{10^{A/10} - 1} \cdot \Delta A \qquad (11)$$

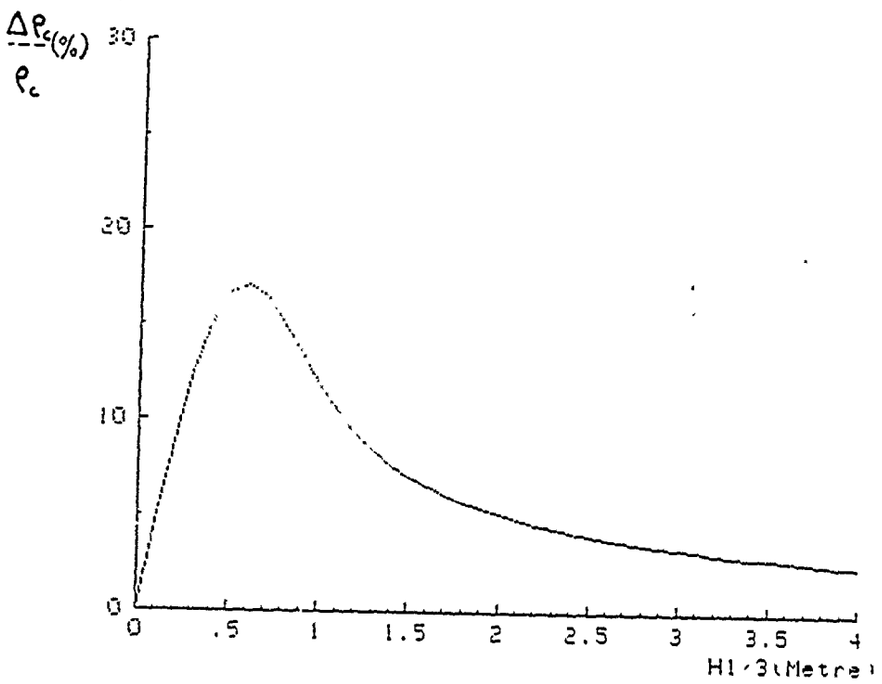

Figure 3.19: Relative error curve for the coherent forward reflection coefficient

(Δ H1/3 = 0.1 m)

Its plot (Figure 3.20) in the form of a graph parametered in A and Δ A shows an error of ρ_c decreasing with high amplitudes. The uncertainty Δ A is not easy to evaluate: it was nevertheless possible to draw up Table 3.3 by analysing the differences in amplitude between successive extrema for identical environmental situations:

A	Δ A	ρ_c	$\Delta\rho_c$	$\frac{\Delta\rho_c}{\rho_c}$
2	0.5	0.14	0.05	35%
5	1.5	0.35	0.11	30%
10	2.5	0.65	0.13	20%
15	3.5	0.87	0.12	15%

Table 3.3

Accumulation of the two types of error gives dispersion values compatible with those observed.

In the final analysis, this error may seem substantial. Accurate calculation of the coherent forward reflection coefficient by the method used is not easy in the context of the present experiments: a shorter link would have been less disrupted by atmospheric propagation.

3.3.1.5 Comments

From the experimental results using the hoist and also fixed antennas (Figures 3.16 and 3.18) it follows that the theory of MILLER and al. can be used in a satisfactory way for the estimation of the coherent reflection coefficient over the entire roughness interval, taken into account the measurement errors. Unlike AMENT's expression, which is valid only for roughnesses below 0.1, the MILLER and al. formulation is well suited for large roughness values.

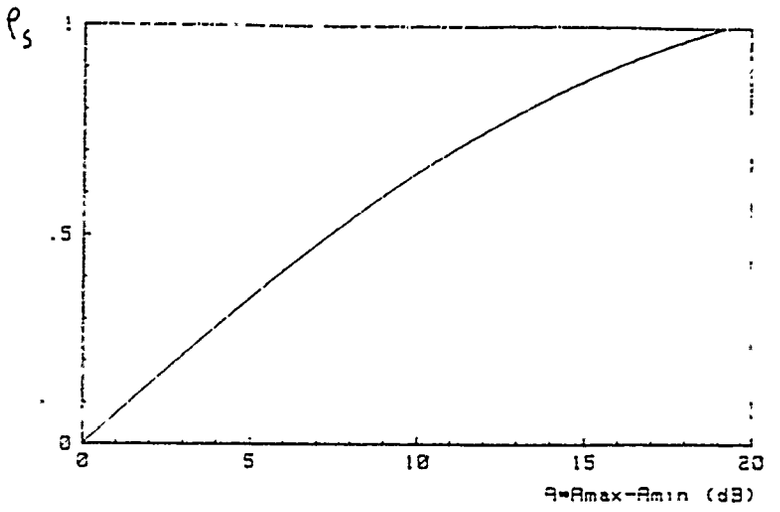

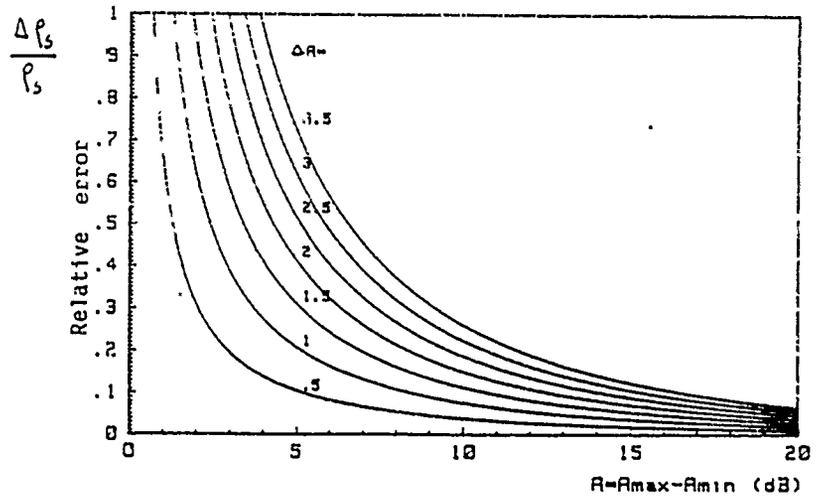

Figure 3.20: Coherent forward reflection coefficient ρ_s and relative error $\frac{\rho_s}{\rho}$ as a function of amplitude A of interference figures

Introduction of a sinusoidal form into the expression for instantaneous sea level height as used by MILLER and al. therefore permits better simulation of the phenomenon.

3.3.2 Received field calculation on the basis of the data acquired

A calculation programme based on the equations in Chapter II, paragraph 3.5 has been developed in order to plot long-term fluctuations in time. Its input parameters are broken down into two groups:

* Parameters which are fixed or presumed to be fixed:
  - transmission frequency;
  - link geometry;
  - the refractive index gradient.
* Parameters which are variable in time:
  - the mean sea level height;
  - sea roughness measured by the buoy.

In general, this type of processing reconstructs the interference figures approximately only, because of misreading of the atmospheric structure and uncertainties in measurement regarding the mean height of the sea. The latter value was available at any time only at the main port of GROIX, about 9 km from the reflection zone. In addition, substantial tide effects in this region caused time shifts in the mean height of the sea between the point of measurement and the reflection zone.

A different calculation process using experimental propagation data was set up in order to remedy this lack of data.

3.3.2.1 Received field level reconstitution

This reconstitution method assumes that the periodic variations recorded at reception are due solely to the tide. In addition we satisfy ourselves by considering the weather conditions that we are not in a situation which might give rise to substantial variations in the refractive index of the air.

The received signal is extreme at certain sea level positions: a FRESNEL ellipsoid is then tangential to the surface. When the order of this ellipsoid is even (odd) the received signal is at a minimum (maximum). These sea height values are shown in Table 3.4.

Sea height (*)	Order of ellipsoid (**)
0.27	28 (m)
0.63	27 (M)
0.98	26 (m)
1.34	25 (M)
1.72	24 (m)
2.08	23 (M)
2.47	22 (m)
2.85	21 (M)
3.24	20 (m)
3.64	19 (M)
4.04	18 (m)
4.45	17 (M)
4.88	16 (m)

Table No. 3.4

(*) Relative to level 0 on naval charts
(**) m: minimum received signal level
M: maximum received signal level

The principle of this method involves identifying the points in time at which the FRESNEL ellipsoids are tangential to the surface on the basis of the received signal, and linking the corresponding sea height to them.

Instantaneous variations in the sea are then interpolated on the basis of the extremal positions and values. Lastly, a smoothing of the curve obtained eliminates discontinuities of slope.

A knowledge of the tide pattern and of variations in the roughness of the sea (giving access to the coherent forward reflection coefficient) makes it possible to reconstitute the received signal level profile over all the stable periods recorded (no rain and no abnormal propagation phenomenon). Figure 3.21 provides an illustration of this treatment.

NOTE: The following method is used to eliminate the ambiguity regarding the sea level height at the extrema: the extreme closest to the time of low or high tide is identified, and the sea level height supplied by Table 3.4 closest to that given in the measured tide table is linked to it.

3.3.3 Statistical study of long-term fluctuations at a frequency of 36 GHz

A statistical study relating to the signal levels, both measured (averaged over two minutes and computed, was carried out over 89 hours of calm sea ($H1/3 < 1.3$ m) and over 28 hours of slightly rough and rough sea ($H1/3 > 1.3$ m) in order to validate the above reconstitution method. The surface roughness has also been studied statistically.

Analysis of the curves obtained (Figure 3.22 a and b) calls for the following observations:

- the difference in behaviour under the two surface state conditions is remarkable: although the fluctuation amplitude reaches 18 dB with a smooth and slightly rough sea (roughness $g \leqslant 0.2$), it decreases to 4 dB with a rough sea ($g > 0.2$);

- the received signal level cumulative probability curves intercept at a point corresponding to the mean value (50%). This value remains the same whatever the sea state;

- the curves relating to the measured signal and the computed signal lie close to each other. The difference between them does not exceed 1 dB for a given percentage of time: the method of received signal calculation on the basis of reconstituted tide and measured wave heights is satisfactory for periods in which atmospheric conditions are constant.

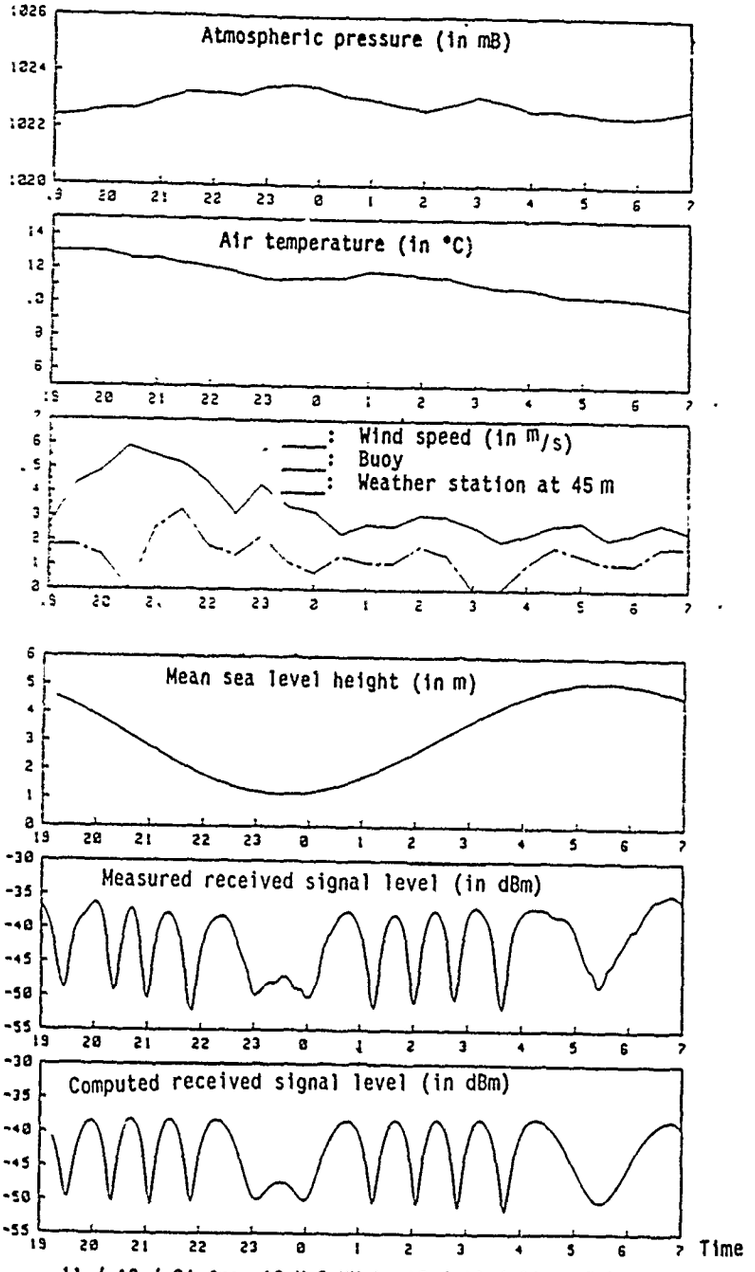

11 / 10 / 84 from 19 H 0 MN to 12 / 10 / 84 at 7 H 0 MN
Frequency = 36 GHz K = 1.33

Figure 3.21: Reconstitution of interference figures

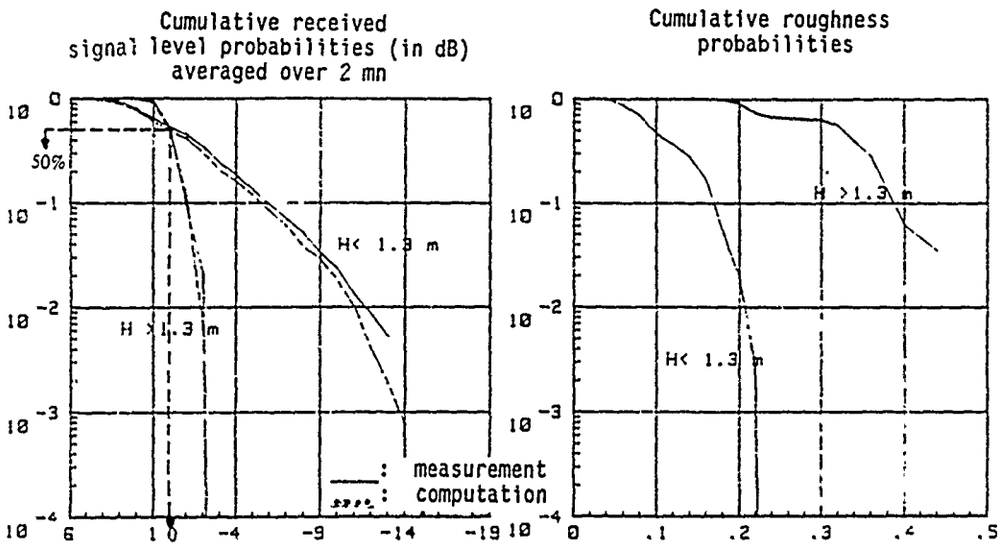

Figure 3.22: Coherent reflection at 36 GHz as a function of sea surface roughness
Experiment at LORIENT 1984-85

CHAPTER IV

STUDY OF DISTURBANCES LINKED WITH MILLIMETRE WAVE PROPAGATION IN A MARITIME ATMOSPHERE

4.1 INTRODUCTION

Disturbances affecting propagation in the atmosphere have not been considered up to now. Solely taking into account the standard atmosphere with a constant index gradient has had the effect of modifying the curvature of the earth in developing the model based on coherent reflection.

In fact, as is apparent from qualitative analysis of signals received (Chapter I, paragraph 1.3.3), a number of atmospheric phenomena may disturb the link to a greater or lesser extent. These are essentially:

- rain;
- variations in the refractive index of the air.

The effect of other hydrometeors (fog, snow) on propagation will also be dealt with.

4.2 ATTENUATION DUE TO MOLECULAR ABSORPTION

The presence of gases in the atmosphere (in particular oxygen and water vapour) causes part of the energy transmitted in millimetre waves to be absorbed.

In order to limit these losses, the frequencies selected when systems are designed are usually those which correspond to the minimum absorption bands ("windows"). These bands are around 35 GHz and 95 GHz, where absorption due to gases is of the order of 0.1 dB/km and 0.5 dB/km respectively [53].

Molecular attenuation depends increasingly upon the water vapour content when we move towards the upper part of the spectrum. At 95 GHz, attentuations due respectively to water vapour and oxygen reach 0.5 dB/km and 0.03 dB/km. Molecular attenuation may vary substantially according to the meteorological conditions encountered [54].

4.3 ATTENUATION DUE TO RAIN

4.3.1 Theoretical calculation of attenuation due to rain in the millimetre wave region

The effects of rain upon centimetre and millimetre wave propagation are numerous: full calculation of linear attenuation caused by rain should take account of the following:

- The shape of the raindrops and their inclination relative to the wave plane:

  Water particles exceeding 3 mm in diameter take the form of flattened spheroids. They may be inclined 10°-20° to the vertical [55].

- Incident wave polarisation:

  Since the raindrops are flattened along the horizontal axis, incident wave attenuation will be larger for horizontal polarisation than for vertical polarisation [56]. In addition the wave undergoes depolarisation.

- Multiple diffusions:

  The wave is reflected from particle to particle before reaching the reception antenna: this leads to a loss of wave coherence. The multiple aspect of diffusion is negligible in the case of frequencies below 30 GHz [57].

In the following paragraphs, raindrops will be treated as spherical. This approximation is justified having regard to the following:

- uncertainty in determination of attenuation caused by rain (due principally to the presence of the double path);

- the type of rain generally recorded, the preciptation rate being rarely in excess of 15 mm/h.

4.3.1.1 Diffusion of an electromagnetic wave by a sphere: the MIE theory

The problem of electromagnetic wave diffusion by a conducting sphere was solved for the first time by MIE in 1908 [58]. This work was subsequently pursued by other authors such as STRATTON (1941) [59], VAN DER HULST (1957) [60], KERKER (1969) [61] and BORN and WOLF (1975) [62].

The problem can be solved in various ways.

The method developed by STRATTON and adopted by VAN DER HULST is based upon vector wave equations.

KERKER and BORN and WOLF contemplate this solution in another way. This involves introducing HERTZ electrical and magnetic potentials.

When attenuation by rain is studied, the point of observation is a long way from the particle. Simplified expressions for the electric and magnetic fields are then obtained. The wave is transverse electromagnetic, and the electric field is expressed by the following relationships:

$$\begin{cases} E_\theta = \dfrac{i \exp(-i k_2 r)}{k_2 r} \cos\phi \, S_2(\theta) \\ E_\phi = \dfrac{-i \exp(-i k_2 r)}{k_2 r} \sin\phi \, S_1(\theta) \end{cases} \tag{1}$$

with

$$\begin{cases} S_1(\theta) = \displaystyle\sum_{n=0}^{\infty} \frac{2n+1}{n(n+1)} \left\{ a_n \pi_n(\cos\theta) + b_n \tau_n(\cos\theta) \right\} \\ S_2(\theta) = \displaystyle\sum_{n=0}^{\infty} \frac{2n+1}{n(n+1)} \left\{ b_n \pi_n(\cos\theta) + a_n \tau_n(\cos\theta) \right\} \end{cases} \tag{2}$$

where $S_1(\theta)$ and $S_2(\theta)$ are functions of amplitude dependent upon the MIE coefficients a_n and b_n:

$$a_n = \frac{\psi_n'(\beta)\,\psi_n(\alpha) - m\,\psi_n(\beta)\,\psi_n'(\alpha)}{\psi_n'(\beta)\,h_n(\alpha) - m\,\psi_n(\beta)\,h_n'(\alpha)} \tag{3}$$

$$b_n = \frac{\psi_n'(\alpha)\,\psi_n(\beta) - m\,\psi_n(\alpha)\,\psi_n'(\beta)}{h_n'(\alpha)\,\psi_n(\beta) - m\,\psi_n'(\beta)\,h_n(\alpha)} \tag{4}$$

where

$$\beta = m_1 \frac{2\pi a}{\lambda_1} \qquad \alpha = m_2 \frac{2\pi a}{\lambda_1} \tag{5}$$

m_1 is the refractive index of the sphere material;

m_2 is the refractive index of the sphere's external environment;

$m = m_1/m_2$;

$\psi_n(.)$ is an n-order Ricatti-Bessel function;

$\psi_n'(.)$ is its derivative;

$h_n(.)$ is an n-order Hankel function;

$h_n'(.)$ is its derivative.

FORTRAN data-processing programming for the MIE coefficients is set out in reference [47].

4.3.1.2 Extinction and diffusion cross-sections

4.3.1.2.1 Definitions

(a) Definition of the extinction cross-section

The extinction cross-section of a particle is the ratio (in the direction of the incident wave) of the loss in total power due to the presence of the particle to the incident power density:

$$Q_e \ [m^2] = \frac{P_e \ [W]}{p_i \ [W/m^2]} \tag{6}$$

(b) Definition of the diffusion cross-section

The diffusion cross-section of a particle is the ratio of the total diffused power to the incident power density:

$$Q_s = \frac{P_s \ [W]}{p_i \ [W/m^2]} \tag{7}$$

(c) Definition of standardized effective cross-sections

This is the ratio of the cross-sections defined above to the effective geometric cross-section of the particle S:

$$Q_n = \frac{Q \ [m^2]}{S \ [m^2]} \tag{8}$$

These magnitudes are dimensionless.

For a spherical particle of radius a, $S = \pi a^2$.

(d) The albedo of a particle

The albedo of a particle is the ratio of the diffusion cross-section to the extinction cross-section:

$$\text{Albedo} = \frac{Q_s}{Q_e} \tag{9}$$

4.3.1.2.2 Expression of cross-sections as a function of the MIE coefficient

Calculation of the extinction and diffusion cross-sections leads to determining the power balance and applying the POYNTING theorem: during a time Δt the total energy loss localised in a volume V containing the sphere is equal to the POYNTING vector outgoing flux through the surface Σ which bounds this volume.

The calculated powers are then divided by the incident power density. Expressions for the extinction and diffusion cross-sections are then written as follows:

$$\begin{aligned} Q_s &= \frac{2\pi}{k_2^2} \sum_{n=1}^{\infty} (2n+1) \left\{ |a_n|^2 + |b_n|^2 \right\} \\ Q_e &= \frac{2\pi}{k_2^2} \sum_{n=1}^{\infty} (2n+1) \left\{ \mathrm{Re}(a_n + b_n) \right\} \end{aligned} \tag{10}$$

The standardized cross-sections appear immediately:

$$\begin{aligned} Q_{sn} &= \frac{Q_s}{\pi a^2} = \frac{2}{\alpha^2} \sum_{n=1}^{\infty} (2n+1) \left\{ |a_n|^2 + |b_n|^2 \right\} \\ Q_{en} &= \frac{Q_e}{\pi a^2} = \frac{2}{\alpha^2} \sum_{n=1}^{\infty} (2n+1) \left\{ \mathrm{Re}(a_n + b_n) \right\} \end{aligned} \tag{11}$$

where $\alpha = 2\pi a/\lambda_2$ and λ_2 is the incident wavelength in the sphere's external environment.

4.3.1.2.3 Numerical results

The diffusion and extinction cross-sections were calculated at 36 GHz and 94 GHz for particle radii a varying from 0.1 mm to 5 mm (a range including that of the radii of raindrops, which are regarded as spherical).

For these values $\alpha = 2\pi a/\lambda_2$ varies between 0.1 and 10.

The complex refractive index of water was calculated on the basis of Ray's formulas [63]. For an ambient temperature of 15°C the refractive index is equal to 4.83 - i2.73 at 36 GHz and 3.21 - i1.79 at 94 GHz.

Analysis of the results leads to the following:

- the standardized extinction cross-sections Q_{en} tend towards 2 when a increases towards the high values. Q_{en} is clearly stronger in the case of small values of a at 94 GHz than at 36 GHz (a < 1 mm). The extinction cross-sections have approximately the same values in the case of high a values (Figures 4.1 and 4.2);

- diffusion is greater at 94 GHz than at 36 GHz for low values of a, whereas in the case of large radii the albedo tends approximately towards the same values at the two frequencies ($Q_s/Q_e \approx 0.6$) (Figure 4.3).

It can therefore be said, to begin with, that when the rain is light (drizzle or fine rain) the attenuation is clearly more substantial at 94 GHz than at 36 GHz. When the rain rate increases in intensity the proportion of large drops tends to increase and the difference between attenuation at 36 GHz and at 94 GHz becomes less substantial.

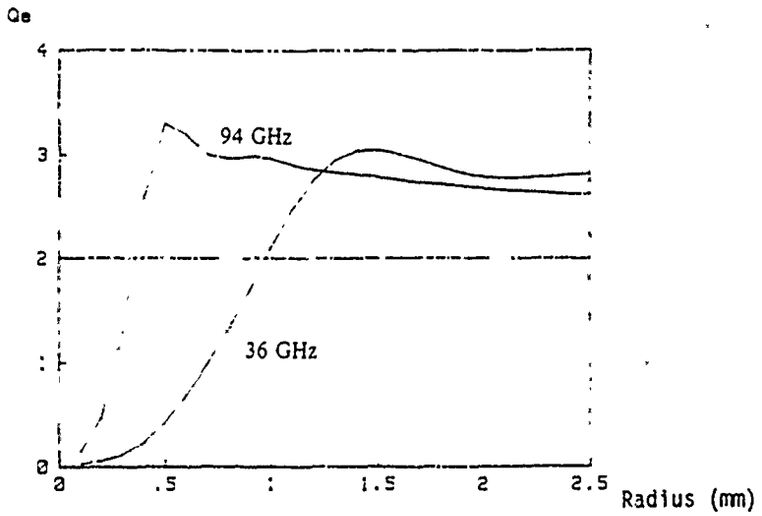

Figure 4.1: Standardized extinction cross-sections at frequencies of 36 GHz and 94 GHz

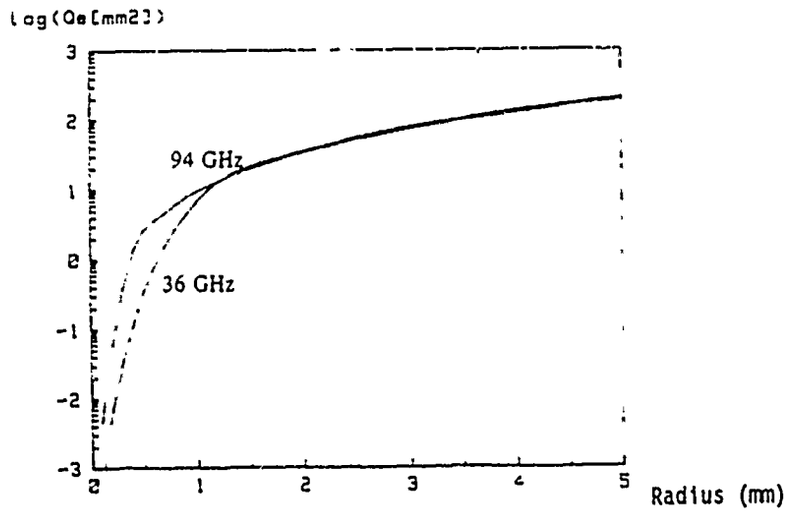

Figure 4.2: Extinction cross-sections in mm at frequencies of 36 GHz and 94 GHz

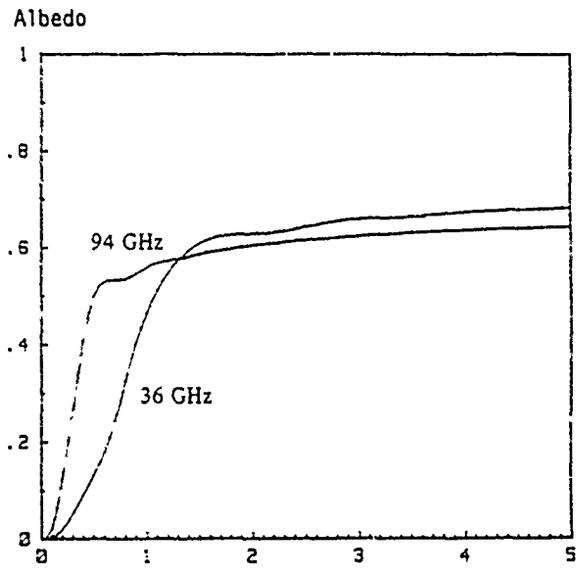

Figure 4.3: Albedo of spherical raindrops at 36 and 94 GHz

The incident energy is substantially absorbed in the case of small radius values (Albedo = very small Q_s/Q_e). When the particle radius increases the proportion of diffused energy rises, becoming preponderant at high values of a.

4.3.1.3 Calculation of specific attenuation due to rainfall

Following calculation of diffusion of an electromagnetic wave by a drop of water, we now deal with the effect of a shower consisting of a large number of drops of rain varying in size.

The drops are assumed to have a diameter distribution N (D) by class intervals centred on D.

Let us then consider a portion of the path d within the rain zone.

In the case of a water drop the total transformed power P_t (D), excluding multiple diffusions, is the product of its cross-section, calculated in the previous paragraph, and the incident power density:

$$P_t(D) = Q_e(D, \lambda)\, p_i \tag{13}$$

For the raindrops as a whole:

$$P_t = \int_0^\infty P_t(D) \cdot N(D)\, dD \tag{14}$$

$$P_t = p_i \int_0^\infty Q_e(D, \lambda)\, N(D)\, dD$$

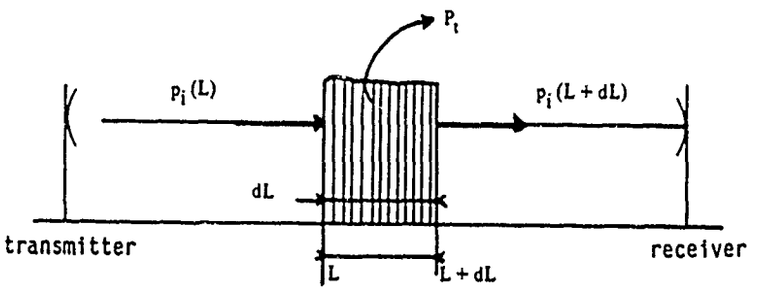

Figure 4.4

We deduce the following, using Figure 4.4:

$$- P_t \, dv = [\, p_i (L + dL) - p_i (L) \,] \, dS$$

i.e.
$$- P_t \, dv = \frac{d\, p_i (L)}{dL} \, dL \, . \, dS \qquad (15)$$

According to (14), and formulating:

$$A = \int_0^\infty N (D) \, Q_e (D, \lambda) \, dD$$

$$d\, p_i (L) = - P_t \, dL = - A \, p_i (L) \, dL \qquad (16)$$

This equation is put in the following form:

$$\frac{d\, p_i (L)}{p_i (L)} = - A \, dL \qquad (17)$$

solution of which leads to the law of attenuation:

$$p_i (L) = p_0 \, e^{- AL} \qquad (18)$$

where p_0 is the initial incident power.

Coefficient A (in Nepers/km) therefore represents attenuation due to rain. Formula (15), expressed in dB/km, becomes:

$$A \text{ (dB/km)} = 4{,}343 \; 10^{-3} \int_0^\infty Q_e (D, \lambda) \, N (D) \, dD \qquad (19)$$

4.3.1.4 Raindrop size distribution

As is apparent in expression (19), specific attenuation is calculated by way of a knowledge of the raindrop size distribution. Measurements of this kind were made for the first time in 1943 by LAWS and PARSONS [64]. Their results supply the percentage in volume of water preciptated for successive diameter ranges for a given rain rate. They were given in tabulated form for rain rates varying from 0.2 mm/h to 152 mm/h and drop diameters (the drops being presumed spherical) up to 7 mm.

This form of presentation is not easy to use, because in practice it requires interpolations. In 1948, MARSHALL and PALMER [65] proposed the representation of distributions in functional form:

$$N(D) = N_0 e^{-\gamma D} \tag{20}$$

with

$$\gamma = \alpha R^{-0.21} \tag{21}$$

where R is the rate of rainfall in mm/h.

This distribution depends upon two parameters N_0 and α supplied in Table 4.1.

This relationship is suitable for measurements over a large range of drop sizes, but it still overestimates the number of small drops.

In 1968 JOSS et al. [66] proposed a refinement in the same form, but with parameters N_0 and α variable according to the type of rain studied (Table 4.1).

Values Type of distribution	N_0 m^{-3} mm^{-1}	α mm^{-1}
Marshall - Palmer	8,000	4.1
Joss et al. drizzle	30,000	5.7
Joss et al. mod. rain	7,000	4.1
Joss et al. storm	1,400	3.0

Table 4.1

The rain rate can be calculated on the basis of the raindrop size distribution:

$$R\ (mm/h) = 3{,}6\ 10^{6}\ \frac{\pi}{6} \int_{0}^{\infty} N\ (D)\ v\ (D)\ D^{3}\ dD \qquad (22)$$

where D is the raindrop diameter (in mm);

N (D) dD is that number of raindrops of diameter between D and D + dD (m^{-3} mm^{-1});

v (D) is the speed of fall of raindrops of diameter D (in m/s).

The relationship universally employed to find the fall velocity of a drop of diameter D is that given by GUNN and KINZER [67]:

$$v\ (D)\ (m/s) = 9{,}65 - 10{,}3\ \exp\ (-\ 0{,}6\ .\ D) \qquad (23)$$

Note on the JOSS et al. distribution

The JOSS et al. distributions should be applied with care. The rain rate used to generate the distribution should be equal to the rain rate deduced from that distribution and from the fall velocity of the raindrops (expression 22). The recalculated values show good agreement when the MARSHALL and PALMER distribution is used, but this is not regularly the case when the expressions of JOSS et al. are used.

4.3.1.5 Calculation of specific attenuation due to rain on the basis of raindrop size distributions

4.3.1.5.1 Calculation programme

A programme for calculating specific attenuation in the millimetre wave region has been implemented on the basis of the integral expression (19).

The input data for this programme are:

- the transmitted frequency;
- the raindrop size distribution;
- the ambient temperature.

A sub-programme is used to calculate the refractive index of the water on the basis of the RAY model.

Integration is by the SIMPSON method over a diameter interval ranging from 0 to 5 mm. The step is fixed at 0.1 m for calculation on the basis of usual distributions. In calculating attenuation on the basis of the experimental distributions, the step will be that imposed by the spectropluviometer data, i.e. 5/16 mm.

4.3.1.5.2 Uncertainty in specific attenuation calculation

(a) Calculation approximations

The error made by reducing the integration interval to 5 mm and in fixing the integration step has been analysed, assuming a MARSHALL-PALMER distribution.

The specific attenuations at 36 and 94 GHz were calculated for this purpose with the following input parameters:

(1) number of steps: 200

integration field: [0.10 mm]

(2) number of steps: 16

integration field: [0.5 mm]

The maximum difference obtained in the rain rate area extending from 0.1 to 20 mm/h is less than 0.03 dB/km.

(b) Error caused by distribution measurement by instruments

The error in specific attenuation was calculated for three rain rates by way of a knowledge of instrument errors relating to the number of drops in each class (Chapter I, paragraph 1.2.4.1) (Table 4.2).

R mm/h	Frequency (GHz) / Distribution	36	94
1	JOSS drizzle	0.008 dB/km (0.33%)	0.013 dB/km (1.11%)
10	MARSHALL-PALMER	0.01 dB/km (1.90%)	0.07 dB/km (0.07%)
30	JOSS storm	0.018 dB/km (1.5%)	0.1 dB/km (1.35%)

Table 4.2

The error remains very small in all cases (< 0.1 dB/km). The difference is a little greater at 94 GHz, since the action of small drops at this frequency is more perceptible.

(c) Variation as a function of ambient temperature

Since the refractive index of water depends upon the ambient temperature, variations in specific attenuation relating to this parameter were also analysed in the range extending from 0°C to 20°C.

Table 4.3 relates to the MARSHALL - PALMER distribution.

R / Frequency	36 GHz	94 GHz
0.1 mm/h	0.02 dB/km (10%)	0.008 dB/km (1%)
1 mm/h	0.001 dB/km (0.01%)	0.04 dB/km (1%)
10 mm/h	0.04 dB/km (1%)	0.06 dB/km (1%)

Table 4.3

The differences in specific attenuation seem to be very slight and are outside the range of accuracy in experimental attenuation determination.

Specific attenuation of millimetre waves by rain in the range of rain rates generally observed on the French Atlantic coast can be accurately calculated on the basis of the usual or measured raindrop size distributions: the absolute maximum cumulative error obtained for high attenuations at 94 GHz is of the order of 0.2 dB/km.

4.3.1.6 Application: Calculation of specific attenuation at 36 GHz and 94 GHz on the basis of $No e^{-\alpha D}$ type distributions

Attenuations at 36 and 94 GHz were calculated for various raindrop size distributions (MARSHALL - PALMER, JOSS et al. drizzle, moderate rain and storm) by the following method in accordance with the note to paragraph 3.1.4:

- N (D) is determined for each rain rate value R according to type of distributions studied (by expressions (20) and (21)).
- The effective rain rate R_{eff} is then recalculated with expression (22).
- Specific attenuation A is likewise calculated on the basis of integral (19).

The A - R_{eff} curve is then drawn.

The results appear in Figs 4.5 and 4.6, the ambient temperature being 15°C.

The effect of the raindrop distributions is more perceptible at 94 GHz than at 36 GHz. This flows from the variations in raindrop effective cross-sections as a function of diameter.

An illustration of variations due to the types of distribution is given in Table 4.4. It can be seen that at 94 GHz the higher the rain rate, the greater the variations in attenuation.

Rain rate	Variation in attenuation at 36 GHz	Variation in attenuation at 94 GHz
0.1 mm/h	8%	30%
1 mm/h	15%	40%
10 mm/h	10%	50%

Table 4.4

Attenuation at 36 GHz is 0.2 dB/km at a rain rate of 1 mm/h, although attenuation at 94 GHz is 1 dB/km, i.e. a power loss factor of 4.

This factor tends to decrease towards high rain rates. Raindrop size becomes greater on average and the effective cross-sections corresponding to 36 GHz and 94 GHz tend to come closer to each other (Figure 4.2).

4.3.1.7 Seeking a simple relationship linking attenuation to rain rate

Figures 4.5 and 4.6 suggest definition of an exponential-type relationship between attenuation A (in dB/km) and the rain rate (in mm/h):

$$A = a R^b \qquad (24)$$

a and b are two parameters to be determined. They depend upon the frequency and the N (D) distribution used.

A theoretical justification for this expression can be found in reference [68]. It is based on expression (19) linking attenuation to the raindrop size distribution of type $Noe^{-\alpha D}$ and to the effective cross-section developed as a limited series on the basis of parameter $2\pi a/\alpha$.

A nonlinear regression programme was applied to the file containing the attenuations (at 36 GHz and 94 GHz) and the rain rates previously calculated on the basis of N (D), to find coefficients a and b.

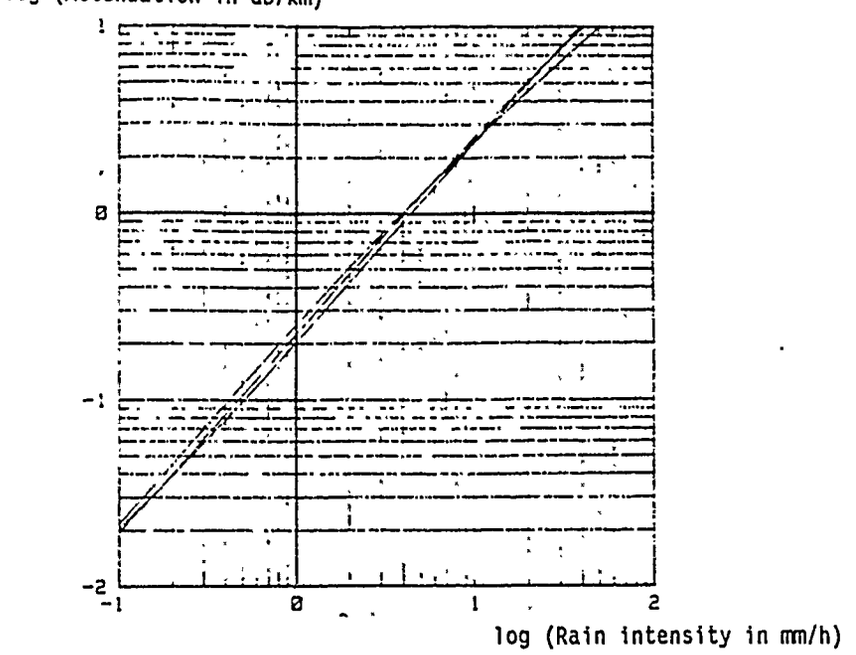

Attenuation by rain at 36 GHz (T = 15 °C)

Figures 4.5 and 4.6 Specific attenuation at 36 & 94 GHz calculated on the basis of raindrop size distributions: JOSS drizzle (J-B), MARSHALL-PALMER (M-P) and JOSS storm (J-O)

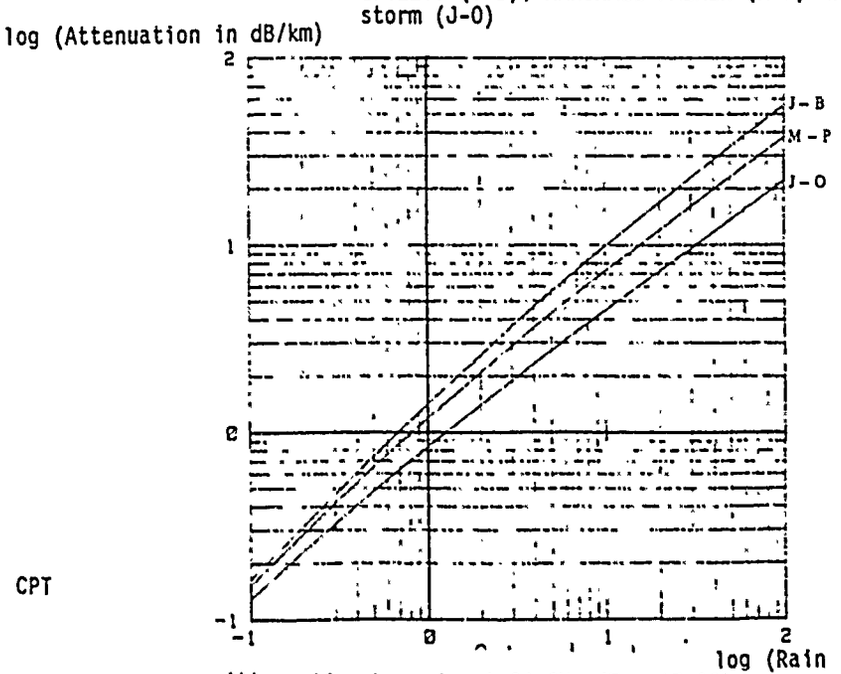

Attenuation by rain at 94 GHz (T = 15 °C)

CPT

The results (Table 4.5) are valid in the [0.1 mm/h, 50 mm/h] area. On the one hand they can be used to calculate attenuation easily and with a high level of accuracy and on the other hand they are useful in certain computation methods (determination of rain cell characteristics on the basis of a knowledge of attenuation at several frequencies [69] [70]).

Type of distribution	a_{36}	b_{36}	a_{94}	b_{94}
MARSHALL-PALMER	0.277	0.974	1.359	0.732
JOSS et al. drizzle	0.223	1.037	1.696	0.768
JOSS et al. moderate	0.275	0.975	1.310	0.732
JOSS et al. storm	0.290	0.930	0.846	0.733

Table 4.5

4.3.2 Experimental determination of attenuation by rain

4.3.2.1 Experimental raindrop size distributions

The spectropluviometer used during a three-month measuring campaign in Autumn-Winter 84-85 provided a rain gauge data base covering the types of rain most frequently encountered on the North Atlantic coasts during this time of year.

The measured distributions for the various types of rain were compared with the usual MARSHALL-PALMER or JOSS et al. distributions for the various types of rain at the same rain rate.

(a) Drizzle

Drizzle is fine rain, which rain rate is less than a few tenths of mm/h. This type of rain rate is frequently encountered on the Breton coast and usually lasts for several hours. Examination of the distribution figures (Figure 4.7 - a, b) shows that only the first three or four classes are non-zero (diameter less than 1.2 mm). The "JOSS drizzle" distribution is in agreement with the measurements, except for the first class, in which the number of drops is overestimated.

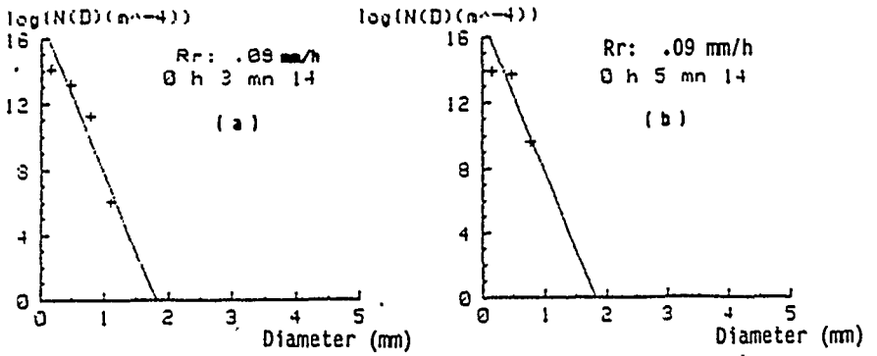

11 / 11 / 84 (JOSS drizzle distribution : ____)

Figure 4.7

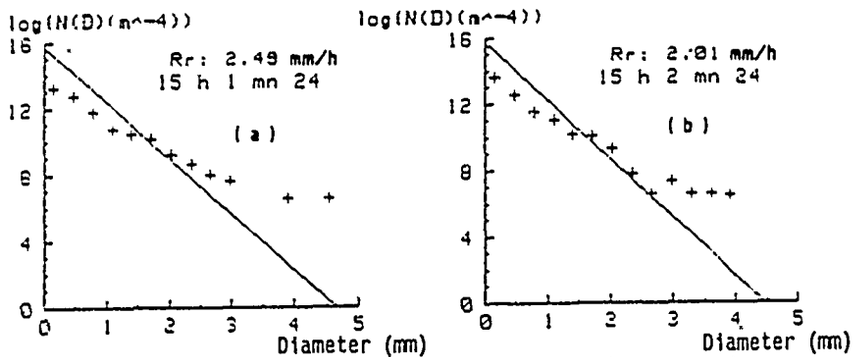

5 / 11 / 84 (JOSS moderate distribution : ____)

Figure 4.8

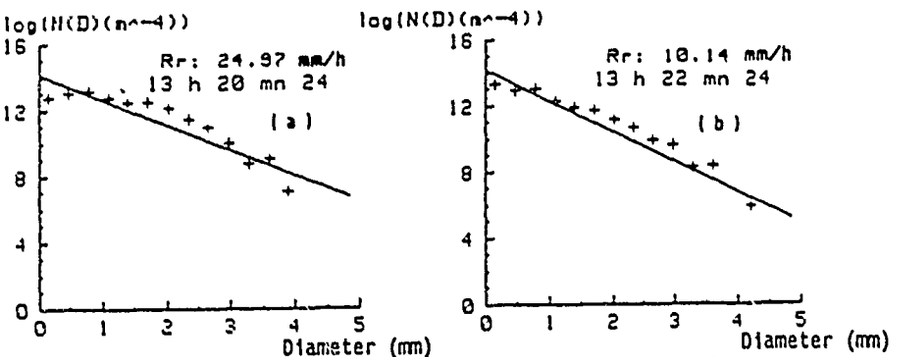

2 / 11 / 84 (JOSS storm distribution : ____)

Figure 4.9

Measured raindrop size distributions

The spectropluviometer principle permits measurement of this type of rain, whereas conventional rain-gauges like the bucket-type instrument are insensitive to it.

(b) Moderate rain

The measured distributions (Figure 4.8 - a, b) are in close agreement with the MARSHALL-PALMER or "JOSS moderate" distributions. Nevertheless, these distributions overestimate the number of drops in the small classes. In the large classes the measured values are often above those given by exponential distributions.

Drops which may reach a diameter of 4 mm have been measured.

(c) Heavy rain

Rain which is heavy for the region lasting several minutes has been recorded simultaneously by the spectropluviometer at GAVRES and the bucket-type rain-gauge at GROIX. During this type of downpour, the rain rate sometimes exceeded 30 mm/h. The corresponding distributions (Figure 4.9 - a, b) are close to the "JOSS - storm" distributions. The latter tend to overestimate the number of drops in the extreme classes and to underestimate the intermediate classes.

4.3.2.2 Study of specific attenuation determined on the basis of measured raindrop size distributions

Where the experimental raindrop size distribution is available, the specific attenuation can be calculated accurately and compared with attenuations deduced from the usual distributions. This work has been carried out with representative showers at 36 GHz and 94 GHz. They demonstrate the close agreement which exists with curves deduced from the usual distributions (Figures 4.10, 4.11 and 4.12).

However, it is apparent that at 36 GHz, when the rain rate exceeds a few mm/h the attenuations calculated on the basis of the experimental distributions are often above the "theoretical" distributions. This difference is due to the form of the distribution, which shows a greater number of drops in the intermediate classes, and sometimes in the large classes.

At 94 GHz the measurement point dispersion is greater. It proves experimentally the sensitivity of the attenuation at 94 GHz to the raindrop size distributions; the rain rate is insufficient for the accurate calculations of the specific attenuation.

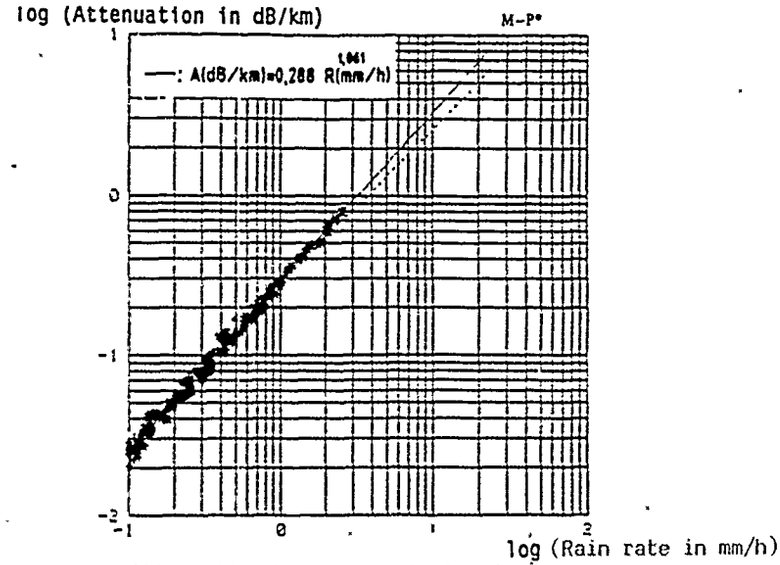

Attenuation by rain at 36 GHz (T = 15 °C)
5 / 11 at 14 h 0 to 6 / 11 at 3 h 0

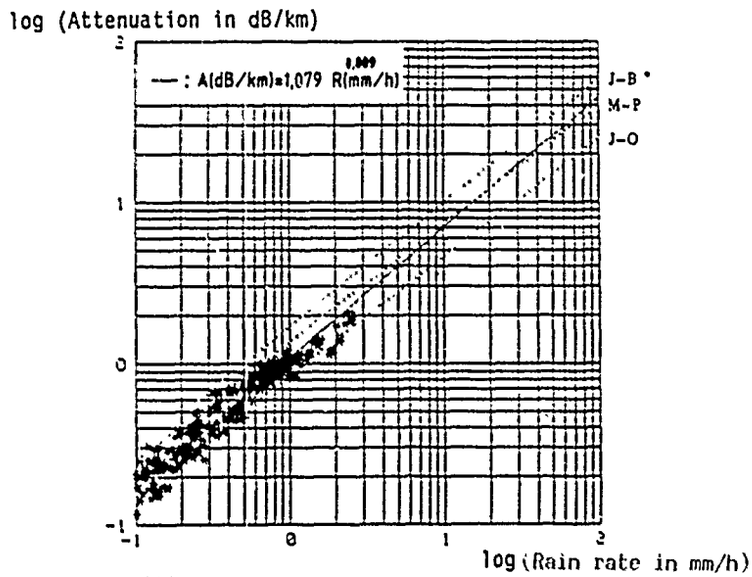

Attenuation by rain at 94 GHz (T = 15 °C)
5 / 11 at 14 h 0 to 6 / 11 at 3 h 0

Figure 4.10 a & b: Specific attenuation at 36 & 94 GHz - Moderate rain

* J-B, M-P, J-O } Theoretical attenuation calculated with JOSS drizzle, MARSHALL-PALMER, JOSS storm distributions

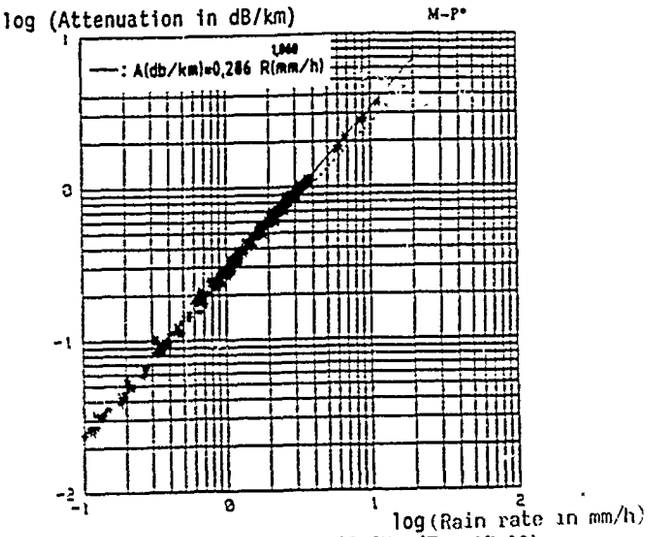

Attenuation by rain at 36 GHz (T = 15 °C)
15 / 11 at 20 h 0 to 16 / 11 at 9 h 0

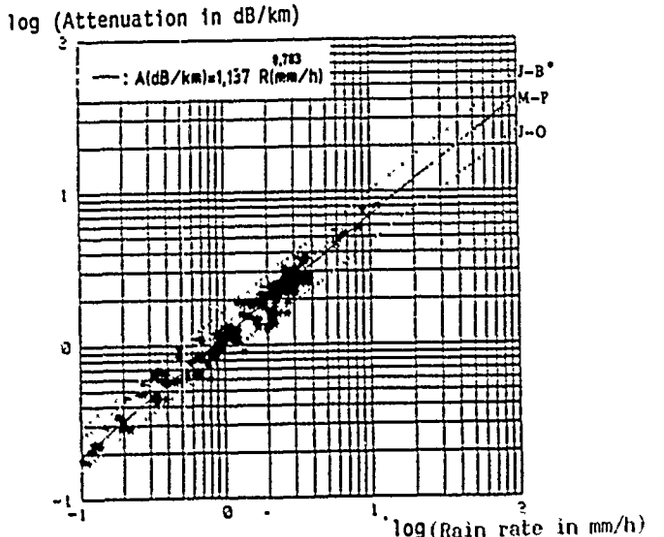

Attenuation by rain at 94 GHz (T = 15 °C)
15 / 11 at 20 h 0 to 16 / 11 at 9 h 0

Figure 4.11 a & b: Specific attenuation at 36 & 94 GHz - Moderate rain

* J-B, M-P, J-O } Theoretical attenuation calculated with JOSS drizzle, MARSHALL-PALMER, JOSS storm distributions

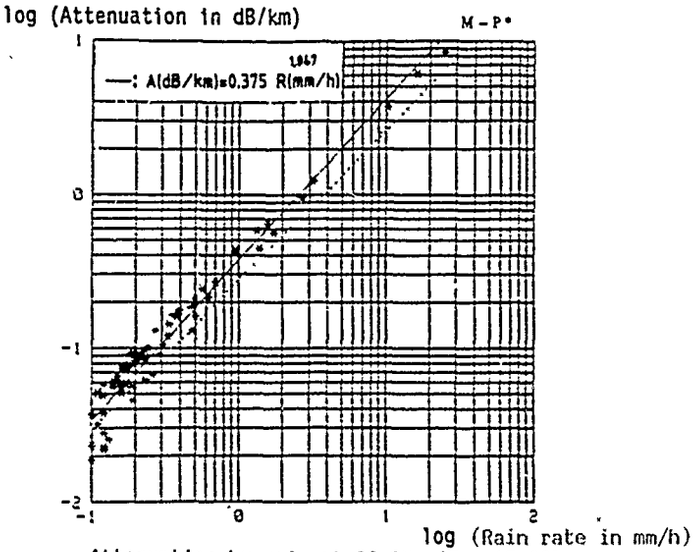

Attenuation by rain at 36 GHz (T = 15 °C)
2 / 11 at 10 h 0 to 2 / 11 at 15 h 0

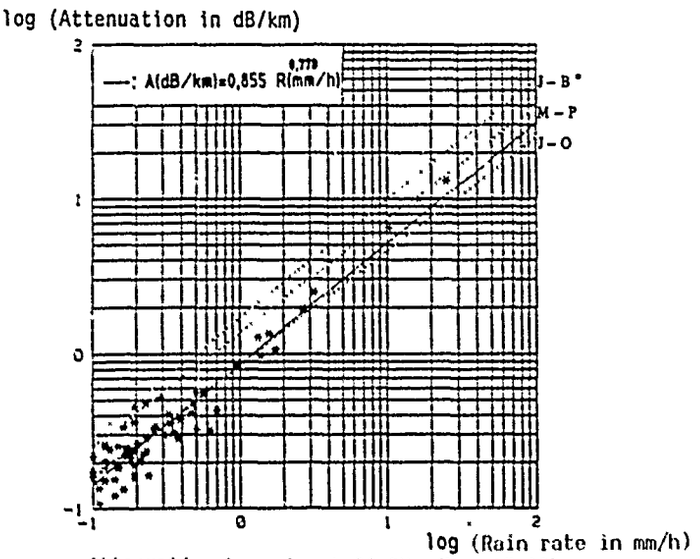

Attenuation by rain at 94 GHz (T = 15 °C)
2 / 11 at 10 h 0 to 2 / 11 at 15 h 0

Figure 4.12 a & b: Specific attenuation at 36 & 94 GHz - Storm rain

* J-B, M-P, J-O } Theoretical attenuation calculated with JOSS drizzle, MARSHALL-PALMER, JOSS storm distributions

4.3.2.3 Attenuation on the link calculated on the basis of rain gauge data

Specific attenuation A_R at the reception site is known, by reference to measurements supplied by the spectropluviometer. Where the rain rate is available, it is interesting to determine coefficients a and b of the relationship by a least-square method:

$$A_R \text{ (dB/km)} = a R_R^b \text{ (mm/h)} \qquad (25)$$

(For the incidents described previously, these coefficients are shown in the corresponding Figs. 4.10, 4.11 and 4.12).

In fact this relationship can be used to calculate the specific attenuation A_E at the transmission site. It is assumed for this purpose that the particle-size structure of the rain is identical on both sides of the link. The attenuation A_E can therefore be written as follows:

$$A_E = a R_E^b \qquad (26)$$

where R_E is the rain rate recorded by the bucket-type rain gauge.

In the cases dealt with, in which it was raining simultaneously on both sides of the link, the overall attenuation due to rainfall was simply calculated as the arithmetic mean of the specific attenuations A_E and A_R multiplied by the distance of the link:

$$A \text{ (dB)} = 9.7 \left(\frac{A_E + A_R}{2} \right) \qquad (27)$$

4.3.2.4 Calculation of attenuation by rain from propagation data at 36 GHz

Determining attenuation actually due to rain calls for a knowledge of the interference figure in an undisturbed atmosphere. This is reconstituted on the basis of the method set out in Chapter III, paragraph 3.2.

Processing is difficult. The positioning of the FRESNEL ellipsoid tangential points with the sea may in fact no longer correspond to the extrema. Reconstitution of the tide contour is then based on extrema due to the double path. In periods of rain, the position of these points is interpolated taking account of the sinusoidal contour of the tide. On the basis of the amplitude of successive extrema due to the effect of the tide, the coherent reflection coefficient is continuously available in the same way by interpolation over the periods of rain and then smoothing.

This treatment provides variations in the received signal level in time in the absence of rain by applying the coherent reflection model described in detail in Chapter II, paragraph 3.5.2 (Figure 4.13). Attenuation due to rain on the link is arrived at by the subtraction of these variations from those corresponding to the signal level actually picked up by the reception antenna.

4.3.2.5 Experimental results at 36 GHz

Attenuations deduced from the received signal level have been compared with those calculated on the basis of rain gauge data for a certain number of incidents corresponding to moderate or heavy rain (Figures 4.14 a and b, 4.15 a and b).

Close agreement in time is apparent between measured attenuations and calculated attenuations over all the cases dealt with. Nevertheless the dispersion diagrams relating to these values show fairly wide point scattering centred on the equal attenuation line. This wide dispersion arises basically from the assumptions made on the rain cell disrupting the link.

This rain zone does not always have a uniform contour like that defined in the model. In addition, rain gauge data only at the two ends of the link do not reveal the true rain profile and cannot be used to determine attenuation over the link at each point in time.

On the other hand, the cumulative probability curves for measured attenuations and calculated attenuations relating to the incidents as a whole are very close to each other (Figure 4.15). These curves have been drawn starting from 2 dB ($\approx$ 0.2 dB/km) because of the data reduction errors affecting weak attenuations.

This curve demonstrates the validity of the model.

When it rains simultaneously at the two ends of a link about 10 km or less in length, the frequency of the attenuations in the millimetre wave range can be correctly assessed on the basis of the raindrop size distribution recorded at one end of the link and the rain rate measured at the other.

NOTE: A model taking account of the displacement of rain cells would call for assumptions which cannot be readily verified and which would lead to complex computations. In short, it would not greatly affect the results.

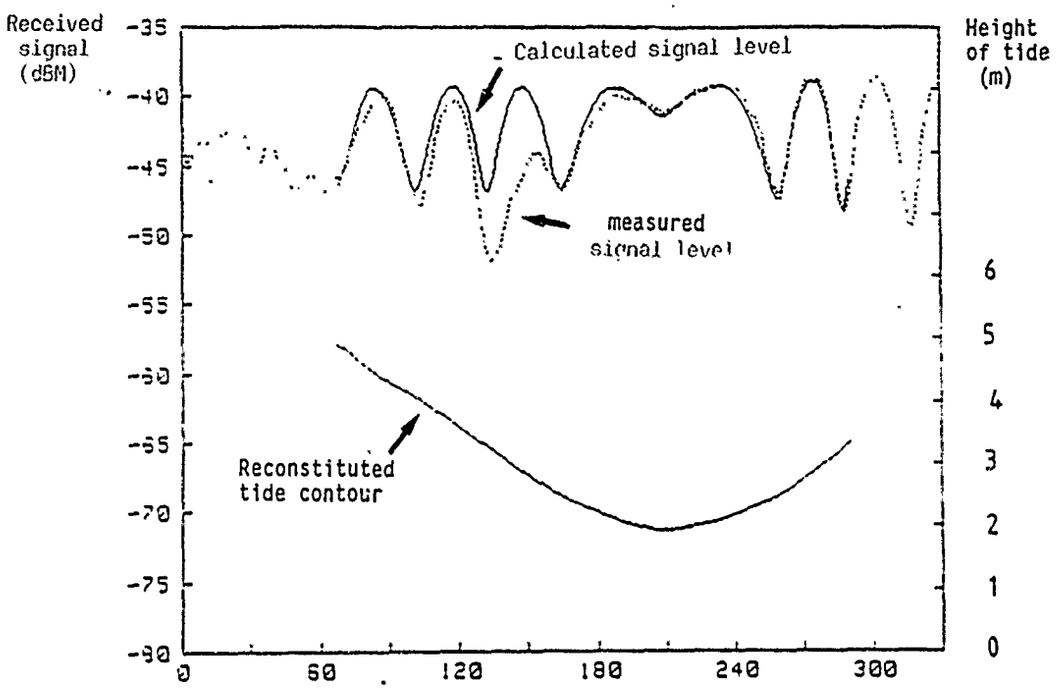

5 / 11 / 84 from 14 H 0 MN to 6 / 11 / 84 at 1 H 0 MN
Frequency = 36 GHz K = 1.33

Figure 4.13: Reconstitution in time of received signal level with rain present

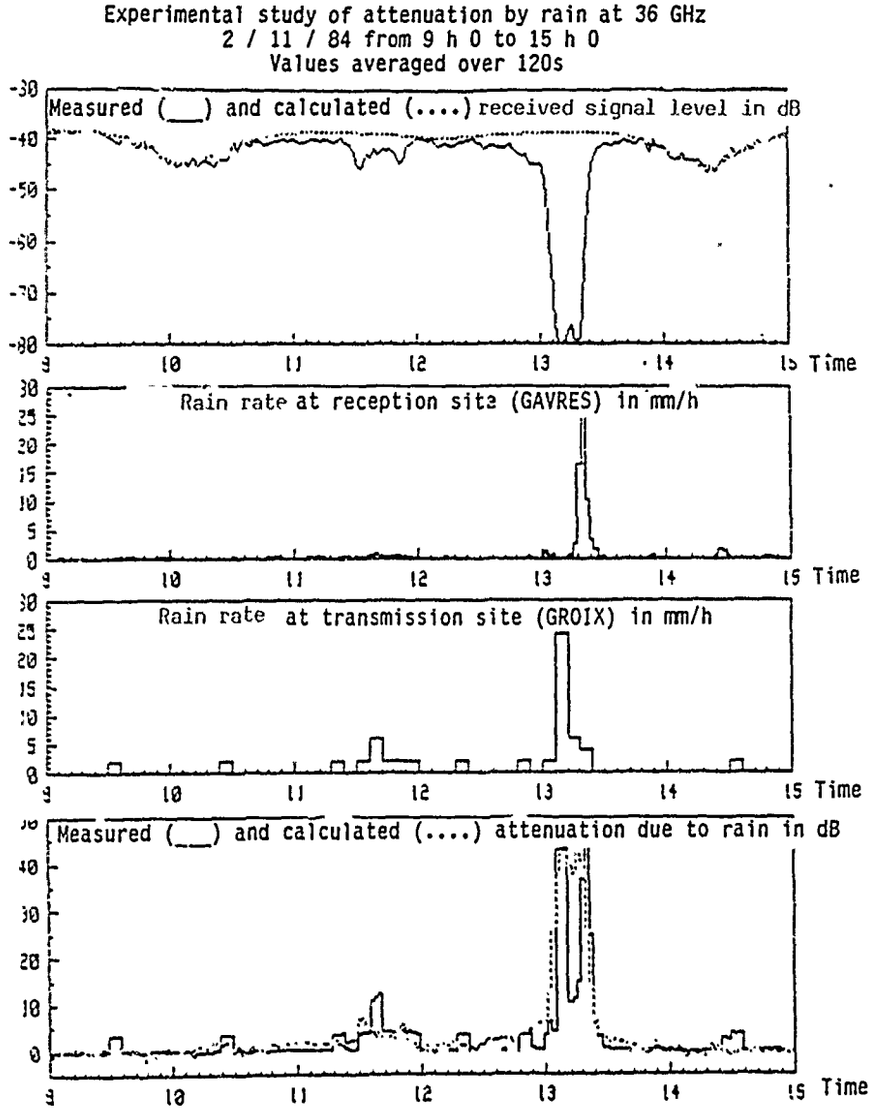
Experimental study of attenuation by rain at 36 GHz
2 / 11 / 84 from 9 h 0 to 15 h 0
Values averaged over 120s
Measured (___) and calculated (....) received signal level in dB
-30
-40
-50
-60
-70
-80
9
10
11
12
13
14
15 Time
Rain rate at reception site (GAVRES) in mm/h
30
25
20
15
10
5
0
Rain rate at transmission site (GROIX) in mm/h
Measured (___) and calculated (....) attenuation due to rain in dB
40
30
20
10
0

Figure 4.14 a

log (measured attenuation)

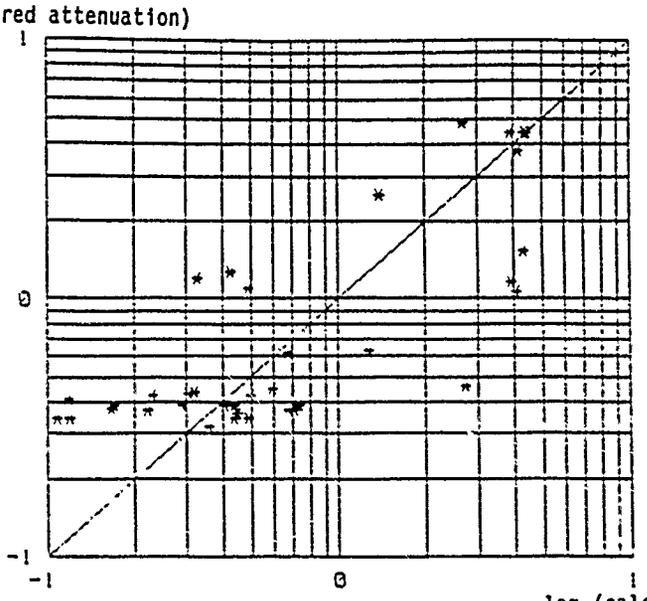

log (calculated attenuation)

Attenuation by rain at 36 GHz (in dB(Km)
From 2 / 11 at 11 h 0 to 2 / 11 at 15 h 0

log (measured attenuation)

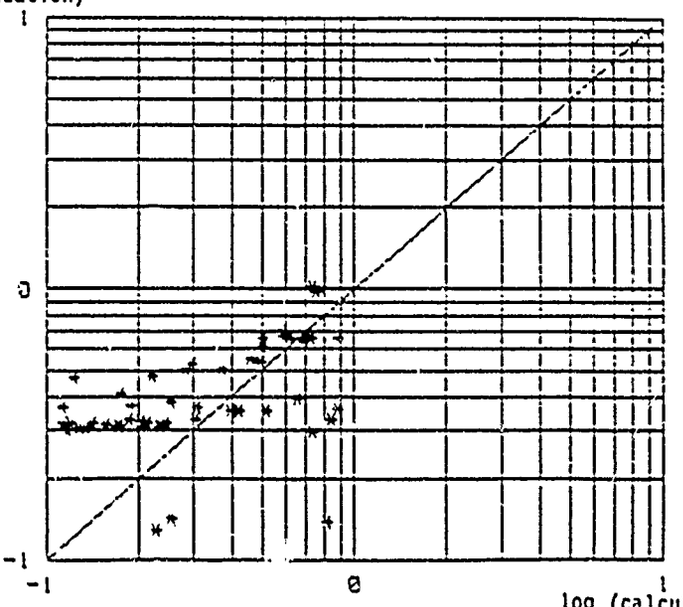

log (calculated attenuation

Attenuation by rain at 36 GHz (in dB(Km)
From 5 / 11 at 16 h 0 to 5 / 11 at 21 h 0

Figure 4.14 b & 4.15 b: Calculated and measured attenuation dispersion diagrams

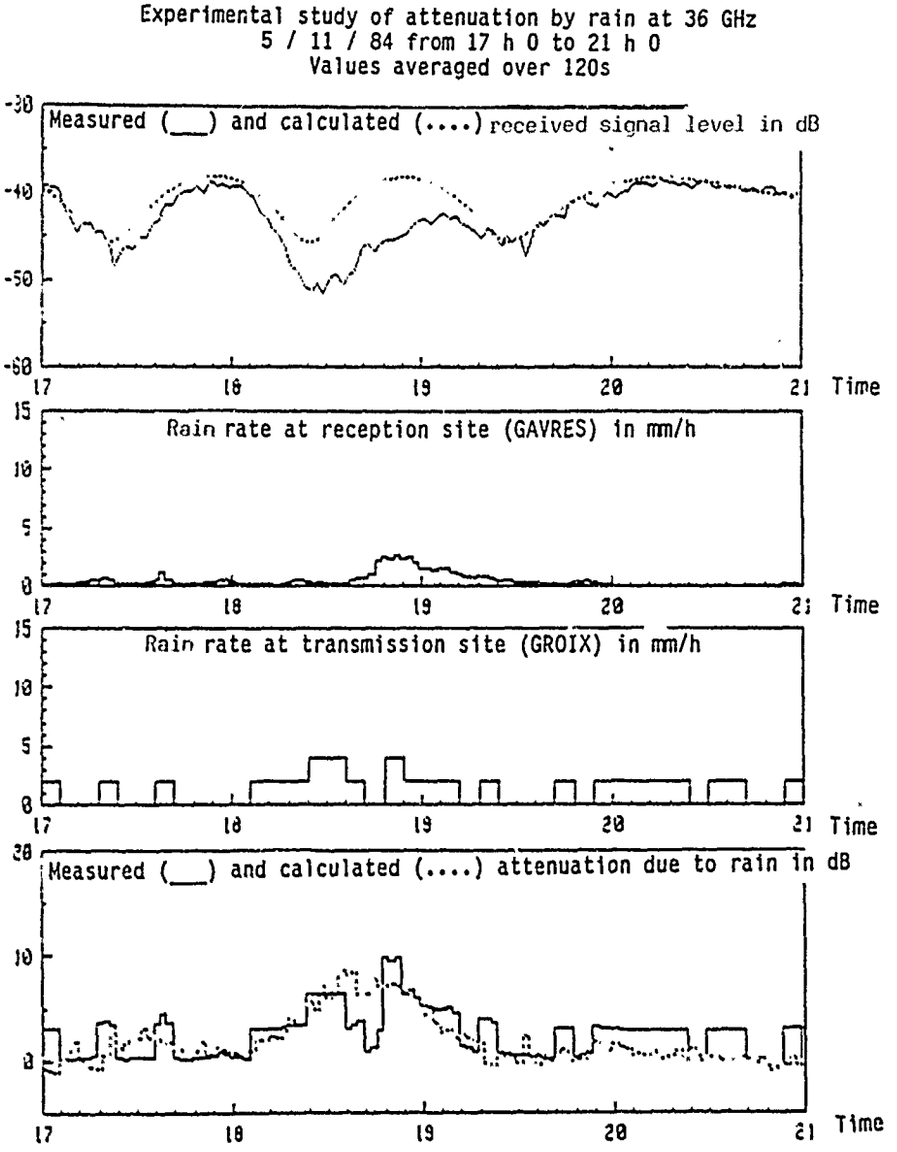
Experimental study of attenuation by rain at 36 GHz
5 / 11 / 84 from 17 h 0 to 21 h 0
Values averaged over 120s
Measured (___) and calculated (....) received signal level in dB
-30
-40
-50
-60
17
18
19
20
21
Time
Rain rate at reception site (GAVRES) in mm/h
15
10
5
0
Rain rate at transmission site (GROIX) in mm/h
Measured (___) and calculated (....) attenuation due to rain in dB
20
10
0

Figure 4.15 a

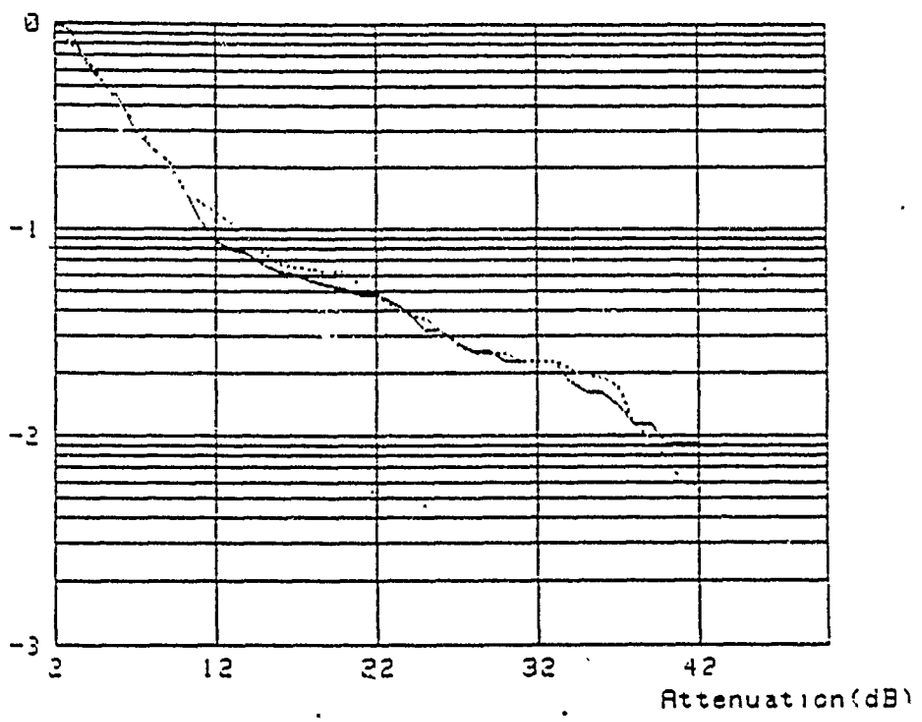

Cumulative probabilities of measured (....) and calculated (___) attenuations over 120 s

Measurement campaign at LORIENT 1984-85

Figure 4.16

4.3.3 Duration of rainfall

The distribution in a given place of rainfall exceeding a fixed duration threshold is of interest in the context of studies of reliability of centimetre or millimetre wave links. Subject to extrapolation of the rainfall rate over the entire link, this information makes it possible to determine the duration of marked attenuation due to rain.

A study of this kind was carried out on measurements collected at a sampling time of 60 seconds, since a substantial rain gauge data base had been acquired by the spectropluviometer. The rain rate thresholds were set at 0.5, 1, 4 and 10 mm/h.

Previous studies [71] have shown that the duration of rainfall had an approximately lognormal distribution:

$$Pr(D_s)[\%] = \frac{100}{\sigma\sqrt{2\pi}} \frac{1}{D_s} \exp\left[-\frac{1}{2}\frac{(\ln D_s - m)^2}{\sigma^2}\right] \qquad (28)$$

where σ is the standard deviation of the Nepierian logarithm of rainfall duration.

	Total number of cases	Median value	Maximum duration
0.5 mm/h	204	3.40 mn	95 mn
1 mm/h	175	3.15 mn	56 mn
4 mm/h	63	1.80 mn	27 mn
10 mm/h	15	1.45 mn	6 mn

Table 4.6

m is the mean value of the Nepierian logarithm of rainfall duration;

exp(m) is called the median value of rainfall duration.

The data were interpreted along these lines (Table 4.6). It is noteworthy that in Figures 4.17 a, b, c and d there is relatively close agreement between the measurement points and the line of the lognormal distribution so long as the number of incidents is sufficient. It is apparent

that the median value of the rainfall duration is a decreasing function of the threshold.

The study cannot be used to prove that the median is inversely proportional to the threshold values for the rain rates as specified in CCIR Report 563-2, because of the limited duration of the experiments and the insufficient number of thresholds.

4.3.4 Statistical study of attenuation by rain at 95 GHz

The cumulative rainfall rate and signal level probabilities at 95 GHz were calculated in connection with the link set up in 1981-82 in order to show the effect of rain upon the statistical behaviour of millimetre wave links. The study covers about 75 days.

4.3.4.1 Rainfall rate

The bucket-type rain gauge recorded the rain rate every 10 seconds. Its sensitivity was 1.8 mm/h.

The cumulative distribution curve is regular up to 16 mm/h (Figure 4.18).

It subsequently falls, due to excess of incidents of heavy rain, since the experiment is limited to a few months. It should be noted that the rain gauge recorded rain rates up to 28 mm/h.

4.3.4.2 Signal levels at 95 GHz

During the measurement campaign the received signal level was recorded on two polarisations (horizontal and vertical) at a rate of 10 seconds.

The total operating time was 1703 hours. Examination of the curves (Figure 4.19) shows that polarisation has no significant effect upon the received signal level values. For a given percentage of time the difference in attenuation remains approximately constant, generally less than 2 dB, even in the case of heavy attenuations. The signal is substantially more attenuated in horizontal polarisation. These observations are along the lines of the theory to the effect that the horizontally polarised wave is more attenuated. In fact when the rain rate increases the raindrops become larger and are deformed along the horizontal axis; for this polarisation their cross-sections increase with increasing deformation.

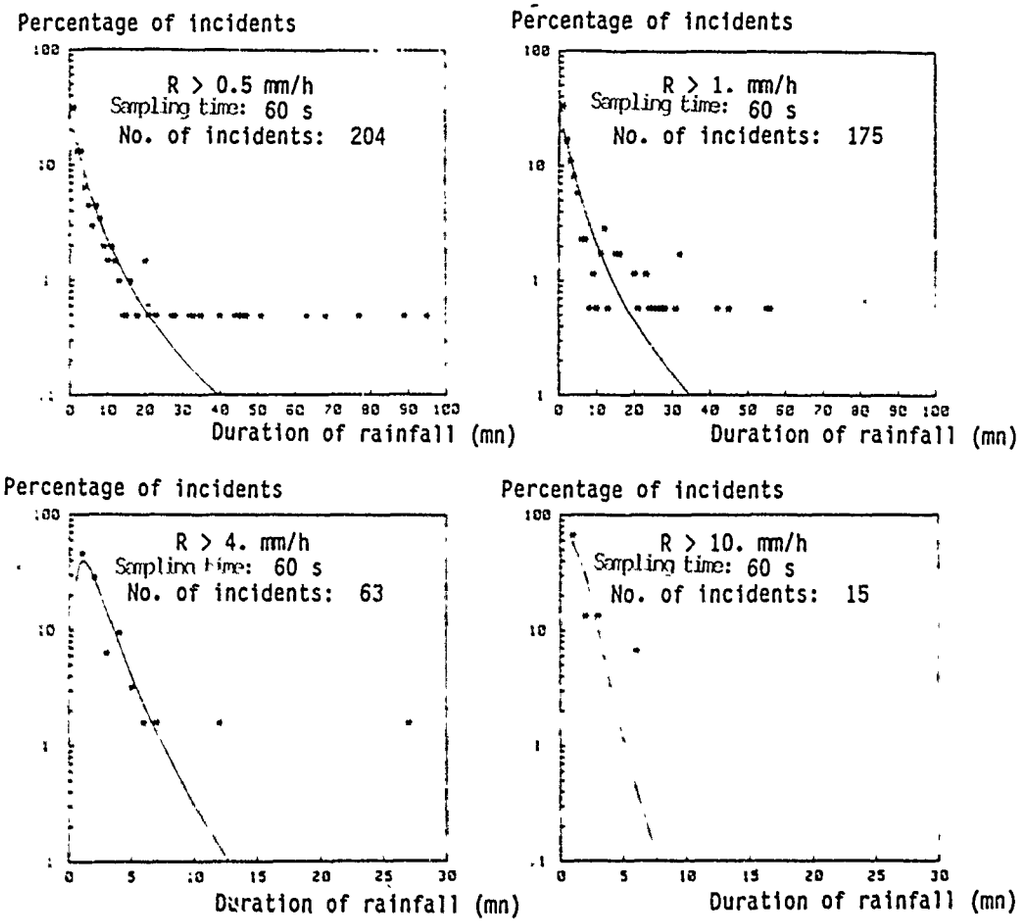

Figure 4.17: Duration of rainfall as a function of the threshold

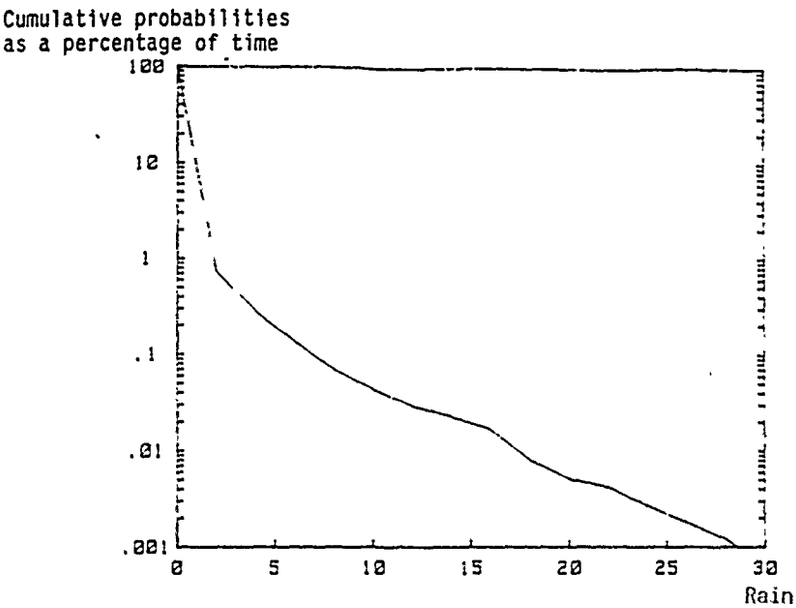

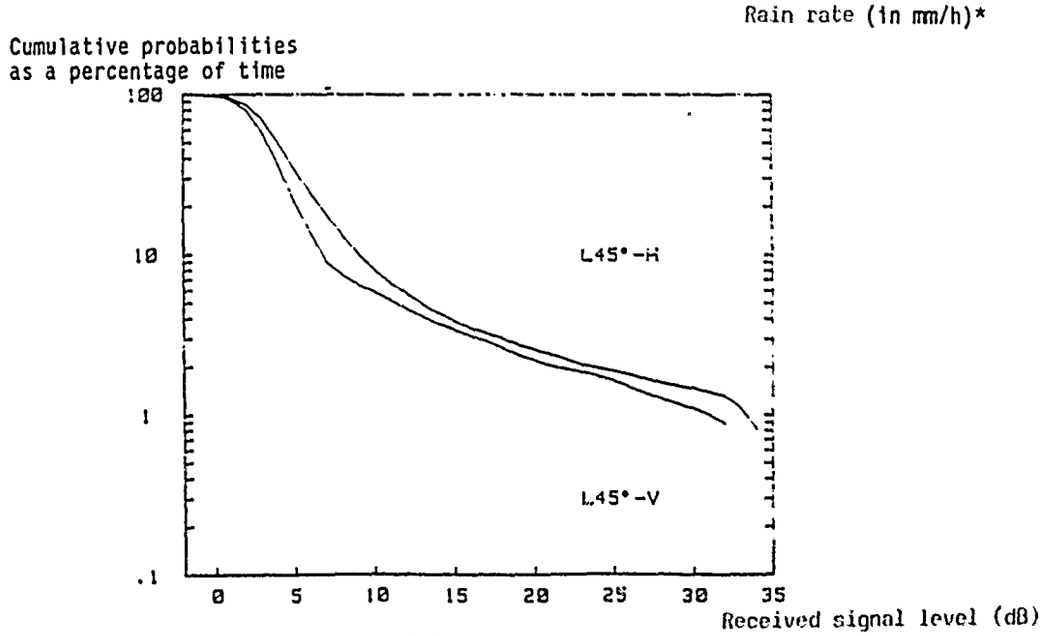

Figures 4.18 & 4.19: Rain gauge and received signal level statistics at 95 GHz

* Averaged over 3 values: measurement sampling time 30 s

However, it is not possible in this experiment to link the difference in attenuation in the direction of polarisation correctly with the rain rate. The link length was 9.7 km: consequently low rain rates over a substantial part of the path might have an attenuating effect as great as heavy localised rainfall, where the large raindrops are deformed. It should also be stressed that the rain rates recorded did not exceed 30 mm/h. This corresponds to rainfall which is certainly substantial but which is nevertheless slight in comparison to tropical rainfall, with rates larger than 100 mm/h. The raindrops are then clearly more deformed on the average. The theoretical difference in attenuation between the two polarisations is multiplied by a factor of three at 94 GHz when the rain rate varies from 30 to 100 mm/h [72].

4.4 ATTENUATION DUE TO OTHER HYDROMETEORS

4.4.1 Attenuation due to fog

4.4.1.1 Specific attenuation

Fog is composed of minute water particles which usually do not exceed a few tens of microns in diameter.

Fog is defined by its liquid water vapour content or by visibility (it should be noted that, in the meteorological sense of the term, fog is present when visibility is equal to or less than 1 km).

A distinction is usually drawn between two types of fog:

- advection fog, which forms when a mass of warm moist air moves above a colder surface;
- convection fog, which forms when the layer of air close to the ground becomes saturated with water as it cools on contact. This is the situation with the fogs which sometimes occur at the beginning of the day.

Attenuations caused by fog are slight, because of the small size of the particles in relation to millimetre wavelengths. This is apparent in Table 4.7, in which specific attenuation for advection and convection fogs is given as a function of visibility [73].

Attenuation (in dB/km) / Visibility	Convection fog		Advection fog	
	36 GHz	94 GHz	36 GHz	94 GHz
100 m	0.08	0.34	0.45	1.85
200 m	0.03	0.12	0.14	0.60
300 m	0.015	0.06	0.07	0.30
500 m	0.007	0.03	0.02	0.12
1 km	0.002	0.01	0.01	0.03

Table 4.7

Only very thick advection fogs give rise to an attenuation value of 1 dB/km at 94 GHz.

4.4.1.2 Experimental study

A satisfactory experimental study of attenuation due to fog was not possible, for the following reasons:

- it was not possible to measure visibility automatically during the experiments. The only visibility data gathered were visual estimates made at the reception site and at the Ile de GROIX semaphore;
- the phenomenon of reflection on the sea prevents a very accurate assessment of the received signal level in the absence of fog;
- lastly, in Brittany the fog is sometimes associated with fine rain, causing additional attenuation.

Nevertheless attenuations due wholly or partly to fog were recorded, taking observations and meteorological measurements into account (Table 4.8):

Date	Period	Wind	Air temp. °C	Relative humidity	Visibility	Attenuation in the 36 GHz band	Attenuation in the 94 GHz band	Observations
9/12 Fig. no. 4.20	4 h - 14 h	< 2 m/s Sector E	3 - 4 °C	100 %	Semaphore 7 h: 30 m 13 h: 80 m	≈ 3 dB	6 dB	Spectropluviometer out of action. Fine rain present.
12/12 Fig. no. 4.21	8 h - 11 h	≈ 4 m/s	Between 5 °C and 10 °C	95%	Semaphore 13 h: 60 m	Not measurable	≈ 3 dB	Fine rain < 0.07 mm/h
17/1 Fig. no. 4.22	10 h - 24 h	5-7 m/s Sector E	Between -5 °C and 0 °C	90%	Semaphore 13 h: 100 m 19 h: 80 m	Not measurable	≈ 3 dB	Intermittent fine rain

Table 4.8

Even in the case of very thick fogs the specific attenuation, assuming the precipitation to be homogenous, did not exceed 0.6 dB/km at 94 GHz. Specific attenuation at 36 GHz is very slight (0.3 dB/km maximum) and cannot be determined with accuracy.

4.4.2 Attenuation due to snow

4.4.2.1 General

Snow, which consists of ice crystals, is difficult to define by a single parameter. Its constituent crystals may take many forms and contain variable amounts of liquid water. Consequently a distinction is drawn between wet snow, containing a large quantity of liquid water, and dry snow.

Experimental results are few in number [74], [56]. They reveal that attenuation caused by snow in the millimetre wave region is slight.

4.4.2.2 Experimental results

Snowfall incidents were recorded during January 1985. The corresponding periods are listed in Table 4.9.

This study can be qualitative only, being based on visible observations at the reception site and at the Ile de GROIX semaphore.

Date	Time	Air temp.	Wind		Observations
			Amplitude	Direction	
8/1 Fig. 4.23	15 h	≈ -1 °C	5 m/s	S.S.W.	Very small not visible attenuation
8/1 Fig. 4.23	17 h - 22 h	0 °C	10 m/s	S.S.W.	High attenuation at all frequencies - wet snow
16/1 Fig. 4.24	9 h - 13 h	-3 °C -2 °C	4 m/s	E.N.E.	Attenuation not measurable

Table 4.9 - Snowfalls

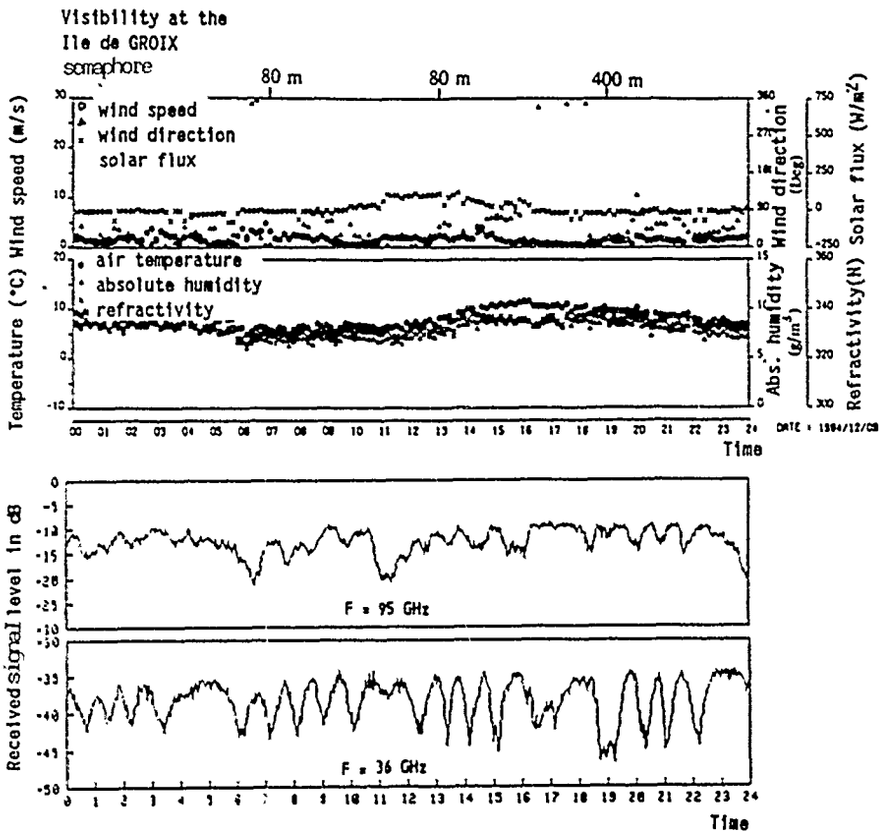

Figure 4.20: Attenuation caused by fog

9 - 12 - 1984 at LORIENT

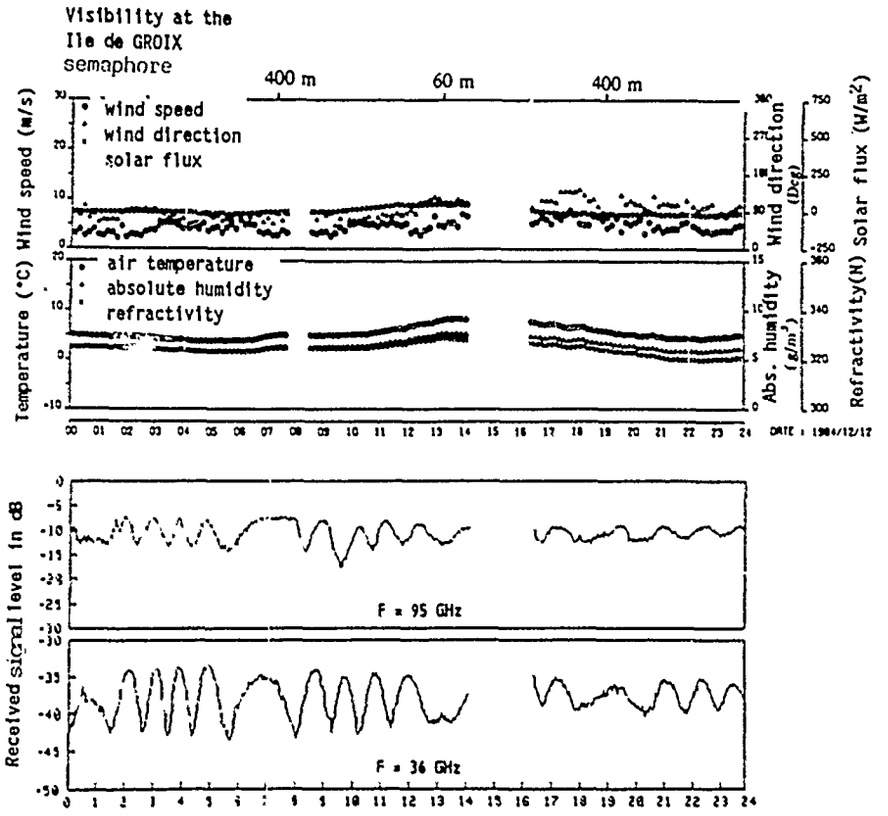

Figure 4.21: Attenuation caused by fog
12 - 12 - 1984 at LORIENT

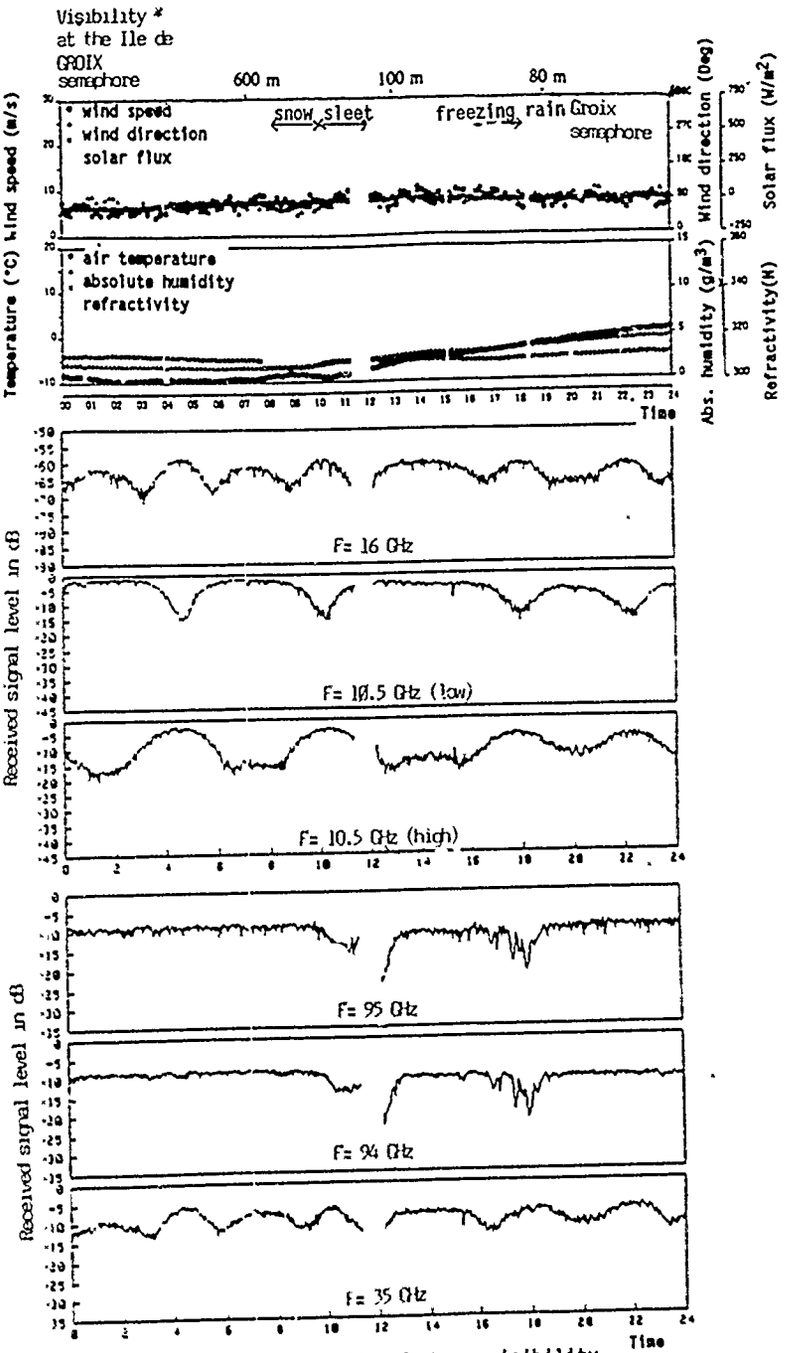

Figure 4.22: Propagation in low visibility
17 - 1 - 1984 at LORIENT

* Low visibility observed at Gâvres as from 10 p.m.

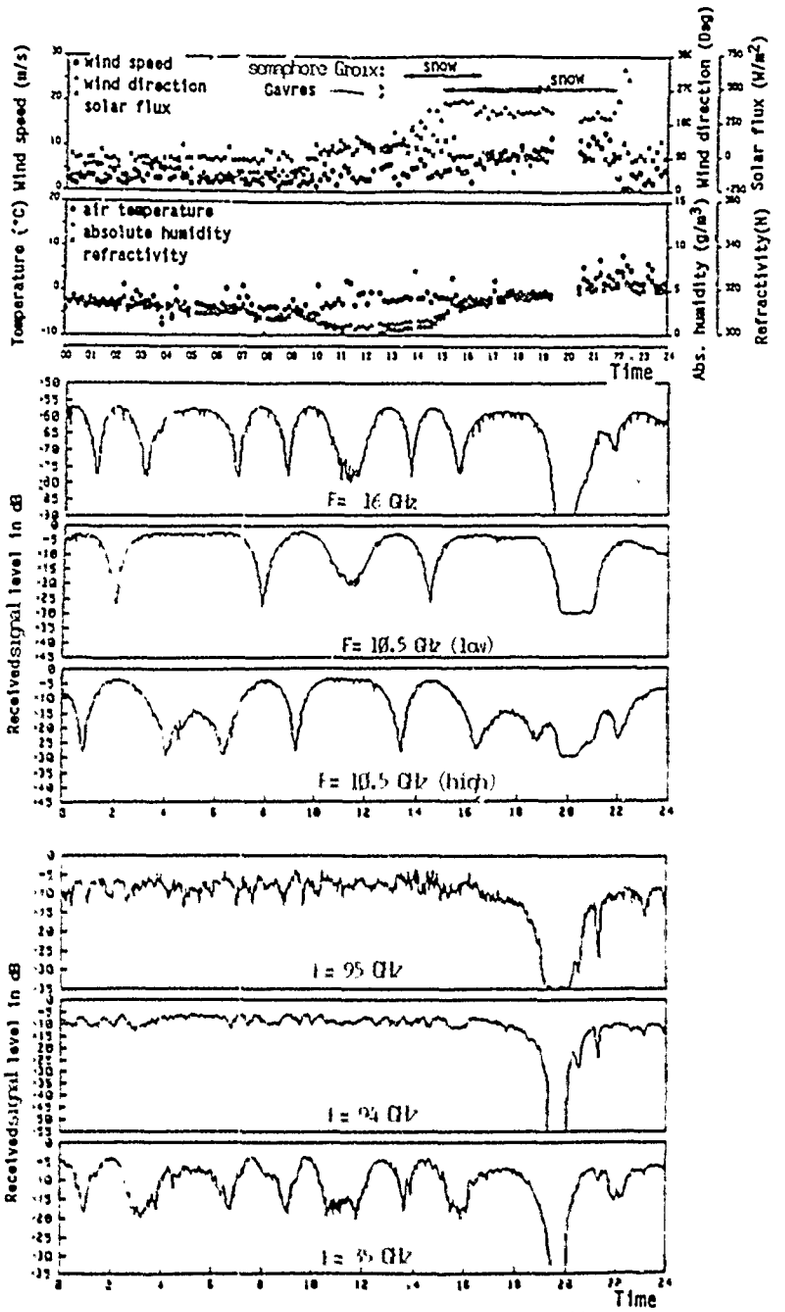

Figure 4.23: Attenuation caused by "dry", then "wet", snow
8 - 1 - 1984 at LORIENT

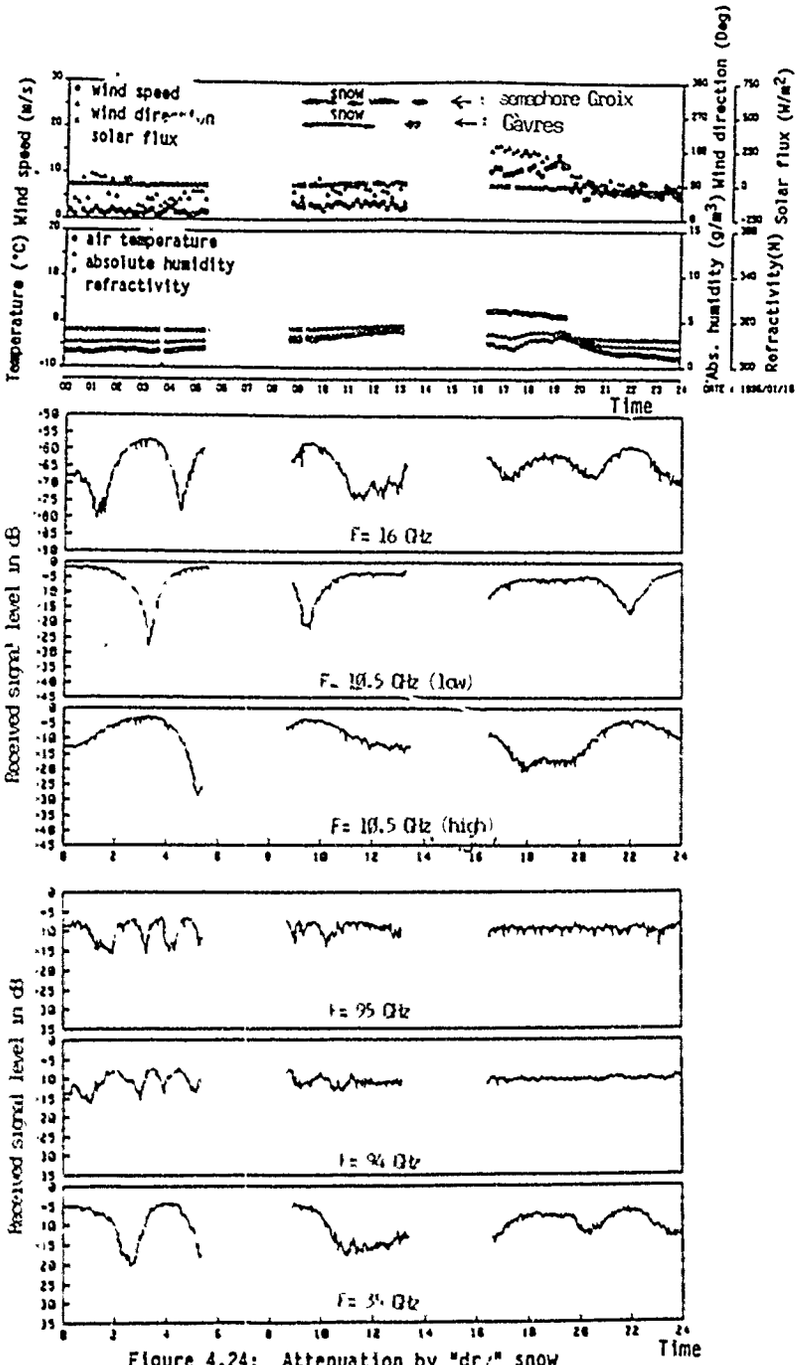

Figure 4.24: Attenuation by "dr." snow
16 - 1 - 1984 at [illegible] :ENT

(a) Incident on 8th January 1985

The presence of snow in small flakes was observed around 1500 h at the reception site. The air temperature then was below zero. Apparently this type of snow causes only very slight attenuations in the millimetre wave range (Figure 4.23). Then the air temperature tended towards zero at about 1800 h.

The wind was then blowing from the south-west.

The high attenuation (more than 20 dB) observed at all frequencies was probably due to wet snow. Its long duration (about 5 h) is noteworthy.

(b) Incident on 16th January 1985

Snow falls were observed at GAVRES and at the semaphore at Ile de GROIX between 9 h and 13 h. The air temperature was then slightly below zero, rising slightly (Figure 4.24). The light wind was north-easterly. The steady increase in the wind increased the roughness of the sea: although the interference figures at 95 GHz were clear in the morning, they tended to disappear in the evening. Interference figures could not be reconstituted because sea roughness measurements for this period were not available. In any event, attenuation by the snow was very small.

4.5 MILLIMETRE WAVE PROPAGATION IN THE LOW-LEVEL MARITIME TROPOSPHERE

4.5.1 Surface boundary layer

4.5.1.1 Qualitative description of the surface boundary layer

The layer of atmosphere lying close to the surface of the sea is called the surface boundary layer. It is the focus of air movements which are closely dependent upon weather and surface conditions. In particular, the air and water temperatures have a profound effect upon its vertical stability:

- when the air temperature (T_a) is lower than the water temperature (T_s), the boundary layer is unstable. This situation gives rise to large-scale turbulence caused by convection;
- when T_a is greater than T_s, the boundary layer is stable. It consists of turbulent movements on a smaller scale than in the previous case.

The surface boundary layer may reveal marked temperature and humidity gradients in light horizontal winds. Its depth is typically several tens of metres.

4.5.1.2 Variation in the refractive index gradient in the surface boundary layer

Vertical variation in the meteorological parameters is represented by a refractive index gradient which takes a simple form in the low-level troposphere [75]:

$$\frac{dN}{dh} = 0.35 \frac{dp}{dh} - 1.3 \frac{dT}{dh} + 7 \frac{ds}{dh}$$

where p is the pressure in mb;

T is the air temperature in °C;

s is the specific humidity (in g of water vapour per kg of dry air).

The specific humidity s is related to the partial water vapour pressure e by s=622 e/p, with p the atmospheric pressure.

In a homogeneous atmosphere, meteorological parameter variation is linear:

$$\frac{dp}{dh} = - 0.12 \text{ mb/m} < 0$$

$$\frac{dT}{dh} = - 6.5\ 10^{-3} \text{ °C/m} < 0$$

$$\frac{ds}{dh} = - 2\ 10^{-3} \text{ g/m} < 0$$

and leads to a dN/dh value close to that for the standard atmosphere.

However, the variations in the meteorological parameters (mainly temperature and humidity) are no longer linear on approaching the air-sea interface. They may cause substantial variations in the refractive index.

- Humidity variation with height

The air at the surface is saturated with water vapour, to meet continuity conditions at the sea-air interface. The relative humidity, which is 100% at zero altitude, decreases sharply over the first few metres and tends towards the ambient value. Therefore the drier the air above the surface, the more negative the humidity gradient.

- Temperature variation with height

The temperature contour is closely dependent upon the stability of the layer, and therefore upon the temperature difference between air and water. It may be very positive when the boundary layer is stable (temperature inversion). This occurs in particular with advection movement of a mass of warm air over a large area of cold sea.

When the air and water temperatures are similar (difference less than 2°C), the temperature and humidity contours are logarithmic. This is called the neutral situation.

4.5.1.3 Evaporation duct

When there is a marked decrease in humidity and/or a temperature inversion, the index gradient is strongly negative up to a certain height and then becomes positive again (Figure 4.25). This layer with a negative index gradient is called an evaporation duct.

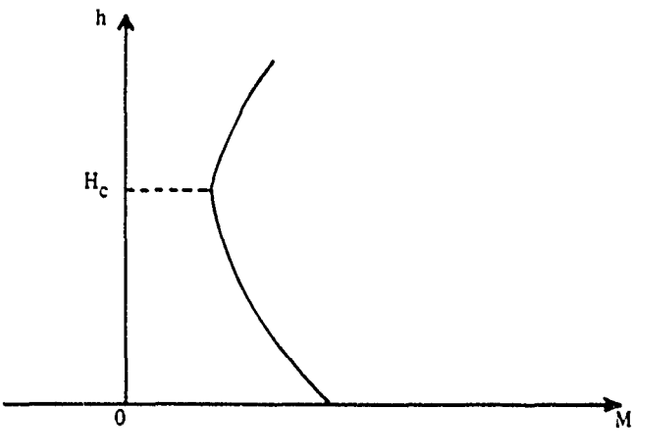

Figure 4.25: Evaporation duct of height H_c

Methods for calculating the height of the duct have been developed on the basis of thermodynamics [75]. They take account of "in situ" measurements to a large extent. This is the "BULK" method, which is regarded as the most reliable. It is of great practical value because it defines the duct on the basis of data which can be arrived at relatively easily by experiment:

- air temperature)
)
- relative humidity) at a given height h
)
- wind speed)

- water temperature at the surface (h = 0).

The depth of the evaporation duct does not exceed 40 m. Its mean value in the northern latitudes is about 8 m, whereas in the tropics it is around 30 m. Other things being equal, the higher the water temperature, the higher the duct [76], [77].

4.5.2 Millimetre wave propagation in "abnormal" atmospheric conditions

Millimetre wave propagation in the low-level maritime troposphere is particularly effected in some of the weather conditions previously referred to. The atmospheric structure may lead to channelling of energy (guidance) where the boundary layer is stable. In the opposite situation it may give rise to received signal level fluctuations which are substantial in phase and in amplitude (without signal level over-elevation).

4.5.2.1 Guidance

When the refractive index gradient is less than -79 N/km, propagation is by super-refraction; the radius of curvature of the radio path is then smaller than the curvature of the earth. Under more severe conditions (index gradient less than -157 N/km) the wave may be guided.

This guidance is possible when the incident beam attack angle is small in relation to the duct axis and when the transmission frequency is above a minimum frequency. The relationship giving the minimum frequency (cut-off frequency) as a function of duct height H_C is written as follows for a linear variation in the index gradient G (in N/km) [48]:

$$f_m \text{ (GHz)} = 3780\, G^{-1/2}\, H_C^{-3/2}$$

and is shown in Fig. 4.26.

The ducts make it possible to obtain signal levels much higher than the free space level, provided that the receiver is placed on the ray trajectory.

Wave attenuation is then inversely proportional to distance d (instead of $1/d^2$). If, however, the receiver is in a shadow zone there may also be persistent attenuations below the free space level [3].

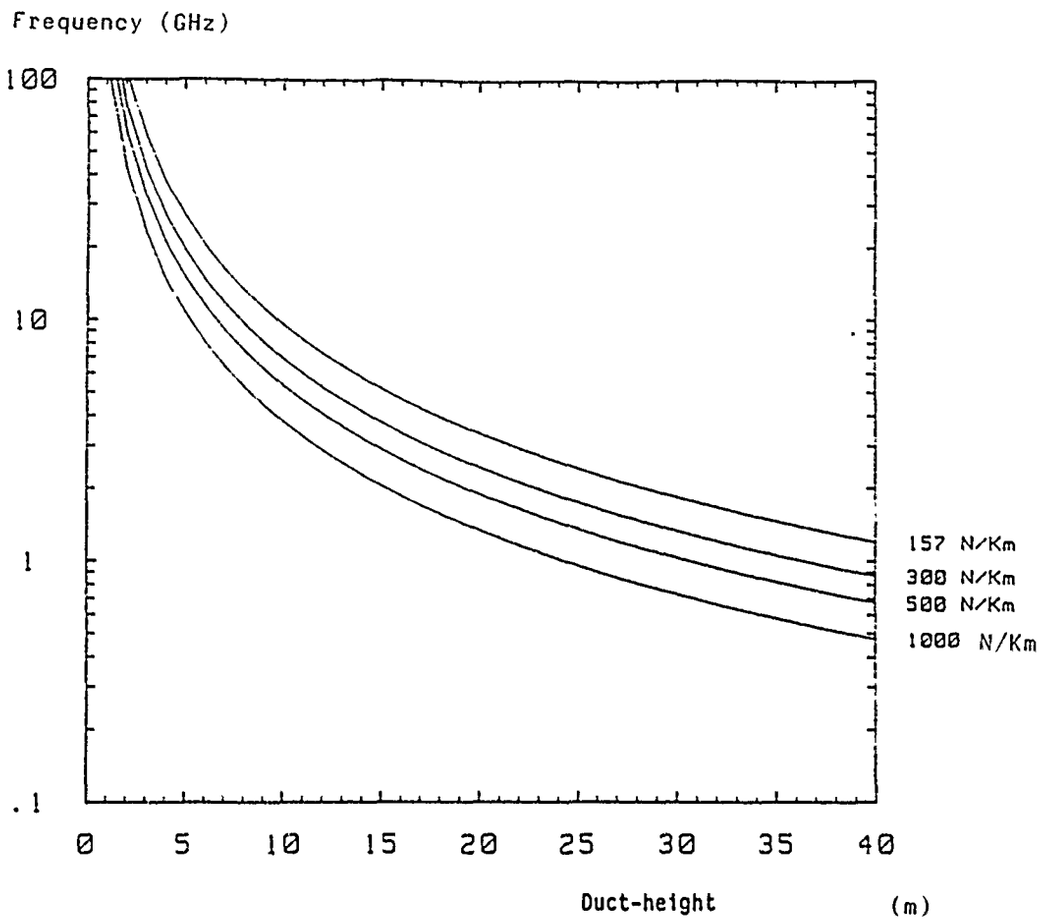

Figure 4.26: Cut-off frequency for an evaporation with a linear index gradient

4.5.2.2 Signal level fluctuations

Abnormal received signal level fluctuations caused by lack of uniformity in the refractive index of the air in space and time were observed in some experiments in a maritime atmosphere [3], [48]. This type of incident is treated at greater length by way of measurements in the next paragraph.

4.5.3 Experimental abnormal propagation data at 36 GHz

Incidents of abnormal propagation were recorded during the three measurement campaigns.

Meteorological data was supplied by two stations on either side of the link and by the buoy. Unfortunately we had no refractometer available to measure the refractive index of the air.

"Abnormal" propagation showed itself in the LORIENT experiments by:

- interference figure deformation due to the double path;
- larger amplitude scintillations.

4.5.3.1 Deformation of interference figures

Deformation of interference figures may be caused by large-scale advection movements, which alter the air refraction gradient. An additional difference in phase between the direct ray and the indirect ray variable in time is added to the nominal value.

This phenomenon is illustrated in Figure 4.27. The meteorological parameters reveal the passage of a warm humid front coming from the ocean: the air temperature rises by about 7°C in three hours, whereas the absolute humidity doubles during this period. There is a transition from an unstable situation (in which the water temperature is high relative to the air temperature) with a high duct to a neutral situation ($T_s \approx T_a$). The duct is then lower.

4.5.3.2 Signal level fluctuations with large amplitude

Short-term signal level fluctuations with large amplitude (more than 25 dB) were recorded during local changes in temperature and humidity of solar origin.

The incident on 13th October 1984 (Fig. 4.28) shows an air temperature close to its daily maximum (about 15°), a light wind (a few metres per second) and low relative humidity (60%-70%).

Similarly there are equivalent meteorological conditions for 17th August 1986, but with a higher air temperature ($\approx$25°C) (Fig. 1.11, Chapter I).

These are the meteorological conditions which induce evaporation ducts with a height of several metres. These are closely dependent upon the meteorological parameters in the vicinity of the surface. Consequently they may have widely fluctuating propagation properties causing this type of fading.

NOTE: No case of guided propagation was recorded during the three campaigns. The received signal level has always remained within the limits fixed by the double path phenomenon. For there to be any hope of observing millimetre wave guided propagation incidents, the link would have to be much lower, a few metres above the sea (see Figure 4.26).

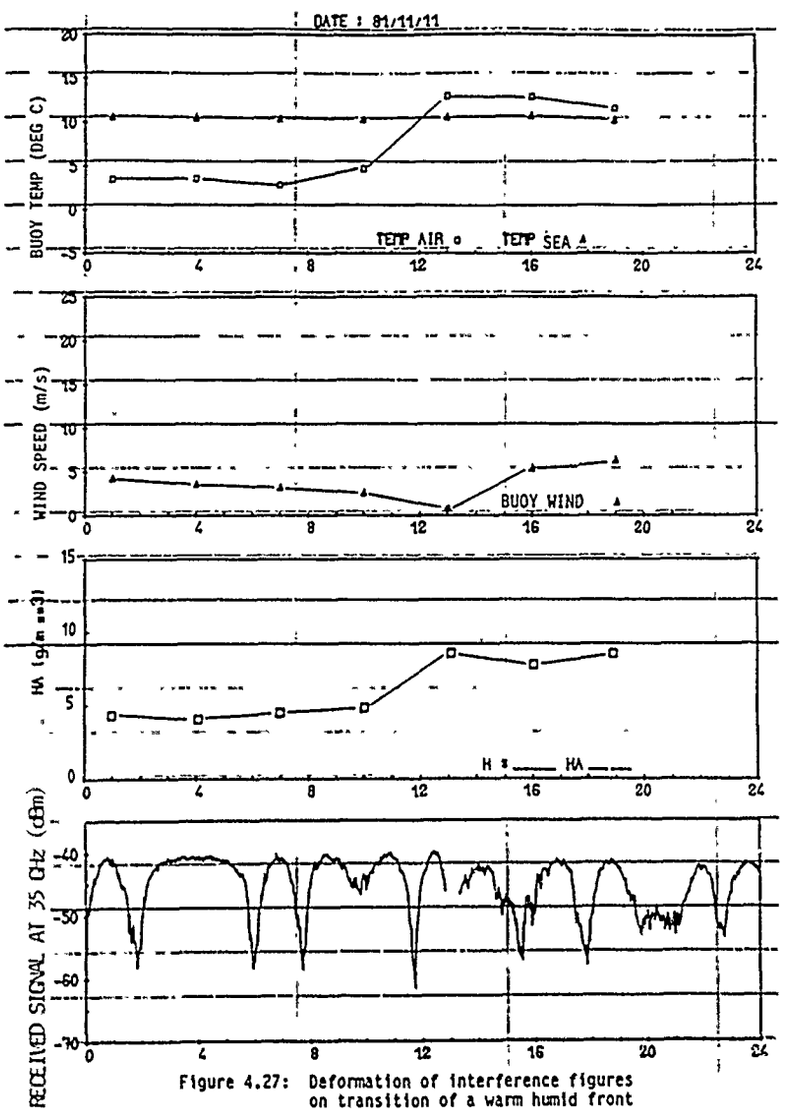

Figure 4.27: Deformation of interference figures on transition of a warm humid front

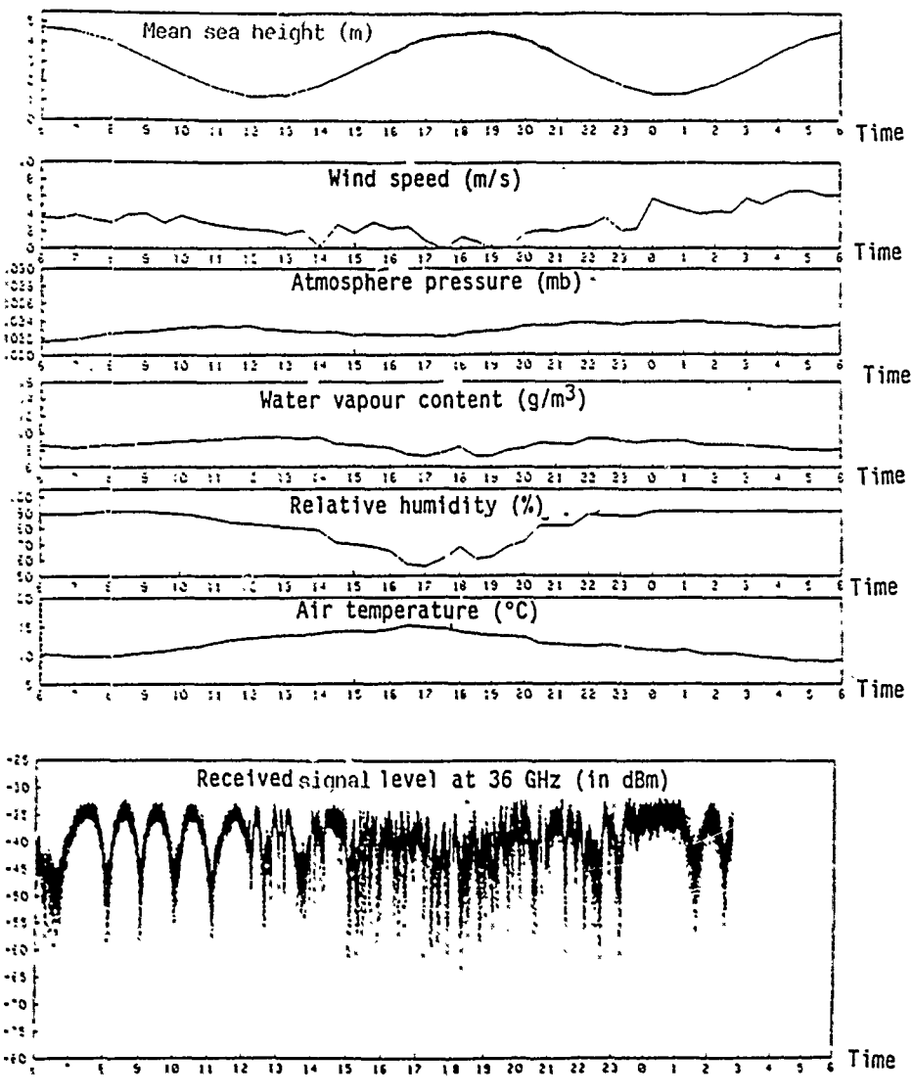

Figure 4.28: Signal level fluctuations in calm weather
13 - 10 - 1984 at LORIENT

CONCLUSIONS - PROSPECTS

This new contribution to the study of millimetre wave propagation above the sea and through hydrometeors (mainly rain) rests on a substantial experimental data base. The work was difficult, due to constant superposition of various phenomena which were difficult to separate:

- double path due to reflection of part of the incident energy on the surface of the sea;
- attenuation by rain;
- disturbances caused by atmospheric propagation.

Nevertheless, examination has yielded a detailed analysis of each of the phenomena observed, by virtue of the resources deployed throughout successive experimental campaigns and a constant search for improved quality of measurement.

Study of the surface of the sea

We sought to gain a good understanding of sea surface movements before embarking on an analysis of the effects of the maritime environment on millimetre wave propagation.

* In the presence of a sea raised by the wind (where Hl/3 > 1.5 m), height measurements Hl/3, period measurement THl/3 and wind speed were compared with expressions deduced from the PIERSON-MOSKOWITZ spectrum. The THl/3 - Hl/3 relationship is validated experimentally. On the other hand, the Hl/3 - wind speed relationship is not consistently valid, because of coast effects and the constant superposition of several wave movements.

* The hydrodynamic spectrum varies greatly in shape according to past or present meteorological situations. It is then clearly apparent that the period THl/3, often supplied by swell sensors, is not necessarily representative of surface periodicity. It should therefore be used with care, particularly for interpretation of propagation phenomena.

* The probability distribution of fluctuations in instantaneous sea levels tends towards a normal distribution.

Then we examined the effects of the sea surface on millimetre-wave propagation by an analysis of short-term signal level fluctuations, followed by an analysis of long-term fluctuations.

Short-term fluctuations

* Statistical analysis of short-term fluctuations shows that these have something in common with a RICE distribution.

These fluctuations tend towards a RAYLEIGH distribution with a calm sea and on the signal minima, whereas when the sea is rough the probability distribution becomes Gaussian in appearance.

* Spectral analysis proves that the received signal is particularly affected by low-frequency movements in the hydrodynamic spectrum. On the other hand, short-term movements due to wind action appear to be "filtered".

When the sea is rough, the signal spectrum resembles a Gaussian noise spectrum occupying the entire band.

Long-term fluctuations

This type of fluctuation is due to the coherent composition of the direct and reflected fields. Analysis of these made it possible to calculate the coherent forward coefficient on the basis of measurements made at fixed heights and measurements collected via a mobile-height system simulating the tide.

Taking measurement uncertainties into account, it is noteworthy that there is good agreement between these measurement points and the expression of MILLER et al. Taking the view that propagation takes place in an atmosphere with a constant index gradient, we developed a model deduced from this formulation. It accurately reproduces long-term variations in the signal received.

Work on signal level fluctuations can be continued along two lines:

* Experimental

The incoherent forward reflection coefficient can be calculated on the assumption of a RICE probability distribution for a certain number of incidents in which it is certain that the signal level fluctuations are essentially due to the sea.

* Theoretical

It would be interesting to develop a theoretical model supplying received signal statistical amplitude and phase characteristics as a function of link geometry and sea surface statistical characteristics. This complex problem, which resorts to several theories (perturbation method, geometrical optics) has not been entirely solved in the millimetre wave range and with low incidences, due to superposition of several roughness scales (gravity waves, capillary waves).

The atmosphere may also cause severe deterioration in link quality in the wave band studied. Millimetre waves are particularly sensitive to rain and to the atmospheric structure.

Attenuation by rain and other hydrometeors

Detailed study of attenuation by rain was possible because we had a spectropluviometer measuring raindrop size distribution. Overall these distributions match those proposed by MARSHALL-PALMER and JOSS et al.

Overall attenuation on the link was calculated on the basis of these data using the MIE theory and the assumption of a uniform rain cell. It was then compared with the measured attenuation deduced from the received signal levels. Considering the length of the link and the presence of a double path, prediction of attenuation by rain as a percentage of time on the basis of rain gauge data alone seemed to be satisfactory.

Other hydrometeors (snow, fog) have little effect upon millimetre-wave propagation. They give rise only to slight attenuations which are difficult to express in figures because the double path phenomenon is present. Nevertheless we observe that "wet" snow causes much greater attenuation than "dry" snow.

Non-standard propagation

The inteference figures recorded in standard conditions are deformed or even destroyed in the presence of peculiar atmospheric structures. High-amplitude short-term fluctuations (during wind-free and sunny periods) are then observed, revealing the probable presence of evaporation ducts several metres in height.

No incident of guided propagation was observed, because of too great an antenna height.

Studies of millimetre wave propagation in the surface boundary layer will have to be completed in future. A more precise definition of the phenomena linked to the air-sea interface seems to be essential for this purpose. Measurements of:

- refraction;
- atmospheric turbulence (using probes with a very short response time);
- wave fronts;

should be made jointly.

Simply setting up a single link operating at a fixed frequency is sometimes insufficient to ensure the rate of operation desired for applications in the field of telecommunications. Various techniques such as space and frequency agility or changing the direction of the antennas can then be used successfully to reduce severe attenuation due to the double path or to atmospheric fluctuations.

REFERENCES

[1] C. I. BEARD et I. KATZ : *«The dependance of microwaves radio signal spectra on roughness and waves spectra»*, IRE TRANS. ON ANTENNAS AND PROPAGATION, Vol. AP-5, pp. 183-191, April 1957

[2] C. I. BEARD : *«Coherent and incoherent scattering of microwaves from the ocean»*, IRE TRANS. ON ANTENNAS AND PROPAGATION, Vol. AP-9, pp. 470-483, Sept 1956

[3] A. J. MONDLOCH : *«Overwater propagation of millimeter waves»*, IEEE TRANS. ON ANTENNAS AND PROPAGATION, Vol. AP-17, pp. 82-85, Jan. 1969

[4] J. A. VIGNALI : *«Overwater line-of-sight fade and diversity measurements at 37 GHz»*, IEEE TRANS. ON ANTENNAS AND PROPAGATION, Vol. AP-18, pp. 463-471, July 1970

[5] R.J. SHERWELL : *«Measurements of effective sea reflectivity and attenuation due to rain at 81 GHz»*, AGARD CONFERENCE PROCEEDINGS N° 245, pp. 45.1-45.5, Sept. 1978

[6] V. KLAUS : *«Cahier marisonde n° 13 étude sur la période d'oscillation des marisondes H»*, Note technique de l'établissement d'étude et de recherches météorologiques n° 92, Nouvelle série, Fév. 1981

[7] P. QUINTY : *«Définition d'un algorithme permettant, à partir des données accélérométriques, le calcul de deux paramètres significatifs de houle et d'un capteur embarcable utilisant cet algorithme»*, Thèse de doctorat de 3ème cycle, Université Pierre et Marie Curie, Paris VI, 1983

[8] ..... : Note technique concernant la description de la bouée «WAVERIDER»

[9] A. JUNCHAT, J.F. KERDRAON : *«Dépouillement d'une campagne d'étude de la propagation des ondes millimétriques en ambiance marine»*, Rapport d'essai n° SRE. 65105, CELAR, Avril 1985

[10] D. HAUSER, P. AMAYENC, B. NUTTEN, P. WALDTEUFEUL : *« A new optical instrument for simultaneous measurement of raindrop diameter and fall speed distributions»*, JOURNAL OF ATMOSPHERIC AND OCEANIC TECHNOLOGY, Vol. 1, Sept. 1984

[11] V. KLAUS :« *Etude d'un spectropluviomètre photoélectrique fournissant en temps réel des paramètres intégrés*», Thèse de doctorat de 3ème cycle, Université de Paris VI, Fév. 1976

[12] ..... : Brochure technique de THOMSON-CSF concernant le faisceau hertzien TFH 720

[13] J.P. DEHAENE : «*Faisceau hertzien millimétrique*», AGARD CONFERENCE PROCEEDINGS N° 245, pp. 4.1-4.13, Sept. 1978

[14] H. LACOMBE : «*Cours d'océanographie physique*», Edition GAUTHIER-VILLARD, Paris 1965

[15] L.F. TITOV : «*Wind driven waves*», Israel programme for scientific translations, Jérusalem 1971

[16] W.J. PIERSON, L. MOSKOWITZ : «*A proposal spectral form for fully developed wind seas based on the simularity theory of S.A.*», JOURNAL OF GEOPHYSICAL RESEARCH, Vol. 69, n° 24, pp. 5181-5190, 1964

[17] O.M. PHILLIPS : «*Dynamics of the upper ocean*», CAMBRIDGE UNIVERSITY PRESS, Londres, pp. 109-119, 1966

[18] K. HASSELMANN, D.B. ROSS, P. MULLER, W. SELL : «*A parametric wave prediction model*», JOURNAL OF PHYSICAL OCEANOGRAPHIY N° 6, pp. 200-228, 1976

[19] D.E. BARRICK : «*Remote sensing of sea state by radar*», REMOTE SENSING OF THE TROPOSHERE, Edition V. DERR, U.S. govt. printing office, Washington, pp. 12.1-12.45, 1972

[20] R. BONNEFILLE : «*Hydraulique maritime*», Chapitre 4, 1976

[21] D. GUNTER : «*General oceanography*», Interscience publishers JOHN WILLY, New-York, Londres, 1963

[22] P. GROEN : «*The waters of the sea*», VAN NOSTRAND CO., Londres, 1967

[23] F. GERARD : «*La houle théorie et prévision*», METEOROLOGIE MARITIME N° 117, Oct. 1982

[24] G.R. VALENZUELA : «*Scattering of electromagnetic waves from the ocean*», Surveillance of environmental pollution and resources by electromagnetic waves, pp. 199-226, 1978

[25] M. FOURNIER : *«Trajets multiples sur la surface de la mer»*, AGARD CONFERENCE PROCEEDINGS N° 345, pp. 24.1-24.16, 1983

[26] S.O. RICE : *«Reflection of electromagnetic waves from slightly rough surfaces»*, COMM. PURE APPL. MATH., Vol. 4, pp. 361-378, Feb.-March 1951

[27] G.R. VALENZUELA : *«Scattering of electromagnetic waves for a tilted rough surfaces»*, RADIO SCIENCE, Vol. 3, n° 11, pp. 1057-1066, Nov. 1968

[28] G.R. VALENZUELA : *«The effective reflection coefficients in forward scatter from a dielctric slightly rough surface»*, PROCEEDINGS OF THE IEEE, Vol. 58, n° 8, pp. 1279, Aug. 1970

[29] D.E. BARRICK : *«Theory of HF and VHF propagation across the rough sea 2, applications to HF and VHF propagation above ' «a»*, RADIO SCIENCE, Vol. 6, pp. 527-533, May 1971

[30] J.W. WRIGHT : *«Backscattering from capillary waves with application to sea clutter»*, TRANS. ON ANTENNAS AND PROPAGATION, Vol. AP-14, n° 6, pp. 749-754, Nov. 1966

[31] A. ISHIMARU : *«Wave propagation and scattering in ramdon media»*, ACADEMIC PRESS, New-York, San Fransisco, Londres, Vol. 2, 1978

[32] P. BROCHE, J.C. DE MAISTRE, P. FORGET : *«Mesure par radar décamétrique cohérent des courants superficiels engendrés par le vent»*, OCEANOLOGICA ACTA, Vol. 6, n° 1, pp. 43-53, 1983

[33] E. AUGROS, C. LEGLANTIER : *«Le radar à diffusion ionosphérique et la mesure des paramètres météo-océaniques»*, la METEOROLOGIE

[34] W S. AMENT : *«Toward a theory of reflection by a rough surface»*, PROCEEDINGS OF THE IRE, n° 41, pp. 142-146, 1953

[35] P. BECKMAN, A. SPIZZICHINO : *«The scattering of electromagnetic waves from rough surfaces»*, PERGAMON PRESS, 1963

[36] R.D. KODIS : *«A note on the theory of scattering from a irregular surface»*, IEEE TRANS. ON ANTENNAS AND PROPAGATION, Vol. AP-14, n° 1, pp. 77-82, Jan. 1966

[37] D.E. BARRICK . *«Rough surface scattering based on the specular point theory»*, IEEE TRANS. ON ANTENNAS AND PROPAGATION, Vol. AP-16, n° 4, pp. 449-454, July 1968

[38] Y. KARASAWA, T. SHIOKAWA : *«Characteristics of L-Band multipath fading due to sea surface reflection»*, IEEE TRANS. ON ANTENNAS AND PROPAGATION, Vol. AP-32, n° 4, pp. 618-623, June 1984

[39] C.I. BEARD : *«Remote sensing of ocean significant waves height by forward scattering examples from L-Band data»*, NRL MEMORAMDUM REPORT 3968, Naval Research Laboratory, Washington D.C., April 1979

[40] J.W. WRIGHT : *«A new model for sea clutter»*, IEEE TRANS. ON ANTENNAS AND PROPAGATION, Vol. AP-16, n° 2, pp. 217-223, March 1970

[41] N.W. GUINARD : *«Experimental study of a sea clutter model»*, PROCEEDING OF THE IEEE, Vol. 58, n° 4, pp. 543-550, April 1970

[42] F.G. BASS, I.M. FUCKS, A.I. KALMYKOV, I.E. OSTROVSKY, A.D. ROSENBERG : *«Very high frequency radiowaves scattering by a disturbed sea surface»*, IEEE TRANS. ON ANTENNAS AND PROPAGATION, Vol. AP-16, n° 5, pp. 560-568, Sept. 1968

[43] G.S. BROWN : *«Backscattering from a gaussian distributed perfectly conducting rough surface»*, IEEE TRANS. ON ANTENNAS AND PROPAGATION, Vol. AP-26, n° 3, pp. 472-482, May 1978

[44] R.K. MOORE : *«Radar determination of winds at sea»*, PROCEEDINGS OF THE IEEE, Vol. 67, n° 11, pp. 1504-1521, Nov. 1979

[45] A.K. FUNG, K.K. LEE : *«A semi-empirical sea-spectrum model for scattering coefficient estimation»*, IEEE JOURNAL OF OCEANIC ENGINEERING, Vol. OE-7, n° 4, pp. 166-176, Oct. 1982

[46] L. BOITHIAS : *«Propagation des ondes radioélectriques dans l'environnement terrestre»*, COLLECTION TECHNIQUE ET SCIENTIFIQUE DES TELECOMMUNICATIONS, DUNOD, Paris, 1983

[47] Y. HURTAUD : *«Contribution à l'étude, l'analyse et la modélisation de la propagation des ondes millimétriques en ambiance maritime et à travers les hydrométéores»*, 1er COMPTE-RENDU ANNUEL, Convention n° 0114184 entre l'UNIVERSITE DE RENNES I ET LE CELAR, Avril 1985

[48] D.E. KERR : *«Propagation of short radio waves»*, DOVER PUBLICATIONS, INC, 1965

[49] A. R. MILLER, R.M. BROWN, E. VEGH : *«New derivations of the rough surface reflection and for the distribution of the sea-waves elevations»*, IEE PROCEEDINGS, Vol. 131, Pt. H, n° 2, pp. 114-115, April 1984

[50] C.C.I.R. : AVIS 310-5, Volume 5 : «PROPAGATION DANS LES MILIEUX NON IONISES»

[51] M. MOREAU, A. MATHIEU : *«Statistiques appliquées à l'expérimentation»*, Editions EYROLLES, Paris, 1979

[52] M.L. JOHNSON, S. KOTZ : *«Continuous univariate distributions-1»* JOHN WILEY, Chp. 12, New-York, Chischester, Brisbane, Toronto, 1970

[53] C.C.I.R. : *«Affaiblissement par les gaz dans l'atmosphère»*, Rapport 719-1, Vol. 5, «PROPAGATION DANS LES MILIEUX NON IONISES»

[54] J.L. LANE : *«Propagation factors in relation to application in the frequency range 30 - 200 GHz»*, Aug. 1978

[55] T. OGUCHI, Y. HOSOYA : *«Scattering proprieties of oblate raindrops and cross-polarisation of radio waves due to rain (part 2). Calculations at microwaves and millimeter regions»*, JOURNAL OF THE RADIO RESEARCH LABORATORIES, Vol. 21, n° 105, pp. 191-259, 1974

[56] J.F. EBERSOLE : *«Effects of hydrometeors on electromagnetic waves propagation»*, AFGL-TR-84-0318, AIR FORCE GEOPHYSICS LABORATORY, Jan. 1974

[57] J.P. MON, N. SPANJAARD : *«La Propagation des ondes millimétriques sur les trajets terre-espace»*, ECHO DES RECHERCHES, pp. 49-55, Jui. 1981

[58] G. MIE : *«Bertrage zu optik truber Medien, speziell kolloidaler Metallosungen»*, annalen der physik, n° 3, 1908

[59] J.A. STRATTON : *«Théorie de l'électromagnétisme»*, DUNOD, Paris, 1961

[60] J.C. VAN DER HULST : *«Light scattering by small particules»*, JOHN WILLY, New-York, 1957

[61] M. KERKER : *«The scattering of light»*, ACADEMIC PRESS, New-York, Londres, 1969

[62] M. BORN, E. WOLF : *«Principles of optics»*, PERGAMON PRESS, 1975

[63] P.S. RAY : *«Broadband complex refractive indices of ice and water»*, APPLIED OPTICS, Vol. 11, n° 8, Août 1972

[64] J.O. LAWS, D.A. PARSONS : *«The relation of raindrop-size to intensity»*, TRANS. AMER. GEOPHYS. UNION, Vol. 24, pp. 452-460, 1943

[65] J.S. MARSHALL, W.M.C.K. PALMER : *«The distribution of raindrops with size»*, J. METEOR., Vol. 5, pp. 165-166, Aug. 1948

[66] J. JOSS, J.C. THAMS, A. WALDVOGEL : *«The variation of raindrop size distribution at Locarno»*, PROC. INT. CONF. CLOUD PHYSICS, pp. 352-373, 1968

[67] K.L.S. GUNN, T.W.R. EAST : *«The microwaves proprieties of precipitation particles»*, QUART. J.R. METEOROL. SOC., Vol. 80, n° 3, pp. 352-545, 1954

[68] R.L. OLSEN, D.V. ROGERS, D.B. HODGE : *«The aR^b relation in the calculation of rain attenuation»*, IEEE TRANS. ON ANTENNAS AND PROPAGATION, Vol. AP-26, n° 2, pp. 318-329, March 1978

[69] D.C. HOGG : *«Intensity and extent of rain on earth-space paths»*, NATURE, n° 243, pp. 377-388, 1973

[70] T. IHARA, Y. FUHUHAMA : *«Frequency scaling of rain attenuation at centimeter and millimeter waves using a path-averaged drop size distribution»*, RADIO SCIENCE, Vol. 16, n° 6, pp. 1365-1372, Nov.-Déc. 1981

[71] C.C.I.R. : *«Données statistiques sur la durée des chutes de pluie»*, RAPPORT 563-2, Vol. 5, «PROPAGATION DANS LES MILIEUX NON IONISES»

[72] E. ALTSHULER : *«Millimeter wave propagation handbook»*, DOCUMENT AC/243-D/916/AC/243/PANEL III/D/220, Mai 1984

[73] K.L. KOESTER, L. KOSOWSKY, J.F. SPARACIO : *«Millimeter waves propagation»*, appendice à «MILLIMETER WAVES RADAR APPLICATIONS TO WEAPONS SYSTEMS», de V.L. RICHARD

[74] H.B. WALLACE : *Millimeter wave propagation measurements at the* Ballistic Research Laboratory», OPTICAL ENGINEERINC, Vol. 22, n° 1, Jan.-Fév. 1983

[75] P. SCHIMTZ : *Détermination numérique de la hauteur du conduit d'évaporation»*, DOCUMENT METEOROLOGIQUE NATIONALE, Mai 1985

[76] J.H. RICHTER : *«Review of recent developments in evaporation ducting* assessments», AGARD CONFERENCE PROCEEDINGS N° 407, pp. 11.1-11.8, Oct. 1986

[77] H.V. HITNEY, J.H. RICHTER, R.A. PAPPERT, K.D. ANDERSON, G.B. BAUMGARTNER : *«Tropcspheric radio assessement»*, PROCEEDINGS OF THE IEEE, Vol. 73, n° 2, Feb. 1985

BIBLIOGRAPHY

L.R. WHICKER, D.C. WEBB : *«The potential milltary applications of millimeter waves»*, AGARD CONFERENCE PROCEEDINGS N° 245, pp. 1.1 - 1.16, 1978

S.L. JOHNSON : *«Millimeter radar»*, MICROWAVES JOURNAL, pp. 16.28, Nov. 1977

K.E. FICHER : *«Atmospheric influences on the millimeter and submillimeter waves propagation»*, AGARD CONFERENCE PROCEEDINGS N° 245, pp. 42.1 - 42.5, Nov. 1978

D. ROTHER, E. MULLER : *«MM-waves propagation and applications in military communications systems»*, AGARD CONFERENCE PROCEEDINGS N° 407, pp. 16.1 - 16.20, Oct. 1986

Y.K. WU, C.P. TRESSELT : *«MM-radar for highway collision avoidance»*, MICROWAVE JOURNAL, pp. 39-42, Nov. 1977

S. OHMORI, A. IRIMATA, H. MORIKAWA, K. KONDO, Y. HASE, S. MIURA : *«Characteristics of sea fading in maritime satellite communications»*, IEEE TRANS. ON ANTENNAS AND PROPAGATION, Vol. AP-33, n° 8, Aug. 1985

R. MAKARUSCHKA, H.H. FUCHS : *«Propagation measurements at 94 GHz in a maritime environment»*, AGARD CONFERENCE PROCEEDINGS N° 345, pp. 36.1 - 36.10

C.I. BEARD, I. KATZ : *«Phenomenological vector model of microwave reflection from the ocean»*, IRE TRANS. ON ANTENNAS AND PROPAGATION, Vol. AP-4, pp. 162-167, April 1956

A.W. STAITON, C.W. TOLBERT : *«Measurement and analysis of instantaneous radio height-gain curves at 8.6 millimeters over rough surfaces»*, IRE TRANS. ON ANTENNAS AND PROPAGATION, Vol. AP-4, pp. 346-351, July 1956

A.H. LAGRONE, A.W. STRAITON, H.W. SMITH : *«Synthesis of radio signals on overwater paths»*, IRE TRANS. ON ANTENNAS AND PROPAGATION, Vol. AP-3, pp. 48-52, April 1955

J. SNIEDER : *«Survey of NATO propagation compaigns in Lorient, France, during winter 1981/1982 and winter 1984/1985 over a 10 km path over sea in the frequency range 10-94 GHz»*, AGARD CONFERENCE PROCEEDINGS N° 407, OTTAWA, Oct. 1986

R. MAKARUSCHKA : *«Millimetre - and centimetre - waves attenuation statistics over a 9.7 km line-of-sight oversea path»*, AGARD CONFERENCE PROCEEDINGS N° 407, OTTAWA, pp. 27.1-27.10, Oct. 1986

W.P.M.N. KEIZER : *«Low-level propagation over sea : the Lorient experiment 1981-1982, Part 1»*, Report n° 1985-82, PHYSICS AND ELECTRONICS LABORATORY TNO, Oct. 1985

W.P.M.N. KEIZER . *«Specular reflection characteristics of the sea at 16 GHz»*, Report n° FEL 1986-30, PHYSICS AND ELECTRONICS LABORATORY TNO, May 1986

V.J. FALCOME, L.W. ABREU, E.P. SHETTLE : *«Effects of hydrometeors on electromagnetic waves propagation»*, Report n° AFGL-TR-84-0318 AIR FORCE GEOPHYSICS LABORATORY, June 1985

R.G. MEDHURST : *«Rainfall attenuation of centimeter waves : comparison and measurement»*, IEEE TRANS. ON ANTENNAS AND PROPAGATION, Vol. AP-13, n° 4, pp. 550-564, July 1965

J. SANDER : *«Rain attenuation of millimeter waves at 5.77, 3.3, and 2 mm»*, IEEE TRANS. ON ANTENNAS AND PROPAGATION, Vol. AP-23, n° 2, pp. 213-220, March 1975

H. KEIZER, J. SNIEDER, C.D. HAAN : *«Rain attenuation measurements at 94 GHz . comparison of theory with experiment»*, AGARD CONFERENCE PROCEEDINGS N° 245, pp. 44.1 - 44.10, Sept. 1978

M.M. KHARADLY, J.D. McNICOL, J.B. PETERS : *«Measurement of attenuation due to rain at 74 GHz»*, AGARD CONFERENCE PROCEEDINGS N° 245, pp. 46.1 - 46.16, Sept. 1978

F.C. MEDEIROS FILHO, R.S. COLE, A.D. SARMA : *«Millimetre-wave rain induced attenuation . theory and experiment»*, IEE PROCEEDINGS, Vol. 133, Pt. H, n° 4, pp. 308-314, Aug. 1986

K.L. HO, N.D. MAVROKOUKOULAKIS, C.K. COLE : *«Propagation studies on a line-of-sight microwaves link at 36 GHz and 110 GHz»*, MICROWAVES OPTICS AND ACOUSTICS, Vol. 3, n° 3, May 1979

B. STRAUSS : *«Evaluation de la hauteur du conduit d'évaporation»*, AGARD CONFERENCE PROCEEDINGS N° 346, STAPIND, pp. 20.1 - 20.8, Oct. 1983

K.D. ANDERSON, J.H. RICHTER, H.V. HITNEY : *«Troposheric propagation assessment»*, AGARD CONFERENCE PROCEEDINGS N° 346, STAPIND, pp. 23.1 - 23.6, Oct. 1983

J.B. KNORR : *«Guide EM waves with atmospheric ducts»*, MICROWAVES & RF, pp. 67-70, May 1985

H. KO : *«A pratical guide to anomalous propagation, Part I»*, MICROWAVES & RF, pp. 71-76, April 1985

H. KO : *«Don't let ducting clutter system specs, Part II»*, MICROWAVES & RF, pp. 103-108, June 1985

J.F. DIOURIS . *«Étude multifréquentielle de l'atténuation par la pluie des ondes millimétriques»*. Convention n° 0114/84 entre l'UNIVERSITÉ DE RENNES I et le CELAR, Juillet 1987.

Y. HURTAUD et A. JUNCHAT : *«Une campagne de propagation en milieu maritime utilisant un système numérique à 36 GHz»*. AGARD CONFERENCE PROCEEDINGS N° 407, pp. 30.1 - 30.14, Octobre 1986.

Y. HURTAUD, A. JUNCHAT et J.F. KERDRAON : *«The effects of sea surface on low level propagation at 36 GHz»*. AGARD CONFERENCE PROCEEDINGS N° 407, pp. 31.1 - 31.11, Octobre 1986.

Y. HURTAUD, C. TERRET, J.P. DANIEL et A. JUNCHAT : *«Étude expérimentale et modélisation du phenomene de reflexion sur la mer à 36 GHz»*, 40 th AGARD Meeting of the ELECTROMAGNETIC WAVE PROPAGATION PANEL . *«Diffusion et propagation dans un milieu aléatoire»*, pp. 26.1 - 26.14, Rome, Mai 1987.

ANTENNA HEIGHTS FOR THE VARIOUS
MEASUREMENT CAMPAIGNS AT LORIENT

Measurement campaign 1981-1982

	Transmission height/ level 0	Reception height/ level 0	Mean angle of incidence on the sea
94 GHz	18.7 m	12.7 m	0.15°
95 GHz	18.6 m	12.7 m	0.15°

Supervised measurement campaign October 1984

	Transmission height/ level 0	Reception height/ level 0	Mean angle of incidence on the sea
10.5 GHz	47.8	9.8 m ↔ 14.5 m	0.33°
16 GHz	47.3	9.6 m ↔ 14.3 m	0.31°
35 GHz	18.8	10.8 m ↔ 15.5 m	0.16°
94 GHz	17.8	9.8 m ↔ 14.5 m	0.14°
95 GHz	17.5	9.6 m ↔ 14.3 m	0.14°

Unsupervised measurement campaign 1984-1985

	Transmission height/ level 0	Reception height/ level 0	Mean angle of incidence on the sea
10.5 GHz	47.8	14.4 m (*) 12.7 m	0.33° 0.32°
16 GHz	47.3	12.5 m	0.32°
35 GHz	18.8	13.7 m	0.16°
94 GHz	17.8	12.7 m	0.15°
95 GHz	17.5	12.3 m	0.15°

Supervised measurement campaign August 1986

	Transmission height/ level 0	Reception height/ level 0	Mean angle of incidence on the sea
10.5 GHz	47.8	9.8 m↔14.5 m	0.33°
35 GHz	18.8	10.8 m↔15.5 m	0.16°
94 GHz	17.8	11.5 m↔16.2 m	0.15°
95 GHz	17.5	9.6 m↔14.3 m	0.14°

(*) Two supervised receivers.

FREE SPACE LEVEL CALCULATION FOR THE SYSTEM OPERATING AT 36 GHz ON THE GROIX-GAVRES LINK

The transmitter and receiver have identical gains $G = 10 \log_{10} g = 42$ dB. The transmitted power P_e is 50 mW.

The received power at distance d = 9,700 m is obtained by the following expression:

$$P_r = \frac{P_e G_e G_r \lambda^2}{16 \pi^2 d^2} \quad (A1)$$

where λ is the wavelength: $\lambda = 3 \cdot 10^8 / f = 8.33 \times 10^{-3}$ m.

Expression A1 takes the form (A2) when the powers are expressed in dBm.

$$P_r \text{ (dBm)} = 10 \log_{10} P_r \text{ (mW)}$$

$$= 10 \log_{10} g_e + 10 \log_{10} g_r - 10 \log_{10} 16\pi^2 + 20 \log_{10} \lambda - 20 \log_{10} d$$

$$P_r \text{ (dBm)} = P_e \text{ (dBm)} + G_e + G_r - A_0$$

with $A_0 = -20 \log_{10} \frac{C}{4\pi} + 20 \log_{10} f + 20 \log_{10} d$

$$= 20 \left[- \log_{10} \frac{C}{4\pi} + \log_{10} d \text{ (km)} + \log_{10} f \text{ (GHz)} \right] + 12$$

$$= 143.30 \text{ dB}$$

Since P_e (dBm) = 10 log 50 = 16.99.

The nominal received power is obtained thus:

$$P_r = 2 \times 42 + 16.99 - 143.30$$

$$P_r = -42.30 \text{ dBm}.$$

The received power is at a maximum when the direct and reflected fields are in phase.

$$P_M = -42.30 + 6 = -36.30 \text{ dBm}$$

RICE DISTRIBUTION

Let $\vec{E} = \vec{C} + \vec{A}$ be the sum of a deterministic signal $(\vec{C})$ and a random signal $(\vec{A})$, the projection of which onto two orthogonal axes are centred Gaussian distributions with the same standard deviation σ (Figure 1). Let us seek the probability distribution of amplitude E of the overall vector.

Let X and Y be its rectangular co-ordinates. The joint probability density of X and Y is written as follows:

$$p(X,Y) = \frac{1}{2\pi\sigma^2} \exp -\left[\frac{(X-C)^2 + Y^2}{2\sigma^2}\right]$$

Let us express p (X,Y) dX dY in polar co-ordinates:

$$X = C + A\cos\theta = E\cos\varphi$$
$$Y = A\sin\theta = E\sin\varphi$$

In calculating the Jacobian, we have $dX\,dY = E\,dE\,d\varphi$

and $$p(X,Y)\,dX dY = \frac{E}{2\pi\sigma^2} \exp\left[-\frac{E^2 + C^2 + 2EC\cos\varphi}{2\sigma^2}\right] dE\,d\varphi$$

The probability distribution of E is obtained by integrating on φ

$$p(E)\,dE = \frac{1}{2\pi\sigma^2}\int_{-\pi}^{\pi} \exp\left[-\frac{E^2 + C^2 + 2EC\cos\varphi}{2\sigma^2}\right] E\,d\varphi\,dE$$

$$= \frac{E}{2\pi\sigma^2} \exp -\frac{E^2 + C^2}{2\sigma^2}\int_{-\pi}^{\pi} \exp\left[-\frac{EC\cos\varphi}{\sigma^2}\right] d\varphi\,dE$$

$$\int_0^{\pi} \exp(u\cos\varphi)\,d\varphi = \pi\, I_0(u) \quad \text{et} \quad \int_{-\pi}^{\pi} = 2\int_0^{\pi}$$

$$p(E) = \frac{E}{\sigma^2} \exp\left[-\frac{E^2 + C^2}{2\sigma^2}\right] \cdot I_0\left(\frac{E.C}{\sigma^2}\right)$$

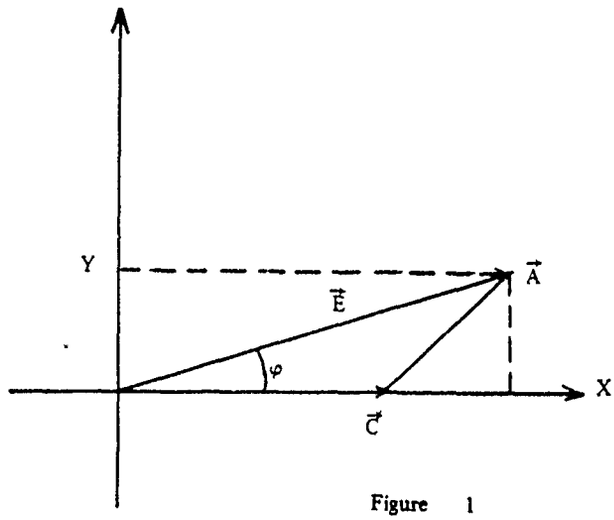

Figure 1

EXPRESSION FOR THE RICE DISTRIBUTION IN TERMS OF POWER ON THE BASIS OF THE EXPRESSION IN TERMS OF AMPLITUDE

The Rice distribution is written as follows in terms of amplitude:

$$p_E(E) = \frac{E}{\sigma^2} \exp\left(-\frac{E^2 + C^2}{2\sigma^2}\right) I_0\left(\frac{EC}{\sigma^2}\right),$$

where C is the amplitude of the deterministic vector;

$\sigma\sqrt{2}$ is the mean-square amplitude of the random vector and E is positive.

Let us express this distribution in terms of power $P = E^2$.

We return for this purpose to the definition of $p_E(E)$:

$$P_E(E) - P_r(E < e < E + dE) = \frac{d f_E(E)}{d E}$$

where East-West is the random variable associated with E and $f_E(E)$ is the cumulative function:

$$f_E(E) = P_r(e < E)$$

The cumulative function of P is written as follows:

$$f_p(P) = P_r(p < P) = P_r(e^2 < P)$$
$$= P_r(e < \sqrt{P}) = f_E(\sqrt{P})$$

and the probability distribution:

$$p_p(P) = \frac{d f_p(p)}{d P} = \frac{d f_E(\sqrt{p})}{d P} = \frac{d f_E(\sqrt{p})}{d E} \frac{dE}{dP}$$
$$= p_E(\sqrt{P}) \frac{d\sqrt{P}}{d P} = \frac{p_E(\sqrt{P})}{2\sqrt{P}}$$

The Rice distribution is therefore written as follows in terms of power:

$$p_p(P) = \frac{p_E(\sqrt{p})}{2\sqrt{P}} = \frac{1}{P_a} \exp\left(-\frac{P + P_c}{P_a}\right) I_0\left(\frac{2\sqrt{P P_c}}{P_a}\right)$$

where $P_a = 2\sigma^2$ is the mean power of the random vector;

P_c = is the power of the deterministic vector.

SUPPLEMENT No. 1 TO THE STUDY OF SHORT-TERM FLUCTUATIONS
(Chapter III, paragraph 2)

For the verification of the RICE distribution, use is made of experimentally obtained received signal levels and of theoretical calculations. The theoretical calculation determines the normalised n order moment of the received signal levels $E(T^n)/E(T)^n$ as a function of the ratio of deterministic power and random power (Pd/Pa) (Figure 1).

The matching of the measurement points to the theoretical curve proves that the signal level fluctuations follow closely a RICE distribution.

$E(T^n)/E(T)^n$

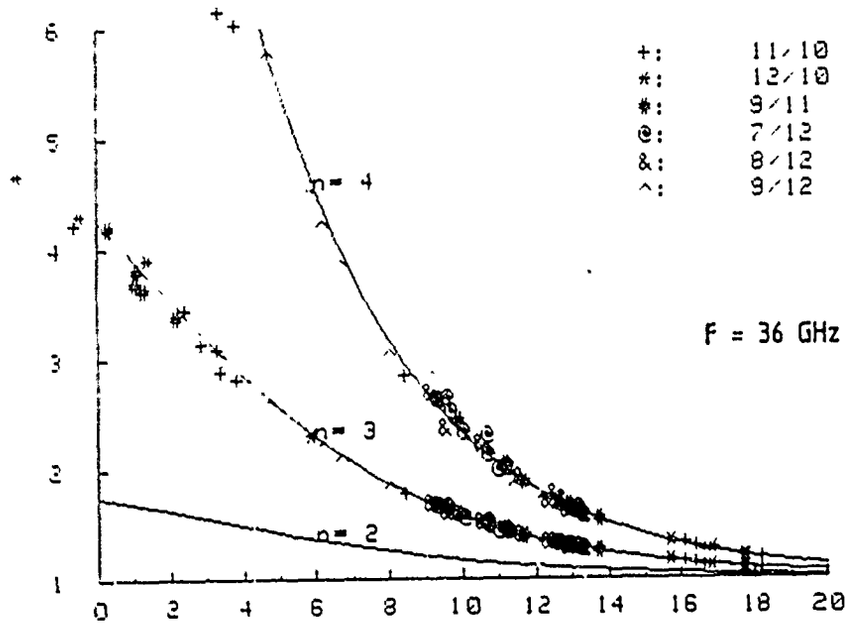

Figure 1